Computer Methods in Applied Mechanics and Engineering 463 (2027) 119401

Contents lists available at ScienceDirect

Comput. Methods Appl. Mech. Engrg.

journal homepage: www.elsevier.com/locate/cma

A porosity-consistent 3D multiphysics smoothed particle hydrodynamics framework for modeling soil–water–rock–structure interactions

Shuaihao Zhang [a,*], Jidong Zhao [a,*], Ruofeng Feng [a], Honghu Zhu [b]

[a] Department of Civil and Environmental Engineering, Hong Kong University of Science and Technology, Clearwater Bay, Kowloon, Hong Kong Special Administrative Region of China

[b] School of Earth Sciences and Engineering, Nanjing University, Nanjing, China

ARTICLE INFO

Keywords:
Smoothed particle hydrodynamics
Porosity-consistent particle relaxation
Fluid-volume conservation
Soil–water interaction
Multiphysics coupling

ABSTRACT

Dynamic interactions among water, deformable soil, discrete rock inclusions, and engineering structures involve large deformation, free surfaces, and multiple moving interfaces. This study presents a three-dimensional smoothed particle hydrodynamics (SPH) framework for these coupled processes. Soil and water are represented by two overlapping particle sets within two-phase mixture theory. An intrinsic-density formulation is adopted for the water phase, allowing the representative mixture volume of each water particle to vary consistently with the local porosity as it moves between clear-fluid and porous regions. To construct initially saturated configurations, a level-set-guided porosity-consistent particle-relaxation method is developed. It produces an equal-mass water-particle distribution whose local number density, spacing, and representative volume conform to the prescribed porosity field. A porosity-consistent extension of the unified transport-velocity formulation is further proposed to regularize the water-particle distribution during physical time integration while preserving porosity-induced spacing variations. The soil and water phases are treated in an updated Lagrangian description, whereas rocks and structures are represented as total-Lagrangian Neo-Hookean solids. Previously established Riemann-based stabilization, spatial multi-resolution, dual-criteria time stepping, and phase-decoupled subcycling are incorporated to support robust and tractable three-dimensional calculations. The formulation is assessed using a fluid-volume-conservation test, U-tube seepage, and a suite of two- and three-phase benchmarks, and is illustrated through two engineering-scale applications. The results show that the framework preserves the expected fluid volume, reproduces porosity-dependent seepage behavior, and remains stable in strongly coupled large-deformation simulations.

1. Introduction

The dynamic interactions among multiphase geomaterials (water and soil), discrete macroscopic inclusions (boulders and cobbles), and engineering structures are ubiquitous in nature and widely encountered across diverse engineering disciplines. Typical examples include catastrophic bouldery debris flows impacting protective barriers in mountainous regions [1,2] (as shown in Fig. 1a), and severe wave hydrodynamics interacting with seabed soil, gravels, and vegetation (*e.g.*, mangrove forests) in coastal zones [3,4]. These phenomena are characterized by massive deformations, rapid free-surface evolutions, intense phase transitions,

* Corresponding authors.
E-mail addresses: shzhangce@ust.hk (S. Zhang), jzhao@ust.hk (J. Zhao).

https://doi.org/10.1016/j.cma.2026.119401
Received 2 May 2026; Received in revised form 26 August 2026; Accepted 3 September 2026

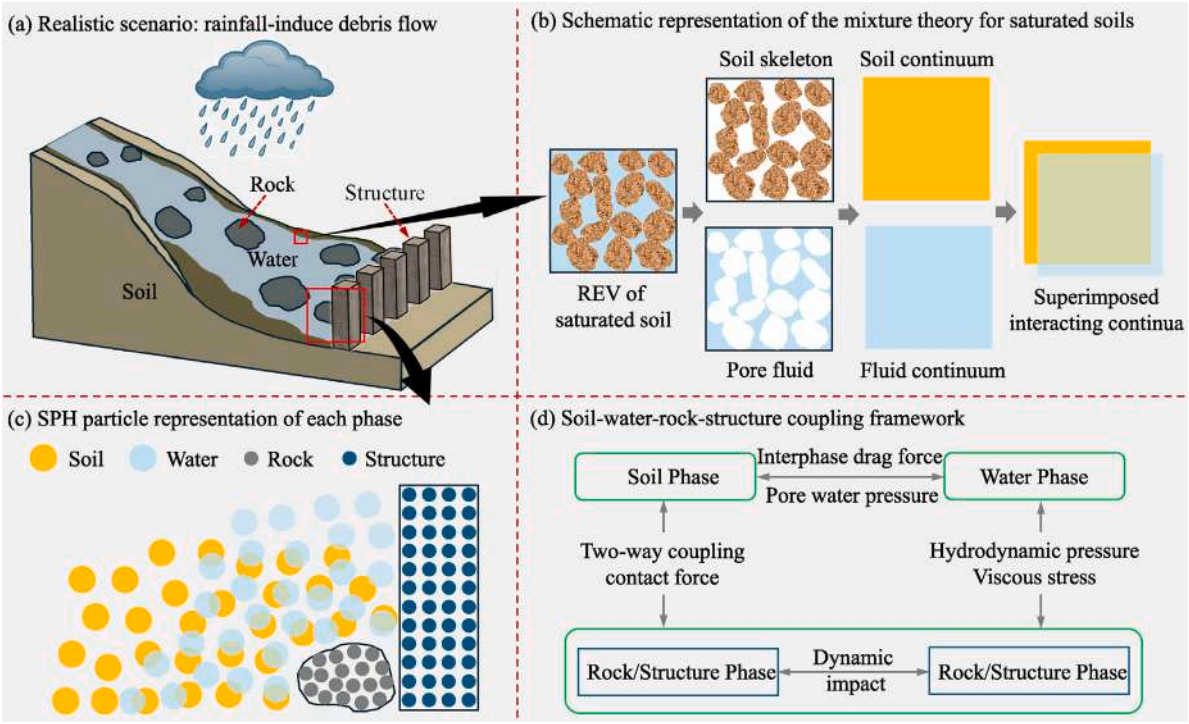

Fig. 1. Schematic of the integrated soil–water–rock–structure interaction framework within the multiphase SPH formulation, from physical interpretation to interphase coupling mechanisms.

and strong dynamic momentum exchanges among distinct physical phases. Developing a robust computational framework to accurately and efficiently model such soil–water–rock–structure interactions is crucial for the design of mitigation measures and the assessment of infrastructural resilience.

Traditionally, grid-based numerical methods, such as the finite element method (FEM) [5,6], the finite volume method (FVM) [7], and coupled Eulerian-Lagrangian (CEL) approaches [8,9], have been extensively employed to simulate multiphase flows and fluid–structure interactions. While advanced techniques such as CEL and arbitrary Lagrangian–Eulerian (ALE) formulations have largely alleviated the issue of mesh entanglement in large deformation problems, they still encounter fundamental bottlenecks when extended to highly complex multiphysics systems, such as soil–water–rock–structure interactions. Specifically, representing elastoplastic geomaterials within an Eulerian framework inevitably introduces severe numerical diffusion when advecting history-dependent tensorial state variables (*e.g.*, plastic strain and stress tensors) across fixed grids [10,11]. Furthermore, explicitly tracking the continuously evolving boundaries among Newtonian fluids, porous geomaterials, discrete moving boulders, and structural components using grid-based interface-tracking algorithms (*e.g.*, volume-of-fluid or level-set methods) incurs prohibitive algorithmic complexity and computational overhead.

To circumvent the limitations imposed by mesh topology, the smoothed particle hydrodynamics (SPH) method [12,13], a fully Lagrangian meshfree method, has emerged as a robust alternative. By discretizing the continuum into a set of interacting Lagrangian particles, SPH naturally accommodates massive deformations and effectively captures complex free-surface fragmentation. As a Lagrangian method, SPH particles serve as material points that intrinsically carry history-dependent state variables, thereby eliminating the numerical diffusion associated with Eulerian advection. Moreover, the interfaces between distinct phases are implicitly defined by the evolving particle distributions, enabling the framework to handle strong multiphase couplings without the need for cumbersome interface-tracking or capturing algorithms [14–16]. Over the past decades, SPH has been extensively extended to geomechanics and multiphase flows [17–21], yielding promising results in simulating landslides, seepage flows, and debris flows [18,22,23].

Nevertheless, while significant progress has been made in simulating two-phase interactions, such as soil–water coupling or fluid–structure interaction, research addressing more intricate multiphysics systems involving the simultaneous presence of soil, water, discrete rock inclusions, and engineering structures remains remarkably scarce. In natural environments, these four phases frequently coexist and interact synergistically, requiring a unified framework capable of resolving multiple heterogeneous interfaces and disparate constitutive behaviors concurrently. The principal challenge is therefore to maintain consistent phase representations, constitutive descriptions, and momentum exchange across multiple evolving interfaces while retaining a computational cost compatible with three-dimensional (3D) applications.

Before addressing the complexities of multiphase coupling, it is essential to establish the rigorous numerical treatments for the individual soil and water phases. Within the SPH framework, the soil phase is conventionally discretized using an updated Lagrangian (UL) formulation [17], in which the geomaterial is modeled as an elastoplastic continuum to accurately capture its highly non-linear, path-dependent mechanical behavior. Concurrently, the water phase is governed by the Navier–Stokes equations and simulated using the weakly compressible SPH (WCSPH) approach, which treats the liquid as a Newtonian fluid. Standard SPH formulations for both elastoplastic solids and weakly compressible fluids rely on artificial viscosity to maintain numerical stability [17,24]. However, this treatment often introduces excessive numerical dissipation, which can adversely affect physical flow characteristics [25,26]. To address this fundamental limitation, the present work employs a unified low-dissipation Riemann solver for both the soil [27] and water [25] phases. By reconstructing the interacting states and solving a Riemann problem along the inter-particle direction, this Riemann-based SPH framework effectively suppresses numerical oscillations while reducing numerical dissipation compared to viscosity-based stabilization [25,28]. Beyond Riemann-based stabilization, recent developments in meshfree particle methods have also improved numerical consistency, accuracy, and robustness through second-order SPH derivative operators [29], stabilized least-squares moving-particle formulations [30], and moving-least-squares-based generalized SPH schemes with discretization-error estimation [31].

In the context of soil–water coupling within SPH, existing approaches can be broadly classified as single-layer and double-layer (or multi-layer) formulations. A single-layer formulation represents the soil–water mixture using one particle set and evaluates equivalent mixture properties [22,32,33]. It is computationally economical for mixture-dominated seepage and granular-flow problems, but it does not independently resolve the relative motion of the two constituents or the free-surface dynamics of water outside the porous skeleton.

Morikawa and Asai [34] proposed a phase-change strategy for landslide simulation, in which soil particles are modeled by finite-strain elastoplastic TLSPH before failure and are converted to a non-Newtonian IISPH fluid phase once a prescribed plastic-strain threshold is exceeded. The solid and fluidized particles are coupled through a fluid–structure interaction treatment. A double-layer formulation instead uses two spatially overlapping particle sets to represent the soil skeleton and water independently (Fig. 1b). Based on two-phase mixture theory and phase-wise mass and momentum balances [18,35,36], this formulation can describe buoyancy, drag, relative phase motion, and the transition between clear-fluid and porous regions within one computational framework.

A central consistency requirement in a double-layer formulation is that the representative mixture volume associated with a water particle must conform to the local water-accessible volume fraction. Early coupled SPH formulations, including those of Bui et al. [18], captured drag-driven soil–water interaction but did not explicitly enforce a porosity-dependent representative water-particle volume. More recent formulations for fixed or prescribed porous media (the deformation of porous media is not considered) have introduced porosity-dependent apparent density, particle volume, and particle regularization [37–39]. Zhu et al. [36] further formulated the water equations for deformable porous media in terms of the intrinsic water density and allowed the representative mixture volume associated with each water particle to vary consistently with the local porosity, thereby accounting for spatial and temporal changes in porosity during the coupled motion.

A distinct issue arises when soil and water overlap at the initial time, as in saturated seabeds, submerged granular deposits, and initially saturated seepage domains. In the initialization used by Zhu et al. [36], water particles were assigned the same initial geometric volume in clear-fluid and porous regions, whereas their masses were scaled by the local water volume fraction. This construction is consistent in terms of mass and apparent density, but it does not generate an equal-mass water discretization whose initial particle number density and spacing conform to the prescribed porosity. Consequently, a separate initialization procedure is required when a uniform particle mass is to be retained throughout the water phase.

Building on the intrinsic-density and variable-representative-volume formulation, the present work develops two porosity-consistent particle treatments. First, based on the level-set-guided particle-relaxation framework [40,41], a porosity-consistent relaxation procedure is introduced to construct initially overlapping soil–water configurations using equal-mass water particles. The local water-particle number density, spacing, and representative volume are prescribed according to the initial porosity field, so that the pore-water discretization is porosity-consistent from the beginning of the physical simulation. Second, the unified transport-velocity formulation of Zhang et al. [26] is extended to regularize the water-particle distribution during time integration without erasing the spacing variation induced by the evolving porosity. In contrast to particle regularization in a fixed or prescribed porous domain, the target representative volume and the projection direction are evaluated from the water volume fraction reconstructed from the deforming soil skeleton.

Beyond the soil–water formulation, rocks and engineering structures are represented as total-Lagrangian (TL) Neo-Hookean solids and coupled to the updated-Lagrangian soil and water phases through established fluid–structure and contact treatments [42,43]. The low-dissipation Riemann solvers [27], hybrid UL/TL treatment [42], spatial multi-resolution [42], dual-criteria time stepping [44], and phase-decoupled subcycling [42] are previously established numerical ingredients that are incorporated here to support robust and tractable 3D calculations. Within this computational environment, the water phase, deformable soil skeleton, rock inclusions, and engineering structures are integrated into a single 3D SPH framework. This integration extends the application scope of the framework to soil–water–rock–structure processes involving free surfaces, evolving porosity, large deformation, and multiple moving interfaces.

Mature open-source SPH platforms, such as DualSPHysics and its geotechnical extensions, already provide advanced capabilities for free-surface flow, multiphase flow, SPH–DEM coupling, liquid–granular interaction, and rigid-body dynamics [20,45,46]. The objective of the present study is not to reproduce these general capabilities. Instead, it addresses the discrete consistency of an equal-mass water-particle representation within a deformable two-continuum soil–water formulation, in which porosity evolves with the

soil skeleton and water particles move between clear-fluid and locally saturated porous regions. This formulation is subsequently incorporated into an environment containing deformable rock and structural phases. The proposed numerical framework is developed and implemented based on the open-source SPHinXsys library [47]. The remainder of this paper is organized as follows. Section 2 presents the governing equations and constitutive descriptions of the soil, water, rock, and structure phases. Section 3 gives the SPH discretization and the interphase coupling treatments, including the equal-mass porosity-consistent particle relaxation and the porosity-consistent transport-velocity regularization. Section 4 assesses the two-phase interaction mechanisms, including fluid-volume conservation and seepage through porous media. Section 5 examines three-phase soil–water–solid interactions. Section 6 illustrates the framework through two three-dimensional engineering applications. Conclusions and limitations are summarized in Section 7.

2. Governing equations and constitutive relations

In this study, the multiphase system is modeled by solving the conservation laws of mass and momentum for each phase. To accommodate the distinct mechanical behaviors of different materials, we employ a unified Lagrangian approach with tailored formulations. For the porous soil–water domain, we adopt the mixture theory [48–50], treating the soil skeleton and pore water as two overlapping continua. Specifically, an updated Lagrangian (UL) formulation is employed for the water and soil phases to naturally capture their continuous flow and severe topological evolution. Conversely, for solid phases characterized by large-deformation dynamics but fixed material topology (rocks and structures), a total Lagrangian (TL) formulation is utilized.

2.1. Mixture theory for soil–water phases

The mathematical modeling of the saturated soil domain is grounded in the mixture theory [48–50]. The present formulation is restricted to clear-water regions and locally saturated soil–water mixture regions. In this rigorous framework, the fluid-saturated porous medium is conceptualized as the superposition of two interpenetrating continua: the solid skeleton and the pore fluid. At any material point within the saturated mixture region, the two phases are distinct yet coupled and are governed by their respective conservation laws.

The kinematic state of the system is described by the phase volume fractions n^s and n^w, and the phase velocities $\mathbf{v}^s$ and $\mathbf{v}^w$. Within a locally saturated soil–water mixture region, the water volume fraction is equal to the porosity φ, i.e., $n^w = \varphi$, and the saturation constraint is written as $n^s + \varphi = 1$. In a clear-water region, $n^s = 0$ and $n^w = 1$. To formulate the conservation equations, we introduce the partial density (or apparent density) of each phase, defined as the product of its intrinsic density and its volume fraction:

$$\tilde{\rho}^s = n^s \rho^s = (1 - \varphi)\rho^s, \tag{1}$$

$$\tilde{\rho}^w = n^w \rho^w = \varphi \rho^w, \tag{2}$$

where ρ^s is the intrinsic density of soil grains, and ρ^w is the intrinsic density of water. In this study, the soil grains are assumed to be intrinsically incompressible ($\rho^s = \text{const}$), while the soil skeleton is deformable (φ varies) and the pore water is weakly compressible to accommodate the SPH formulation.

Crucially, the mechanical coupling between the two phases is governed by the effective stress principle. The partial Cauchy stress tensor of the soil phase $\tilde{\boldsymbol{\sigma}}^s$ is decomposed into the effective stress $\boldsymbol{\sigma}^{s\prime}$ and the pore water pressure contribution:

$$\tilde{\boldsymbol{\sigma}}^s = \boldsymbol{\sigma}^{s\prime} - n^s p^w \mathbf{I}, \tag{3}$$

where p^w denotes the pore-water pressure (positive in compression). It should be noted that the continuum mechanics convention, *i.e.*, tension taken as positive, is adopted for all stress tensors in this study. The partial stress tensor of the water phase is given by:

$$\tilde{\boldsymbol{\sigma}}^w = -n^w p^w \mathbf{I} + n^w \boldsymbol{\tau}^w, \tag{4}$$

where $\boldsymbol{\tau}^w$ is the viscous stress tensor of the fluid.

2.2. Soil phase: Porous media formulation

The soil phase is treated as a deformable porous continuum. Based on the conservation of mass, the continuity equation for the soil phase is initially expressed in terms of the partial density $\tilde{\rho}^s$ [18]:

$$\frac{\mathrm{d}\tilde{\rho}^s}{\mathrm{d}t} + \tilde{\rho}^s(\nabla \cdot \mathbf{v}^s) = 0, \tag{5}$$

where $\mathbf{v}^s$ denotes the velocity of the soil skeleton. By combining Eq. (1) and the above equation, we obtain:

$$\frac{\mathrm{d}(n^s \rho^s)}{\mathrm{d}t} + n^s \rho^s(\nabla \cdot \mathbf{v}^s) = 0. \tag{6}$$

Eq. (6) can be rewritten as:

$$\rho^s \frac{\mathrm{d}n^s}{\mathrm{d}t} + n^s \frac{\mathrm{d}\rho^s}{\mathrm{d}t} = -n^s \rho^s(\nabla \cdot \mathbf{v}^s). \tag{7}$$

Under the assumption that the soil grains are intrinsically incompressible ($\mathrm{d}\rho^s/\mathrm{d}t = 0$), the conservation of mass is reformulated to describe the evolution of the soil volume fraction n^s:

$$\frac{\mathrm{d}n^s}{\mathrm{d}t} = -n^s \nabla \cdot \mathbf{v}^s. \tag{8}$$

The conservation of linear momentum for the soil phase is given by:

$$\tilde{\rho}^s \frac{\mathrm{d}\mathbf{v}^s}{\mathrm{d}t} = \nabla \cdot \tilde{\boldsymbol{\sigma}}^s + \tilde{\rho}^s \boldsymbol{g} + \boldsymbol{f}^{s\leftarrow w} + \boldsymbol{f}^{s\leftarrow rs}, \tag{9}$$

where $\boldsymbol{g}$ is the gravitational acceleration vector with a magnitude of $g = 9.81\ \mathrm{m/s^2}$. Here, $\boldsymbol{f}^{s\leftarrow w}$ denotes the hydrodynamic interaction force density (force per unit volume) exerted by the water phase on the soil skeleton, while $\boldsymbol{f}^{s\leftarrow rs}$ represents the mechanical contact force density exerted by the rock and structure phases. The interface force $\boldsymbol{f}^{s\leftarrow w}$ can be expressed as:

$$\boldsymbol{f}^{s\leftarrow w} = -p^w \nabla n^w + \boldsymbol{f}^d, \tag{10}$$

where the first term represents the buoyancy-like force, and $\boldsymbol{f}^d$ is the drag force. Substituting Eqs. (3) and (10) into Eq. (9), the momentum equation for the soil phase can be rewritten as:

$$\begin{aligned} \tilde{\rho}^s \frac{\mathrm{d}\mathbf{v}^s}{\mathrm{d}t} &= \nabla \cdot \boldsymbol{\sigma}^{s\prime} - (p^w \nabla n^s + n^s \nabla p^w) + \tilde{\rho}^s \boldsymbol{g} - p^w \nabla n^w + \boldsymbol{f}^d + \boldsymbol{f}^{s\leftarrow rs} \\ &= \nabla \cdot \boldsymbol{\sigma}^{s\prime} - n^s \nabla p^w + \tilde{\rho}^s \boldsymbol{g} + \boldsymbol{f}^d + \boldsymbol{f}^{s\leftarrow rs}, \end{aligned} \tag{11}$$

where we have used the relation $\nabla n^s = -\nabla n^w$.

To close the governing system, a constitutive closure is required to relate the effective stress $\boldsymbol{\sigma}^{s\prime}$ to the deformation history of the soil skeleton. In this work, the soil phase is modeled as an elastic–perfectly plastic material governed by the Drucker–Prager (D–P) yield criterion with a non-associated flow rule [51,52]. For a detailed discussion on this constitutive model and its specific SPH implementation, readers are referred to Refs. [17,27]. Therefore, only a brief overview is presented herein.

The yield function f and the plastic potential function g are formulated in terms of stress invariants as:

$$f(I_1, J_2) = \alpha_\phi I_1 + \sqrt{J_2} - k_c, \tag{12}$$

$$g(I_1, J_2) = \alpha_\psi I_1 + \sqrt{J_2}, \tag{13}$$

where $I_1 = \mathrm{tr}(\boldsymbol{\sigma}^{s\prime})$ is the first invariant of the effective stress tensor, and $J_2 = \frac{1}{2}\boldsymbol{s}^{s\prime} : \boldsymbol{s}^{s\prime}$ is the second invariant of the deviatoric effective stress tensor. Here, the deviatoric effective stress is defined as $\boldsymbol{s}^{s\prime} = \boldsymbol{\sigma}^{s\prime} - \frac{1}{3} I_1 \mathbf{I}$. The material constants α_ϕ, k_c, and α_ψ are determined by the cohesion c, the internal friction angle ϕ, and the dilation angle ψ of the soil:

$$\alpha_\phi = \frac{\tan\phi}{\sqrt{9 + 12\tan^2\phi}}, \quad k_c = \frac{3c}{\sqrt{9 + 12\tan^2\phi}}, \quad \alpha_\psi = \frac{\tan\psi}{\sqrt{9 + 12\tan^2\psi}}. \tag{14}$$

To ensure objectivity under large rigid-body rotations, the stress evolution is computed using the Jaumann stress rate. After converting the Jaumann objective rate into the material time derivative, the constitutive relation is expressed as:

$$\dot{\boldsymbol{\sigma}}^{s\prime} = 2G\left[\dot{\boldsymbol{\varepsilon}}^s - \frac{1}{3}\mathrm{tr}(\dot{\boldsymbol{\varepsilon}}^s)\mathbf{I}\right] + K\mathrm{tr}(\dot{\boldsymbol{\varepsilon}}^s)\mathbf{I} - \dot{\lambda}\left(3\,K\alpha_\psi \mathbf{I} + \frac{G}{\sqrt{J_2}}\boldsymbol{s}^{s\prime}\right) + \boldsymbol{\omega}^s \cdot \boldsymbol{\sigma}^{s\prime} - \boldsymbol{\sigma}^{s\prime} \cdot \boldsymbol{\omega}^s, \tag{15}$$

where G and K denote the shear and bulk moduli, respectively. The strain rate tensor $\dot{\boldsymbol{\varepsilon}}^s$ and the spin tensor $\boldsymbol{\omega}^s$ represent the symmetric and skew-symmetric parts of the velocity gradient, and are defined as:

$$\begin{cases} \dot{\boldsymbol{\varepsilon}}^s = \frac{1}{2}\left[\nabla\mathbf{v}^s + (\nabla\mathbf{v}^s)^T\right], \\ \boldsymbol{\omega}^s = \frac{1}{2}\left[\nabla\mathbf{v}^s - (\nabla\mathbf{v}^s)^T\right]. \end{cases} \tag{16}$$

The plastic multiplier rate $\dot{\lambda}$ is determined by the consistency condition ($\dot{f} = 0$ during plastic loading):

$$\dot{\lambda} = \frac{3\alpha_\phi K\mathrm{tr}(\dot{\boldsymbol{\varepsilon}}^s) + (G/\sqrt{J_2})\boldsymbol{s}^{s\prime} : \dot{\boldsymbol{\varepsilon}}^s}{9\alpha_\phi K\alpha_\psi + G}. \tag{17}$$

Eq. (17) is applied only during plastic loading. For elastic loading or unloading, $\dot{\lambda} = 0$.

The constitutive equation is integrated using an explicit rate-based stress update. At each time step, the loading state and the corresponding plastic multiplier rate are first determined, after which the complete material stress rate in Eq. (15), including the elastic, plastic, and rotational contributions, is evaluated. The provisional effective stress at time step $n+1$ is then obtained as:

$$\boldsymbol{\sigma}_{n+1}^{s\prime,\mathrm{pred}} = \boldsymbol{\sigma}_n^{s\prime} + \dot{\boldsymbol{\sigma}}_n^{s\prime}\Delta t. \tag{18}$$

It should be emphasized that Eq. (18) represents a complete rate-based elastoplastic update rather than an elastic trial step, because the plastic contribution associated with $\dot{\lambda}$ has already been included in $\dot{\boldsymbol{\sigma}}_n^{s\prime}$.

Owing to the explicit time integration and the finite time-step size, the provisionally updated stress may exhibit numerical drift outside the admissible stress domain. Following Bui et al. [17], a post-integration stress-correction procedure is therefore applied to restore numerical consistency.

First, if $-\alpha_\phi I_{1,n+1}^{\text{pred}} + k_c < 0$, the tension-cracking correction of Bui et al. [17] is applied. The hydrostatic stress component is shifted to the pressure corresponding to the apex of the Drucker–Prager yield surface, while the deviatoric stress components remain unchanged:

$$\boldsymbol{\sigma}_{n+1}^{s\prime} = \boldsymbol{\sigma}_{n+1}^{s\prime,\text{pred}} - \frac{1}{3}\left(I_{1,n+1}^{\text{pred}} - \frac{k_c}{\alpha_\phi}\right)\mathbf{I}. \tag{19}$$

Otherwise, if $-\alpha_\phi I_{1,n+1}^{\text{pred}} + k_c < \sqrt{J_{2,n+1}^{\text{pred}}}$, the provisional stress lies outside the conical part of the Drucker–Prager yield surface. The deviatoric component is then scaled back to the yield surface while the hydrostatic component is retained:

$$\boldsymbol{\sigma}_{n+1}^{s\prime} = \frac{-\alpha_\phi I_{1,n+1}^{\text{pred}} + k_c}{\sqrt{J_{2,n+1}^{\text{pred}}}}\boldsymbol{s}_{n+1}^{s\prime,\text{pred}} + \frac{1}{3}I_{1,n+1}^{\text{pred}}\mathbf{I}. \tag{20}$$

If neither condition is satisfied, the provisional stress lies inside the admissible stress domain and is retained without correction:

$$\boldsymbol{\sigma}_{n+1}^{s\prime} = \boldsymbol{\sigma}_{n+1}^{s\prime,\text{pred}}. \tag{21}$$

The rate-based constitutive update and the subsequent stress-correction procedure are summarized in Algorithm 1.

Algorithm 1: Effective-stress update algorithm for the non-associated Drucker–Prager constitutive model.

Input : $\boldsymbol{\sigma}_n^{s\prime}$, $\dot{\boldsymbol{\epsilon}}_n^s$, $\boldsymbol{\omega}_n^s$, and Δt
Output: Updated effective stress $\boldsymbol{\sigma}_{n+1}^{s\prime}$

Compute $I_{1,n}$, $\boldsymbol{s}_n^{s\prime}$, $J_{2,n}$, and f_n from Eqs. (12) and (13);
Determine the current loading state from the yield condition and loading direction;
if *plastic loading* **then**
  Compute $\dot{\lambda}_n$ from Eq. (17);
else
  Set $\dot{\lambda}_n = 0$;
end
Compute the complete material effective-stress rate $\dot{\boldsymbol{\sigma}}_n^{s\prime}$ from Eq. (15);
Update the provisional effective stress: $\boldsymbol{\sigma}_{n+1}^{s\prime,\text{pred}} = \boldsymbol{\sigma}_n^{s\prime} + \dot{\boldsymbol{\sigma}}_n^{s\prime}\Delta t$;
Compute $I_{1,n+1}^{\text{pred}}$, $\boldsymbol{s}_{n+1}^{s\prime,\text{pred}}$, and $J_{2,n+1}^{\text{pred}}$ from $\boldsymbol{\sigma}_{n+1}^{s\prime,\text{pred}}$;
if $-\alpha_\phi I_{1,n+1}^{\text{pred}} + k_c < 0$ **then**
  Apply the tension-cracking correction: $\boldsymbol{\sigma}_{n+1}^{s\prime} = \boldsymbol{\sigma}_{n+1}^{s\prime,\text{pred}} - \frac{1}{3}\left(I_{1,n+1}^{\text{pred}} - \frac{k_c}{\alpha_\phi}\right)\mathbf{I}$;
else
  if $-\alpha_\phi I_{1,n+1}^{\text{pred}} + k_c < \sqrt{J_{2,n+1}^{\text{pred}}}$ **then**
    Scale the deviatoric stress back to the yield surface: $\boldsymbol{\sigma}_{n+1}^{s\prime} = \frac{-\alpha_\phi I_{1,n+1}^{\text{pred}} + k_c}{\sqrt{J_{2,n+1}^{\text{pred}}}}\boldsymbol{s}_{n+1}^{s\prime,\text{pred}} + \frac{1}{3}I_{1,n+1}^{\text{pred}}\mathbf{I}$;
  else
    Retain the provisional stress: $\boldsymbol{\sigma}_{n+1}^{s\prime} = \boldsymbol{\sigma}_{n+1}^{s\prime,\text{pred}}$;
  end
end

The present soil formulation differs from the TLSPH-based finite-strain elastoplastic formulation of Morikawa and Asai [34]. Their formulation evaluates deformation and stress in the fixed reference configuration and employs a Hencky hyperelastic–plastic model, whereas the present method adopts an updated-Lagrangian rate-type elastoplastic formulation in the current configuration, allowing the particle configuration and interaction topology to evolve continuously during large deformation. The Jaumann stress rate provides frame objectivity at the constitutive-rate level. However, because the adopted elastoplastic formulation is not derived from a finite-strain elastic energy potential, exact energy consistency under arbitrary finite-deformation loading paths is not guaranteed.

2.3. Water phase: From pure fluid to pore water

In the proposed unified framework, the governing equations for the water phase are formulated to describe both the clear-fluid region and the pore water inside the soil skeleton. The Eulerian mass conservation of the water phase is written as

$$\frac{\partial(n^w\rho^w)}{\partial t} + \nabla\cdot(n^w\rho^w\mathbf{v}^w) = 0, \tag{22}$$

where $\mathbf{v}^w$ is the pore-average water velocity. Combining Eq. (22) with the saturation condition $n^w + n^s = 1$ and the mass balance of the soil skeleton gives the intrinsic-density form

$$\frac{\mathrm{d}\rho^w}{\mathrm{d}t} = -\frac{\rho^w}{n^w}\nabla\cdot\left(n^w\mathbf{v}^w + n^s\mathbf{v}^s\right), \tag{23}$$

where $\mathrm{d}(\cdot)/\mathrm{d}t = \partial(\cdot)/\partial t + \mathbf{v}^w \cdot \nabla(\cdot)$ denotes the material derivative following the pore-average water velocity. In the clear-fluid limit, $n^w = 1$ and $n^s = 0$, Eq. (23) reduces to the standard weakly compressible SPH continuity equation. The momentum conservation is written as:

$$\tilde{\rho}^w \frac{\mathrm{d}\mathbf{v}^w}{\mathrm{d}t} = \nabla \cdot \tilde{\boldsymbol{\sigma}}^w + \tilde{\rho}^w \boldsymbol{g} + \boldsymbol{f}^{w \leftarrow s} + \boldsymbol{f}^{w \leftarrow rs}, \tag{24}$$

where $\boldsymbol{f}^{w \leftarrow s} = -\boldsymbol{f}^{s \leftarrow w}$. Substituting Eqs. (4) and (10) into Eq. (24), the momentum equation for the water phase can be rewritten as:

$$\begin{aligned} \tilde{\rho}^w \frac{\mathrm{d}\mathbf{v}^w}{\mathrm{d}t} &= -(p^w \nabla n^w + n^w \nabla p^w) + \nabla \cdot (n^w \boldsymbol{\tau}^w) + \tilde{\rho}^w \boldsymbol{g} + p^w \nabla n^w - \boldsymbol{f}^d + \boldsymbol{f}^{w \leftarrow rs} \\ &= -n^w \nabla p^w + \nabla \cdot (n^w \boldsymbol{\tau}^w) + \tilde{\rho}^w \boldsymbol{g} - \boldsymbol{f}^d + \boldsymbol{f}^{w \leftarrow rs}. \end{aligned} \tag{25}$$

The pore pressure p^w is related to the intrinsic water density ρ^w via an artificial isothermal equation of state [53,54]:

$$p^w = (c_0^w)^2 (\rho^w - \rho_0^w), \tag{26}$$

where c_0^w is the artificial speed of sound in the water, and ρ_0^w is the initial density of water. c_0^w is set to $c_0^w = 10 \left|\mathbf{v}_{max}\right|$ here, in which $\mathbf{v}_{max}$ represents the anticipated maximum flow velocity, to ensure that the density fluctuations remain below 1% during the simulation [54].

This equation of state is used to impose weak compressibility and close the WCSPH equations; it is not intended as a constitutive model for physically rigorous pore-water pressure, matric suction, or soil–water retention behavior. More rigorous pore-pressure formulations can be found in Biot-type poromechanics and computational geomechanics frameworks [5,55]. At the particle level, the apparent density also defines the representative SPH volume of a water particle,

$$V_i^w = \frac{m_i^w}{\tilde{\rho}_i^w} = \frac{m_i^w}{n_i^w \rho_i^w}. \tag{27}$$

This relation allows the particle volume to change consistently with the local water-accessible volume fraction while the pressure remains linked to the intrinsic water density. The shear stress tensor $\boldsymbol{\tau}^w$ is given by:

$$\boldsymbol{\tau}^w = 2\eta \dot{\boldsymbol{\varepsilon}}^w = \eta \left[\nabla \mathbf{v}^w + (\nabla \mathbf{v}^w)^T\right], \tag{28}$$

where η is the dynamic viscosity of water.

2.4. Viscous drag force between soil and water

Due to viscous dissipation within the pore space, the relative motion between pore water and the deformable soil skeleton gives rise to an interphase drag force. From the perspective of mixture theory, this interaction is modeled as a body force acting on each phase with equal magnitude and opposite direction, thereby ensuring momentum conservation of the mixture system.

For laminar seepage flows in porous media, the drag force is commonly described by Darcy's law, which assumes a linear relationship between the drag force and the relative velocity of the two phases. Accordingly, the drag force exerted by the water phase on the soil skeleton can be expressed as:

$$\boldsymbol{f}^d = \frac{(n^w)^2 \rho^w g}{K^s} \left(\mathbf{v}^w - \mathbf{v}^s\right), \tag{29}$$

where K^s (with units of m/s) is the hydraulic conductivity of the porous medium. The hydraulic conductivity is related to the intrinsic permeability k (unit: m^2) through

$$K^s = \frac{\rho^w g k}{\eta}. \tag{30}$$

Although the linear Darcy-type drag formulation has been widely adopted in modeling water–soil interaction under low Reynolds number conditions [35,56,57], it becomes inadequate when inertial effects are non-negligible. In many dynamic water–soil coupling problems, such as wave-induced seepage and rapid transient flows, the Reynolds number within the pore space can be sufficiently large that nonlinear drag behavior must be taken into account. In such cases, empirical or semi-empirical nonlinear drag laws have been proposed to better capture the flow resistance in porous media. In the present study, a quadratic drag formulation based on the Ergun-type relation is employed. The drag force per unit mixture volume is written as [58]:

$$\boldsymbol{f}^d = \alpha_d \frac{\eta (1 - n^w)^2}{n^w D_c^2} \left(\mathbf{v}^w - \mathbf{v}^s\right) + \beta_d \frac{\rho^w (1 - n^w)}{D_c} \left|\mathbf{v}^w - \mathbf{v}^s\right| \left(\mathbf{v}^w - \mathbf{v}^s\right), \tag{31}$$

where D_c denotes the characteristic length of the soil grains. For coarse-grained soils, D_c is commonly taken as D_{50}, *i.e.*, the median grain diameter corresponding to 50% passing in the grain size distribution. The coefficients α_d and β_d are empirical parameters that account for the viscous and inertial contributions to the drag force, respectively. According to Ref. [36], the values $\alpha_d = 150$ and $\beta_d = 1.75$ are adopted in this work.

It is worth noting that the drag force defined in Eq. (31) naturally vanishes in regions where the porosity approaches unity, corresponding to pure water without soil grains. This feature allows the same governing equations to be applied seamlessly throughout the entire water domain, eliminating the need for explicit distinction between free-flow and porous regions.

2.5. Rock and structure phase: total Lagrangian formulation

The rock and structure phases are treated as impermeable solid bodies undergoing large deformations while preserving a fixed material topology. To accurately capture their mechanical response and avoid numerical issues associated with particle disorder, a total Lagrangian formulation is adopted. In this framework, all kinematic quantities, differential operators, and constitutive relations are evaluated with respect to the initial reference configuration, which remains unchanged throughout the simulation.

Let $\mathbf{r}_0^{rs} \in \Omega_0^{rs}$ denote the material position of a solid particle in the initial reference configuration, and $\mathbf{r}^{rs} = \boldsymbol{\varphi}(\mathbf{r}_0^{rs}, t)$ its current position at time t. The displacement vector is defined as:

$$\mathbf{u}^{rs} = \mathbf{r}^{rs} - \mathbf{r}_0^{rs}. \tag{32}$$

Accordingly, the deformation gradient tensor is given by:

$$\mathbb{F} = \frac{\partial \mathbf{r}^{rs}}{\partial \mathbf{r}_0^{rs}} = \nabla_0 \mathbf{u}^{rs} + \mathbf{I}, \tag{33}$$

where ∇_0 denotes the gradient operator with respect to the reference configuration, and $\mathbf{I}$ is the identity tensor. The Jacobian determinant of deformation is defined as $J = \det(\mathbb{F})$.

Within the TL framework, mass conservation is inherently satisfied and can be expressed as:

$$\rho^{rs} = J^{-1} \rho_0^{rs}, \tag{34}$$

where ρ_0^{rs} and ρ^{rs} are the initial and current densities of rocks/structures, respectively.

The conservation of linear momentum for the rock and structure phases is written as:

$$\rho_0^{rs} \frac{\mathrm{d}\mathbf{v}^{rs}}{\mathrm{d}t} = \nabla_0 \cdot \mathbb{P}^T + \rho_0^{rs} \boldsymbol{g} + \boldsymbol{f}^{rs \leftarrow s} + \boldsymbol{f}^{rs \leftarrow w}, \tag{35}$$

where $\mathbf{v}^{rs}$ is the particle velocity, $\boldsymbol{g}$ denotes gravitational acceleration. $\boldsymbol{f}^{rs \leftarrow s}$ and $\boldsymbol{f}^{rs \leftarrow w}$ represent external forces arising from interactions with surrounding soil and water phases, respectively. Here, $\mathbb{P}$ is the first Piola–Kirchhoff stress tensor, which relates forces in the current configuration to areas in the reference configuration.

To close the governing equations, a constitutive relation is required to relate stress to deformation. For elastic solids, the first Piola–Kirchhoff stress tensor is related to the second Piola–Kirchhoff stress tensor $\mathbb{S}$ through:

$$\mathbb{P} = \mathbb{F}\mathbb{S}. \tag{36}$$

The second Piola–Kirchhoff stress tensor is evaluated from a constitutive model defined in terms of the Green–Lagrangian strain tensor.

$$\mathbb{E} = \frac{1}{2}\left(\mathbb{F}^T\mathbb{F} - \mathbf{I}\right). \tag{37}$$

For finite-strain problems, a St. Venant–Kirchhoff hyperelastic model may be employed, yielding:

$$\mathbb{S} = K\,\mathrm{tr}(\mathbb{E})\,\mathbf{I} + 2G\left(\mathbb{E} - \tfrac{1}{3}\mathrm{tr}(\mathbb{E})\,\mathbf{I}\right) = \lambda\,\mathrm{tr}(\mathbb{E})\,\mathbf{I} + 2\mu\,\mathbb{E}, \tag{38}$$

where λ and μ are the Lamé parameters, related to the bulk modulus K and shear modulus G by $K = \lambda + 2\mu/3$ and $G = \mu$.

To account for large deformations and geometric nonlinearities, a Neo-Hookean model is adopted in this work. The strain-energy density function is defined as [59]:

$$\mathbb{W} = \mu\,\mathrm{tr}(\mathbb{E}) - \mu \ln J + \frac{\lambda}{2}(\ln J)^2, \tag{39}$$

from which the second Piola–Kirchhoff stress tensor is obtained as:

$$\mathbb{S} = \frac{\partial \mathbb{W}}{\partial \mathbb{E}} = \mu\left(\mathbf{I} - \mathbb{C}^{-1}\right) + \lambda(\ln J)\,\mathbb{C}^{-1}, \tag{40}$$

where $\mathbb{C} = \mathbb{F}^T\mathbb{F}$ is the right Cauchy–Green deformation tensor.

In the present study, the rock and structure phases are assumed to remain purely elastic, and material failure or fragmentation is not considered. This assumption is reasonable for the problems investigated herein, as the deformation of intact rock blocks and structural components remains limited. Nevertheless, for extreme loading conditions involving high-speed impacts or intense collisions, more advanced damage or fracture models would be required.

The total-Lagrangian formulation is adopted for the rock and structure phases, rather than the updated-Lagrangian treatment used for the soil phase, because these bodies are assumed to remain elastic and to preserve their material topology. In TLSPH, the kernel functions, particle interactions, and correction matrices are evaluated in the fixed initial configuration. Consequently, the internal particle arrangement is not distorted by the current deformation, which avoids the conventional tensile instability and particle-disorder problems associated with updated-Lagrangian SPH formulations. In addition, the internal neighbor configuration and kernel-gradient corrections can be precomputed and reused throughout the simulation, eliminating the need to update the rock/structure particle configuration at every time step and thereby reducing the computational cost.

3. SPH discretization and interaction modeling

This section details the numerical discretization of the unified framework. The domain is discretized into particles carrying phase information. For the soil–water mixture, the two phases are discretized by two distinct sets of SPH particles, allowing for relative motion.

3.1. SPH discretization

3.1.1. Basic SPH approximations

In the SPH framework, the computational domain is discretized by a set of Lagrangian particles. The value of a scalar field function $f(\mathbf{x})$ at particle i is approximated as:

$$f_i = \sum_j f_j W_{ij} V_j, \tag{41}$$

where $f_i = f(\mathbf{r}_i)$ and $f_j = f(\mathbf{r}_j)$, $\mathbf{r}_i$ and $\mathbf{r}_j$ denote the positions of particles i and j, respectively, and V_j is the volume associated with particle j. The summation is carried out over all particles within the support domain of the kernel function. The kernel function is defined as $W_{ij} = W(\mathbf{r}_{ij}, h)$, where $\mathbf{r}_{ij} = \mathbf{r}_i - \mathbf{r}_j$ and h is the smoothing length.

The gradient of the field function is evaluated in a similar manner as:

$$\nabla f_i = \sum_j f_j \nabla_i W_{ij} V_j, \tag{42}$$

where $\nabla_i W_{ij} = \nabla_i W(\mathbf{r}_{ij}, h) = \frac{\partial W(\mathbf{r}_{ij}, h)}{\partial r_{ij}} \mathbf{e}_{ij}$ denotes the gradient of the kernel function evaluated at particle i. $r_{ij} = \left|\mathbf{r}_i - \mathbf{r}_j\right|$ is the distance between particles i and j. Note that the gradient is taken with respect to the coordinates of particle i, and thus $\nabla_i W_{ij} = -\nabla_j W_{ij}$. The unit vector directed from particle j to particle i is represented by $\mathbf{e}_{ij}$. h is the smoothing length that defines the influence radius of the kernel function.

The particle approximation given in Eq. (42) serves as the basic SPH gradient formulation. However, to satisfy specific conservation properties or consistency requirements in mechanics, alternative forms derived from vector identities are typically employed.

Based on the product rule identity $\nabla(\Psi f) = \Psi \nabla f + f \nabla \Psi$, setting the auxiliary scalar field $\Psi = 1$ leads to the relation $\nabla f = \nabla(\Psi f) - f \nabla \Psi$, which simplifies to $\nabla f = \nabla f - f \nabla 1$. Applying the SPH interpolation to the terms on the right-hand side yields the strong form:

$$\nabla f_i = -\sum_j (f_i - f_j) \nabla_i W_{ij} V_j. \tag{43}$$

This form vanishes exactly when the field function f is constant, thereby solving the problem of zeroth-order consistency. It is frequently used for discretizing terms where consistency is prioritized over strict conservation, such as density renormalization or velocity divergence.

Conversely, considering the identity $\nabla f = \nabla f + f \nabla 1$ or deriving from the integral weak form using integration by parts, we obtain:

$$\nabla f_i = \sum_j (f_i + f_j) \nabla_i W_{ij} V_j. \tag{44}$$

Eq. (44) involves the symmetric operand $(f_i + f_j)$. Combined with the antisymmetry of the kernel gradient ($\nabla_i W_{ij} = -\nabla_j W_{ji}$), this form ensures that the interaction forces between particle pairs are equal and opposite (strictly conservative). Consequently, this form is widely adopted for discretizing the pressure gradient term in the momentum equation to ensure the conservation of linear momentum.

3.1.2. Soil phase

The continuity Eq. (8) is discretized to update the soil volume fraction n_i^s carried by soil particle i:

$$\frac{\mathrm{d}n_i^s}{\mathrm{d}t} = \sum_{j \in s} n_j^s \left(\mathbf{v}_i^s - \mathbf{v}_j^s\right) \cdot \nabla_i W_{ij}^s V_j^s, \tag{45}$$

where the summation is performed over neighboring soil particles. The momentum equation (11) for soil is discretized using a stress-based formulation:

$$\frac{\mathrm{d}\mathbf{v}_i^s}{\mathrm{d}t} = \frac{1}{\tilde{\rho}_i^s} \sum_{j \in s} \left(\boldsymbol{\sigma}_i^{s\prime} + \boldsymbol{\sigma}_j^{s\prime}\right) \cdot \nabla_i W_{ij}^s V_j^s + \frac{n_i^s}{\tilde{\rho}_i^s} \sum_{j \in s} (p_i^{s \leftarrow w} - p_j^{s \leftarrow w}) \nabla_i W_{ij}^s V_j^s + \mathbf{g} + \frac{1}{\tilde{\rho}_i^s} \sum_{j \in w} \boldsymbol{f}_{ij}^d W_{ij}^{s \leftarrow w} V_j^w + \frac{1}{\tilde{m}_i^s} \boldsymbol{F}_i^{s \leftarrow rs}, \tag{46}$$

where $\tilde{m}_i^s = \tilde{\rho}_i^s V_i^s$. The drag force density $\boldsymbol{f}^d$ is evaluated using the soil–water viscous drag model described in Section 2.4. Note that the contact force term with rock/structure phases is discretized explicitly. The total contact force $\mathbf{F}_i^{s \leftarrow rs}$ is related to the force density in the governing equation (11) by $\mathbf{F}_i^{s \leftarrow rs} = \boldsymbol{f}_i^{s \leftarrow rs} V_i^s$.

In the above equations, the subscript i in $\mathrm{d}n_i^s/\mathrm{d}t$ and $\mathrm{d}\mathbf{v}_i^s/\mathrm{d}t$ denotes the target particle belonging to the soil phase. The summation indices $j \in s$ and $j \in w$ specify that the neighboring particle j is from the soil phase and the water phase, respectively. Thus, the summation involving the kernel gradient $\nabla_i W_{ij}^s$ is carried out over neighboring soil particles, while the drag force term represents the phase-coupling interaction with neighboring water particles. It is noted that the contact forces between the soil phase and structure phases (*e.g.*, rock or structures) are excluded here and will be explicitly defined in Section 3.1.4.

$p_i^{s\leftarrow w}$ is the pore-water pressure at the location of soil particle i, which is interpolated from neighboring water particles as:

$$p_i^{s\leftarrow w} = \frac{\sum_{j\in w} p_j^w W_{ij}^{s\leftarrow w} V_j^w}{\sum_{j\in w} W_{ij}^{s\leftarrow w} V_j^w}, \tag{47}$$

where the summation index j runs over neighboring water particles within the support domain of soil particle i.

Instead of relying on traditional artificial viscosity terms [24] to suppress numerical oscillation [17,60], which often introduce excessive damping, this study employs a low-dissipation Riemann solver [25,27]. By solving the inter-particle Riemann problem, the necessary numerical dissipation is implicitly introduced into the system, thereby enhancing stability while preserving solution accuracy. Consequently, the governing equations are reformulated based on the Riemann flux integration, as presented in Eqs. (48) and (49). For the sake of brevity, the detailed derivation is omitted here and interested readers are referred to Ref. [27].

$$\frac{\mathrm{d}n_i^s}{\mathrm{d}t} = 2\sum_{j\in s} n_j^s \left(\mathbf{v}_i^s - \mathbf{v}^{s*}\right)\cdot \nabla_i W_{ij}^s V_j^s, \tag{48}$$

$$\frac{\mathrm{d}\mathbf{v}_i^s}{\mathrm{d}t} = \frac{2}{\tilde{\rho}_i^s}\sum_{j\in s} \boldsymbol{\sigma}^{s*}\cdot\nabla_i W_{ij}^s V_j^s + \frac{n_i^s}{\tilde{\rho}_i^s}\sum_{j\in s}(p_i^{s\leftarrow w} - p_j^{s\leftarrow w})\nabla_i W_{ij}^s V_j^s + \mathbf{g} + \frac{1}{\tilde{\rho}_i^s}\sum_{j\in w} \boldsymbol{f}_{ij}^d W_{ij}^{s\leftarrow w} V_j^w + \frac{1}{\tilde{m}_i^s}\boldsymbol{F}_i^{s\leftarrow rs}, \tag{49}$$

where $\mathbf{v}^{s*}$ and $\boldsymbol{\sigma}^{s*}$ are the intermediate Riemann solutions, and are expressed as:

$$\begin{cases} \mathbf{v}^{s*} = \overline{\mathbf{v}}_{ij}^s - \left(U^{s*} - \overline{U}^s\right)\mathbf{e}_{ij} \\ \boldsymbol{\sigma}^{s*} = \overline{\boldsymbol{s}}_{ij}' - P^{s*}\mathbf{I} \end{cases}, \tag{50}$$

where $\overline{U}^s = (U_L^s + U_R^s)/2$. $\overline{\mathbf{v}}_{ij}^s = (\mathbf{v}_i^s + \mathbf{v}_j^s)/2$ and $\overline{\boldsymbol{s}}_{ij}' = (\boldsymbol{s}_i' + \boldsymbol{s}_j')/2$ are the particle-average velocity and deviatoric effective stress, respectively.

The scalar solutions U^{s*} and P^{s*} are obtained from the one-dimensional inter-particle Riemann problem along the unit vector $\mathbf{e}_{ij}$:

$$\begin{cases} U^{s*} = \dfrac{\rho_{0L}^s c_{0L}^s U_L^s + \rho_{0R}^s c_{0R}^s U_R^s + P_L^{s\prime} - P_R^{s\prime}}{\rho_{0L}^s c_{0L}^s + \rho_{0R}^s c_{0R}^s} \\ P^{s*} = \dfrac{\rho_{0L}^s c_{0L}^s P_R^{s\prime} + \rho_{0R}^s c_{0R}^s P_L^{s\prime} + \beta^s \rho_{0L}^s c_{0L}^s \rho_{0R}^s c_{0R}^s \left(U_L^s - U_R^s\right)}{\rho_{0L}^s c_{0L}^s + \rho_{0R}^s c_{0R}^s} \end{cases}, \tag{51}$$

where $P^{s\prime}$ denotes the mean effective stress, defined as $P^{s\prime} = -\frac{1}{3}\mathrm{tr}(\boldsymbol{\sigma}^{s\prime})$. In these expressions, the left (L) and right (R) states correspond to the variables of particle i and j, and are defined as follows:

$$\begin{cases} (\rho_{0L}^s, U_L^s, P_L^{s\prime}, c_{0L}^s) = (\rho_{0i}^s, -\mathbf{v}_i^s\cdot\mathbf{e}_{ij}, P_i^{s\prime}, c_{0i}^s) \\ (\rho_{0R}^s, U_R^s, P_R^{s\prime}, c_{0R}^s) = (\rho_{0j}^s, -\mathbf{v}_j^s\cdot\mathbf{e}_{ij}, P_j^{s\prime}, c_{0j}^s) \end{cases}. \tag{52}$$

The wave speed of the soil skeleton c^s is determined by:

$$c_0^s = \sqrt{\frac{K}{\rho_0^s}}, \tag{53}$$

where K is the bulk modulus and ρ_0^s is the initial density of the soil skeleton. To minimize excessive numerical dissipation, the limiter β^s is applied as follows [25]:

$$\beta^s = \min\left\{\xi^s \max\left[\frac{(\rho_{0L}^s + \rho_{0R}^s)(U_L^s - U_R^s)}{\rho_{0L}^s c_{0L}^s + \rho_{0R}^s c_{0R}^s}, 0\right], 1.0\right\}, \tag{54}$$

where ξ^s is a dimensionless coefficient, typically set to $20d$ (with d being the spatial dimension) for soils [27,43].

The velocity gradient $\nabla\mathbf{v}$ in Eqs. (16) can be discretized as:

$$\nabla\mathbf{v}_i^s = \sum_{j\in s}\left(\mathbf{v}_j^s - \mathbf{v}_i^s\right)\otimes\nabla_i W_{ij}^s V_j^s \tag{55}$$

3.1.3. Water phase

For the water phase, a weakly compressible intrinsic-density formulation is adopted. The water particles are advected by the pore-average velocity $\mathbf{v}^w$, while the representative particle volume is updated from Eq. (27). In the multi-layer SPH framework, the water volume fraction is evaluated at the locations of water particles. Since the soil phase is treated as the active phase, the solid

volume fraction at a water particle is obtained through kernel interpolation of the surrounding soil particles. Under the saturation assumption:

$$n_i^w = 1 - n_i^s = 1 - \sum_{j\in s} n_j^s W_{ij}^{w\leftarrow s} V_j^s, \tag{56}$$

where the summation is performed over neighboring soil particles j within the support domain of water particle i. The soil velocity at a water-particle position is interpolated as:

$$\mathbf{v}_i^{s\to w} = \frac{\sum_{j\in s} \mathbf{v}_j^s W_{ij}^{w\leftarrow s} V_j^s}{\sum_{j\in s} W_{ij}^{w\leftarrow s} V_j^s}. \tag{57}$$

The intrinsic-density continuity equation in Eq. (23) is then discretized as:

$$\frac{\mathrm{d}\rho_i^w}{\mathrm{d}t} = \frac{\rho_i^w}{n_i^w} \sum_{j\in w} \left[n_i^w \mathbf{v}_i^w - n_j^w \mathbf{v}_j^w - \left(1 - n_j^w\right) \mathbf{v}_j^{s\to w} \right] \cdot \nabla_i W_{ij}^w V_j^w + 2\rho_i^w \sum_{j\in w} \frac{p_i^w - p_j^w}{\rho_{0i}^w c_{0i}^w + \rho_{0j}^w c_{0j}^w} \frac{\partial W_{ij}^w}{\partial r_{ij}} V_j^w. \tag{58}$$

The last term in Eq. (58) is the Riemann density-dissipation term [25]. This form accounts for the spatial variation of the water volume fraction as water particles cross the clear-fluid/porous-medium interface [36].

The momentum equation for the water phase, given in Eq. (25), is discretized as [19,36]:

$$\begin{aligned} \frac{\mathrm{d}\mathbf{v}_i^w}{\mathrm{d}t} = & -\frac{1}{\rho_i^w} \sum_{j\in w} (p_i^w + p_j^w) \nabla_i W_{ij}^w V_j^w + \frac{1}{\tilde{\rho}_i^w} \sum_{j\in w} \eta \frac{\left(n_i^w + n_j^w\right) \mathbf{r}_{ij} \cdot \nabla_i W_{ij}^w}{r_{ij}^2 + 0.01(h^w)^2} V_j^w \left(\mathbf{v}_i^w - \mathbf{v}_j^w\right) \\ & + \mathbf{g} - \frac{1}{\tilde{\rho}_i^w} \sum_{j\in s} (\boldsymbol{f}_{ij}^d) W_{ij}^{w\leftarrow s} V_j^s + \frac{1}{\tilde{m}_i^w} \boldsymbol{F}_i^{w\leftarrow rs}, \end{aligned} \tag{59}$$

where $\tilde{m}_i^w = \tilde{\rho}_i^w V_i^w$. $\boldsymbol{F}_i^{w\leftarrow rs} = \boldsymbol{f}_i^{w\leftarrow rs} V_i^w$ is the total contact force acting on water particle i from rock/structure phases. In the discretized formulations above, the subscript i denotes the target particle belonging to the water phase. The summations involving the fluid kernel gradient $\nabla_i W_{ij}^w$ (in the continuity and momentum equations) represent intra-phase interactions and are performed over neighboring water particles. Conversely, the terms for evaluating the water volume fraction and the drag force represent phase-coupling interactions; hence, the summation index j in these specific terms refers to neighboring soil particles, utilizing the soil volume V_j^s and the interaction kernel $W_{ij}^{w\leftarrow s}$.

Similar to the treatment of the soil phase, to suppress non-physical pressure fluctuations while minimizing numerical dissipation, the low-dissipation Riemann solver is incorporated into the water phase discretization [25]. The momentum equation is modified by substituting the pressure gradient term with the Riemann pressure flux P^{w*}:

$$\begin{aligned} \frac{\mathrm{d}\mathbf{v}_i^w}{\mathrm{d}t} = & -\frac{2}{\rho_i^w} \sum_{j\in w} P^{w*} \nabla_i W_{ij}^w V_j^w + \frac{1}{\tilde{\rho}_i^w} \sum_{j\in w} \eta \frac{\left(n_i^w + n_j^w\right) \mathbf{r}_{ij} \cdot \nabla_i W_{ij}^w}{r_{ij}^2 + 0.01(h^w)^2} V_j^w \left(\mathbf{v}_i^w - \mathbf{v}_j^w\right) \\ & + \mathbf{g} - \frac{1}{\tilde{\rho}_i^w} \sum_{j\in s} (\boldsymbol{f}_{ij}^d) W_{ij}^{w\leftarrow s} V_j^s + \frac{1}{\tilde{m}_i^w} \boldsymbol{F}_i^{w\leftarrow rs}. \end{aligned} \tag{60}$$

The intermediate Riemann solutions for velocity $\mathbf{v}^{w*}$ and pressure P^{w*} are constructed following the same reconstruction protocol as the soil phase, expressed as:

$$\begin{cases} \mathbf{v}^{w*} = \overline{\mathbf{v}}_{ij}^w - \left(U^{w*} - \overline{U}^w\right) \mathbf{e}_{ij} \\ U^{w*} = \dfrac{\rho_{0L}^w c_{0L}^w U_L^w + \rho_{0R}^w c_{0R}^w U_R^w + P_L^w - P_R^w}{\rho_{0L}^w c_{0L}^w + \rho_{0R}^w c_{0R}^w} \\ P^{w*} = \dfrac{\rho_{0L}^w c_{0L}^w P_R^w + \rho_{0R}^w c_{0R}^w P_L^w + \beta^w \rho_{0L}^w c_{0L}^w \rho_{0R}^w c_{0R}^w \left(U_L^w - U_R^w\right)}{\rho_{0L}^w c_{0L}^w + \rho_{0R}^w c_{0R}^w} \end{cases}, \tag{61}$$

where $\overline{\mathbf{v}}_{ij}^w = (\mathbf{v}_i^w + \mathbf{v}_j^w)/2$ is the inter-particle average velocity, and $\overline{U}^w = (U_L^w + U_R^w)/2$.

Here, c_0^w is the artificial speed of sound in water. The left (L) and right (R) states are defined by projecting the fluid variables along the interaction vector:

$$\begin{cases} (\rho_{0L}^w, U_L^w, P_L^w, c_{0L}^w) = (\rho_{0i}^w, -\mathbf{v}_i^w \cdot \mathbf{e}_{ij}, p_i^w, c_{0i}^w) \\ (\rho_{0R}^w, U_R^w, P_R^w, c_{0R}^w) = (\rho_{0j}^w, -\mathbf{v}_j^w \cdot \mathbf{e}_{ij}, p_j^w, c_{0j}^w) \end{cases}. \tag{62}$$

The dissipation limiter β^w is defined as:

$$\beta^w = \min\left\{ \xi^w \max\left[\frac{(\rho_{0L}^w + \rho_{0R}^w)(U_L^w - U_R^w)}{\rho_{0L}^w c_{0L}^w + \rho_{0R}^w c_{0R}^w}, 0 \right], 1.0 \right\}, \tag{63}$$

Here, ξ^w in the limiter is set to 3 for water [25].

3.1.4. Rock and structure phase

The discretization of the rock and structure phases is established within the TLSPH framework. Unlike the formulation used for soil and water phases, spatial derivatives here are evaluated with respect to the initial reference configuration Ω_0^{rs}. Thanks to the Lagrangian nature of the method, the explicit time integration of the mass continuity equation is circumvented. Instead, the density of particle i at the current configuration, ρ_i^{rs}, is algebraically updated via the Jacobian determinant J:

$$\rho_i^{rs} = \rho_{0i}^{rs}\frac{1}{J_i} = \rho_{0i}^{rs}\frac{1}{\det(\mathbb{F}_i)}, \tag{64}$$

where ρ_{0i}^{rs} denotes the initial reference density.

Regarding the momentum conservation, the internal force is computed utilizing the first Piola–Kirchhoff stress tensor $\mathbb{P}$. To address the incomplete support domain issue and guarantee first-order consistency (linear preservation) of the SPH approximation, a kernel gradient correction matrix $\mathbb{B}_0$ is incorporated into the formulation. The momentum equation is thus discretized as [61,62]:

$$\frac{\mathrm{d}\mathbf{v}_i^{rs}}{\mathrm{d}t} = \frac{1}{\rho_{0i}^{rs}}\sum_{j\in rs}\left[\mathbb{P}_i(\mathbb{B}_{0i})^{\mathrm{T}} + \mathbb{P}_j(\mathbb{B}_{0j})^{\mathrm{T}}\right]\cdot\nabla_{0i}W_{ij}V_{0j}^{rs} + \mathbf{g} + \frac{1}{m_i^{rs}}\boldsymbol{F}_i^{rs\leftarrow s} + \frac{1}{m_i^{rs}}\boldsymbol{F}_i^{rs\leftarrow w} + \frac{1}{m_i^{rs}}\boldsymbol{F}_i^{c}, \tag{65}$$

where $\boldsymbol{F}_i^{c}$ represents the contact force among rock particles and between rocks and structures. $\boldsymbol{F}_i^{rs\leftarrow s}$ and $\boldsymbol{F}_i^{rs\leftarrow w}$ denote the coupling forces exerted by the soil and water phases, respectively. These interaction forces will be elaborated in Section 3.2.

The correction matrix $\mathbb{B}_{0i}$, which is computed solely based on the initial particle distribution, serves as a renormalization term for the gradient operator. It is defined as the inverse of the moment matrix [63–65]:

$$\mathbb{B}_{0i} = \left[\sum_j\left(\mathbf{r}_j^{rs,0} - \mathbf{r}_i^{rs,0}\right)\otimes\nabla_{0i}W_{ij}V_{0j}^{rs}\right]^{-1}. \tag{66}$$

Note that since the reference configuration is fixed, $\mathbb{B}_{0i}$ is computed only once at the beginning of the simulation, incurring minimal computational cost.

The kinematic evolution of the solid phase is driven by the deformation gradient tensor $\mathbb{F}$. Its temporal rate of change is discretized using the relative velocities of neighboring particles [61]:

$$\frac{\mathrm{d}\mathbb{F}_i}{\mathrm{d}t} = \sum_{j\in rs}\left(\mathbf{v}_j^{rs} - \mathbf{v}_i^{rs}\right)\otimes\nabla_{0i}W_{ij}V_{0j}^{rs}\mathbb{B}_{0i}. \tag{67}$$

3.2. Modeling of multiphase interactions

This section details the computation of coupling forces between the soil and rock/structure phases, as well as the interaction forces between the water and rock/structure phases. Additionally, the mechanical contact interactions among rock particles, as well as those between rocks and structures, are explicitly formulated.

3.2.1. Soil–water interaction

The mechanical interaction between the soil and water phases is governed by both viscous drag force and buoyancy. While the buoyancy effect is inherently captured by the pore-water pressure gradient within the governing equations of the respective phases (Eqs. (11) and (25)), the specific formulation for the viscous drag force is detailed in Section 2.4.

This section primarily outlines the calculation of the degree of saturation [18]. Essentially, this study considers two extreme saturation states for the soil phase. When no water particles exist within the support domain of a soil particle, it is defined as a dry condition (Fig. 2a), yielding $S_r = 0$. Conversely, when the support domain is completely occupied by water particles, it is defined as a fully saturated condition (Fig. 2c), yielding $S_r = 1$. However, for soil particles situated at the soil–water interface, their support domains are only partially occupied by water (Fig. 2b). This specific area is defined as the transition zone [18].

The degree of saturation for a given soil particle is calculated based on its neighboring water particles as follows:

$$S_{ri} = \sum_{j\in w}\frac{\tilde{m}_j^w}{\tilde{\rho}_j^w}W_{ij}^{s\leftarrow w}. \tag{68}$$

Specifically, soil particles containing water particles within their support domains are first identified as *mixture* particles. For these particles within the transition zone, the partial presence of water particles naturally leads to a degree of saturation S_r strictly between 0 and 1. Here, the intermediate value $0 < S_r < 1$ serves only as a numerical indicator of the soil–water interface, arising from the partial occupation of a soil particle's support domain by neighboring water particles; it does not represent a physically modeled unsaturated state. For mixture particles located near the boundaries, the contribution from boundary particles is explicitly incorporated into Eq. (68) to prevent unphysically low saturation values caused by kernel truncation.

Unless otherwise stated, S_r is retained only as a diagnostic quantity for visualization and post-processing and does not enter the mass and momentum equations or the soil–water interaction forces. When a saturation-dependent material property is explicitly prescribed, however, S_r can be used as a local wetting indicator to update that property. For example, in the rainfall-induced bouldery debris-flow case in Section 6.1, S_r is used in Eq. (108) to interpolate the soil cohesion between its initial and saturated values, thereby affecting the simulation through the constitutive stress response. This empirical use does not introduce an unsaturated-soil formulation involving suction or capillary pressure.

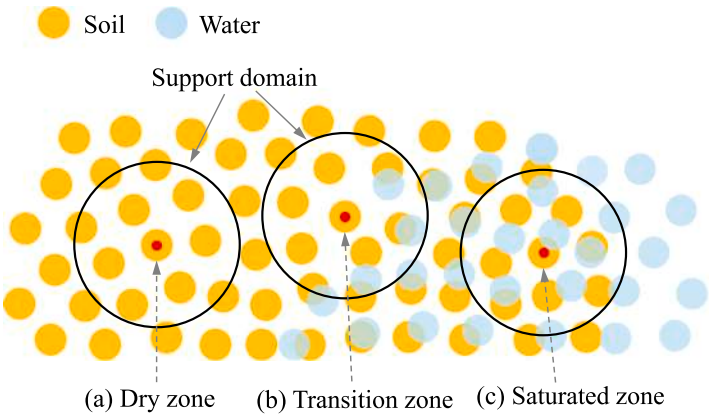

Fig. 2. Schematic of dry, transition, and saturated zones defined by the support domain of soil particles.

3.2.2. Soil–rock/structure interaction

For the interaction between the soil phase and rock/structure phases, the rock and structure phases are treated as moving boundaries, imposing contact constraints via repulsive forces to prevent penetration, while a no-slip boundary condition is enforced at the interface.

The total contact force exerted by the rock/structure phase on a soil particle i, denoted as $\mathbf{F}_i^{s\leftarrow rs}$, is computed by integrating the stress tensor over the neighboring rock/structure particles [43]:

$$\mathbf{F}_i^{s\leftarrow rs} = \sum_{j\in rs} \left\{ 2\tilde{\boldsymbol{\sigma}}_i^s \cdot \mathbf{e}_{ij}^{s\leftarrow rs} + \beta^s \rho_{0i}^s c_{0i}^s \left[(\mathbf{v}_i^s - \mathbf{v}_j^{rs,d}) \cdot \mathbf{n}_j^{rs} \right] \mathbf{n}_j^{rs} \right\} \frac{\partial W_{ij}^{s\leftarrow rs}}{\partial r_{ij}} V_i^s V_j^{rs}, \tag{69}$$

where the summation is performed over the neighboring rock/structure particles j. $\mathbf{v}_j^{rs,d} = 2\mathbf{v}_j^{rs} - \mathbf{v}_i^s$ is the imaginary velocity of rock/structure particle j used to enforce the no-slip boundary condition at the Soil–rock/structure interface. W_{ij}^{s-rs} is the kernel function calculated using the smoothing length of the soil phase.

The reaction force exerted by the soil phase on a rock/structure particle i is given by [43]:

$$\mathbf{F}_i^{rs\leftarrow s} = \sum_{j\in s} \left\{ 2\tilde{\boldsymbol{\sigma}}_j^s \cdot \mathbf{e}_{ij}^{rs\leftarrow s} - \beta^s \rho_{0j}^s c_{0j}^s \left[(\mathbf{v}_j^s - \mathbf{v}_i^{rs,d}) \cdot \mathbf{n}_i^{rs} \right] \mathbf{n}_i^{rs} \right\} \frac{\partial W_{ij}^{rs\leftarrow s}}{\partial r_{ij}} V_i^{rs} V_j^s, \tag{70}$$

where $\mathbf{v}_i^{rs,d} = 2\mathbf{v}_i^{rs} - \mathbf{v}_j^s$ is the imaginary velocity of rock/structure particle i. $\mathbf{n}_j^{rs}$ is the normal direction of rock/structure and is defined as [25]:

$$\mathbf{n}_i^{rs} = -\frac{\sum_{j\in rs} \nabla_i W_{ij}^{rs} V_j^{rs}}{\left| \sum_{j\in rs} \nabla_i W_{ij}^{rs} V_j^{rs} \right|}. \tag{71}$$

These reaction forces (Eqs. (69) and (70)) are then incorporated into the momentum equations of the soil and rock/structure phases (Eqs. (49) and (65)) to govern their motion.

The second term within the braces in Eqs. (69) and (70) represents the numerical dissipation term, which is derived by solving a one-sided Riemann problem [25] along the normal direction of rock/structure particles. Analogously, the wall-boundary conditions for the soil phase are implemented using fixed wall-boundary particles, where the interaction is governed by the same one-sided Riemann formulation. For a detailed implementation of this boundary treatment, readers are referred to Refs. [25,43], and thus the details are omitted here for brevity.

3.2.3. Water–rock/structure interaction

Similar to the soil phase, the rock and structure phases function as moving solid boundaries for the water phase, where a no-slip boundary condition is enforced at the water–structure interface.

The total contact force $\mathbf{F}_i^{w\leftarrow rs}$ exerted by the rock/structure phase on a water particle i can be divided into two components:

$$\mathbf{F}_i^{w\leftarrow rs} = \mathbf{F}_i^{w\leftarrow rs:p} + \mathbf{F}_i^{w\leftarrow rs:v}, \tag{72}$$

where $\mathbf{F}_i^{w\leftarrow rs:p}$ and $\mathbf{F}_i^{w\leftarrow rs:v}$ represent the pressure and viscous forces acting on water particle i, respectively. Following Refs. [25,66], these forces are computed as:

$$\mathbf{F}_i^{w\leftarrow rs:p} = -\sum_{j\in rs} \left\{ \left(p_i^w + p_j^{rs,d} \right) \mathbf{e}_{ij}^{w\leftarrow rs} - \beta^w \rho_{0i}^w c_{0i}^w \left[(\mathbf{v}_i^w - \mathbf{v}_j^{rs,d}) \cdot \mathbf{n}_j^{rs} \right] \mathbf{n}_j^{rs} \right\} \frac{\partial W_{ij}^{w\leftarrow rs}}{\partial r_{ij}} V_i^w V_j^{rs}, \tag{73}$$

$$\mathbf{F}_i^{w\leftarrow rs:v} = 2\sum_{j\in rs}\eta\frac{\mathbf{r}_{ij}\cdot\nabla_i W_{ij}^{w\leftarrow rs}}{r_{ij}^2+0.01(h^w)^2}\left(\mathbf{v}_i^w-\mathbf{v}_j^{rs,d}\right)V_i^w V_j^{rs}. \tag{74}$$

$p_j^{rs,d} = p_i^w + \rho_i^w \max\left[0,\left(\mathbf{g}-\mathrm{d}v_j^{rs}/\mathrm{d}t\right)\cdot\mathbf{n}_j^{rs}\left(\mathbf{r}_{ij}^{w\leftarrow rs}\cdot\mathbf{n}_j^{rs}\right)\right]$ is the imaginary pressure of rock/structure particle j.

Accordingly, the reaction force exerted by the water phase on a rock/structure particle i is given by:

$$\mathbf{F}_i^{rs\leftarrow w} = \mathbf{F}_i^{rs\leftarrow w:p} + \mathbf{F}_i^{rs\leftarrow w:v}, \tag{75}$$

where $\mathbf{F}_i^{rs\leftarrow w:p}$ and $\mathbf{F}_i^{rs\leftarrow w:v}$ are computed as:

$$\mathbf{F}_i^{rs\leftarrow w:p} = -\sum_{j\in w}\left\{\left(p_i^{rs,d}+p_j^w\right)\mathbf{e}_{ij}^{rs\leftarrow w} + \beta^w\rho_{0j}^w c_{0j}^w\left[(\mathbf{v}_j^w-\mathbf{v}_i^{rs,d})\cdot\mathbf{n}_i^{rs}\right]\mathbf{n}_i^{rs}\right\}\frac{\partial W_{ij}^{rs\leftarrow w}}{\partial r_{ij}}V_i^{rs}V_j^w, \tag{76}$$

$$\mathbf{F}_i^{rs\leftarrow w:v} = 2\sum_{j\in w}\eta\frac{\mathbf{r}_{ij}\cdot\nabla_i W_{ij}^{rs\leftarrow w}}{r_{ij}^2+0.01(h^w)^2}\left(\mathbf{v}_i^{rs,d}-\mathbf{v}_j^w\right)V_i^{rs}V_j^w, \tag{77}$$

where $p_i^{rs,d} = p_j^w + \rho_j^w \max\left[0,\left(\mathbf{g}-\mathrm{d}v_i^{rs}/\mathrm{d}t\right)\cdot\mathbf{n}_i^{rs}\left(\mathbf{r}_{ij}^{rs\leftarrow w}\cdot\mathbf{n}_i^{rs}\right)\right]$ is the imaginary pressure of rock/structure particle i.

The second term within the braces in Eqs. (73) and (76) represents the numerical dissipation term derived from a one-sided Riemann problem along the normal direction of rock/structure particles, similar to that in the Soil–rock/structure interaction. The wall boundary conditions for the water phase are also implemented using fixed wall-boundary particles, following the same one-sided Riemann formulation [25].

3.2.4. Rock-rock and rock-structure interaction

To resolve the mechanical contact between discrete rock bodies or between rock and structural components, a density-based contact model is employed. Drawing an analogy to the hydrodynamic pressure formulation in SPH, this method treats the penetration between solid bodies as a localized increase in a fictitious density, which in turn generates a repulsive force to separate the contacting bodies [67].

When a rock/structure particle i comes into contact with another solid body (indexed by j), a contact density ρ_i^c is evaluated. This variable is computed by accumulating the kernel contributions from neighboring particles that are currently within the interaction range but were not part of the initial neighbor list (*i.e.*, belonging to a different body or originally distant) [67]:

$$\rho_i^c = \rho_{0i}^{rs}\sum_{j\in\text{contact}} W(\mathbf{r}_{ij},h^c)V_{0j}^{rs}, \tag{78}$$

where ρ_{0i}^{rs} and V_{0j}^{rs} are the initial density and volume of the rock/structure particles, respectively. The contact smoothing length is defined as the arithmetic mean $h^c = (h_i+h_j)/2$. The summation condition $j\in$ contact encompasses particles satisfying $r_{ij}\le 2h^c$ in the current configuration, while $r_{0ij} > 2h^c$ in the reference configuration, thereby excluding the internal neighbors of the same elastic body to avoid self-repulsion forces.

Based on this contact density, a repulsive contact force $\mathbf{F}_i^c$ acting on particle i is formulated to counteract penetration. By adopting a momentum conservation form similar to the fluid pressure gradient, the contact force is given by [67]:

$$\mathbf{F}_i^c = -2\sum_{j\in\text{contact}}\bar{p}_{ij}^c\nabla_i W(\mathbf{r}_{ij},h^c)V_i^{rs}V_j^{rs}, \tag{79}$$

where the inter-particle average contact pressure is $\bar{p}_{ij}^c = 0.5(p_i^c+p_j^c)$. The contact pressure p^c is related to the contact density via an equation of state-like relation: $p_i^c = \rho_i^c(c_{0i}^{rs})^2$ and $p_j^c = \rho_j^c(c_{0j}^{rs})^2$ where c_0^{rs} represents the sound speed of the rock/structure phase and can be calculated by Eq. (53).

3.3. Level-set-guided porosity-consistent particle relaxation

For cases in which water and soil overlap at the initial time, such as saturated beds, submerged granular deposits, or seepage domains, the water particles inside the mixture region must represent the pore volume prescribed by the porosity field from the beginning of the computation. In the initialization adopted by Zhu et al. [36], water particles in the clear-fluid and mixture regions were assigned the same initial geometric volume, while their masses were scaled by the local water volume fraction. This initialization is consistent in terms of mass and apparent density. However, it does not produce an equal-mass water discretization whose initial number density and inter-particle spacing conform to the prescribed porosity. The present procedure addresses this distinct equal-mass initialization problem. The water particles are kept equal-mass, and their representative volume is adjusted according to Eq. (27). Thus, the initial water-particle volume in the mixture region is consistent with the local water volume fraction, while the particle mass remains unchanged.

The particle distribution is generated with the aid of a level-set description of the initial water domain. Following the level-set-based preprocessing and physics-driven relaxation strategies [40,41], the water domain is described by a signed-distance function ζ_w, where $\zeta_w < 0$ denotes the interior of the water body and $\zeta_w = 0$ denotes its boundary. The outward normal direction is:

$$\mathbf{n}^{\mathrm{LS}} = \frac{\nabla\zeta_w}{|\nabla\zeta_w|}. \tag{80}$$

Let n^w_{tar} denote the prescribed initial water volume fraction used for particle generation. In the clear-fluid region, $n^w_{\mathrm{tar}} = 1$, whereas in the saturated porous region $n^w_{\mathrm{tar}} = 1 - n^s_0$. For equal-mass water particles with $m^w_i = m^w_0$, the target representative volume is:

$$V^{w,\mathrm{tar}} = \frac{m^w_0}{n^w_{\mathrm{tar}}\rho^w_0}. \tag{81}$$

With dp^w denoting the reference water-particle spacing in the clear-fluid region, the target spacing can be written as:

$$dp^{w,\mathrm{tar}} = \left[V^{w,\mathrm{tar}}\right]^{1/d} = dp^w \left[n^w_{\mathrm{tar}}\right]^{-1/d}. \tag{82}$$

Thus, a smaller water volume fraction gives a larger representative particle volume and a smaller expected number of water particles. In practice, candidate particles are generated on the reference lattice and accepted according to the local value of n^w_{tar}, so that the accepted particles represent the local pore-fluid volume while retaining a uniform particle mass m^w_0.

The accepted water particles are subsequently relaxed inside the level-set-defined water domain. Following the physics-driven relaxation framework [40,41], a pseudo-velocity $\mathbf{v}^r_i$ is introduced as:

$$\frac{\mathrm{d}\mathbf{v}^r_i}{\mathrm{d}t} = \mathbf{a}^w_{p,i}, \tag{83}$$

where $\mathbf{a}^w_{p,i}$ is the pseudo-acceleration induced by a constant background pressure. To make the relaxation consistent with Eq. (81), the pressure-induced pseudo-acceleration is evaluated with the porosity-consistent target representative volume:

$$\mathbf{a}^w_{p,i} = -\frac{2p_0 V^{w,\mathrm{tar}}_i}{m^w_0}\left(\sum_{j\in w,\,\zeta^w_j<0}\nabla_i W^w_{ij} V^{w,\mathrm{tar}}_j + \sum_{\ell,\,\zeta^w_\ell>0}\nabla_i W^w_{i\ell} V^{\mathrm{b}}_\ell\right), \tag{84}$$

where p_0 is the constant background pressure used only in the particle-relaxation process; following Ref. [41], $p_0 = 1$ is used in the present implementation. The quantities $V^{w,\mathrm{tar}}_i$ and $V^{w,\mathrm{tar}}_j$ are computed from Eq. (81). Here, ζ^w_j is the signed distance at water particle j, whereas ζ^w_ℓ and V^{b}_ℓ denote the signed distance and quadrature volume of the ℓth background-mesh point in the level-set correction, respectively. The first summation provides the repulsive contribution from water particles inside the geometry, and the second summation accounts for the truncated kernel support near the boundary.

The particle position is updated in pseudo time as:

$$\mathbf{r}^{k+1}_i = \mathbf{r}^k_i + \frac{1}{2}\left(\Delta t_{r,i}\right)^2 \mathbf{a}^w_{p,i}, \tag{85}$$

where k is the relaxation-step index and $\Delta t_{r,i}$ is the pseudo-time step constrained by the acceleration criterion. The quantities p_0 and $\Delta t_{r,i}$ control only the relaxation path and do not enter the subsequent physical time integration. After each position update, particles that approach or cross the level-set boundary are projected back into the water body by the surface-bounding operation:

$$\mathbf{r}^{\mathrm{b}}_i = \begin{cases} \mathbf{r}_i - \left(\zeta^w_i + \dfrac{1}{2}dp^w\right)\mathbf{n}^{\mathrm{LS}}_i & \zeta^w_i \geq -\dfrac{1}{2}dp^w \\ \mathbf{r}_i & \text{otherwise} \end{cases}, \tag{86}$$

where $\mathbf{r}^{\mathrm{b}}_i$ is the bounded position, ζ^w_i and $\mathbf{n}^{\mathrm{LS}}_i$ are the signed distance and outward normal evaluated at water particle i, respectively, and $dp^w/2$ is the prescribed distance from the particle center to the level-set boundary in the bounding step. After each relaxation sweep, the water volume fraction is recomputed at the water-particle positions and the representative volume is synchronized through Eq. (27). The resulting initialization differs from the standard level-set preprocessing in that the representative water-particle volume follows the local pore-fluid volume rather than the geometric volume alone. It also differs from the variable-mass initialization in Ref. [36], since the mixture-region water volume is represented by a larger particle volume rather than by a reduced particle mass.

The performance of the level-set-guided porosity-consistent particle relaxation is illustrated in Fig. 3. A submerged porous medium is considered, where the water particles overlap with the soil skeleton from the initial state. Two porosity distributions are tested. In Fig. 3(a), a uniform porosity of 0.5 is prescribed; in Fig. 3(b), the porosity decreases linearly from 0.5 at the top of the porous medium to 0.2 at the bottom. At relaxation step 0, the water particles inside the porous region are randomly generated according to the prescribed pore-fluid volume. As the relaxation proceeds, the initially disordered particles gradually evolve into a regular distribution while preserving the porosity-dependent particle density. After 100 relaxation steps [40], the water particles form a smooth and stable initial configuration. For the non-uniform porosity case, the final distribution clearly shows a decreasing water-particle volume fraction from the upper part to the lower part of the porous medium, consistent with the prescribed porosity field. The relaxed configuration can be stored and reused for simulations sharing the same initial geometry and porosity field. The relaxation is therefore treated as an offline preprocessing step.

3.4. Porosity-consistent unified transport-velocity formulation

Particle regularization in SPH is commonly achieved through particle-shifting techniques [68–70] or transport-velocity formulations [26,71]. In the present work, the unified transport-velocity formulation (UTVF) [26] is adopted for water-particle regularization. Within the present IDF–VA implementation, the volume-weighted UTVF can reflect spatial variations in the

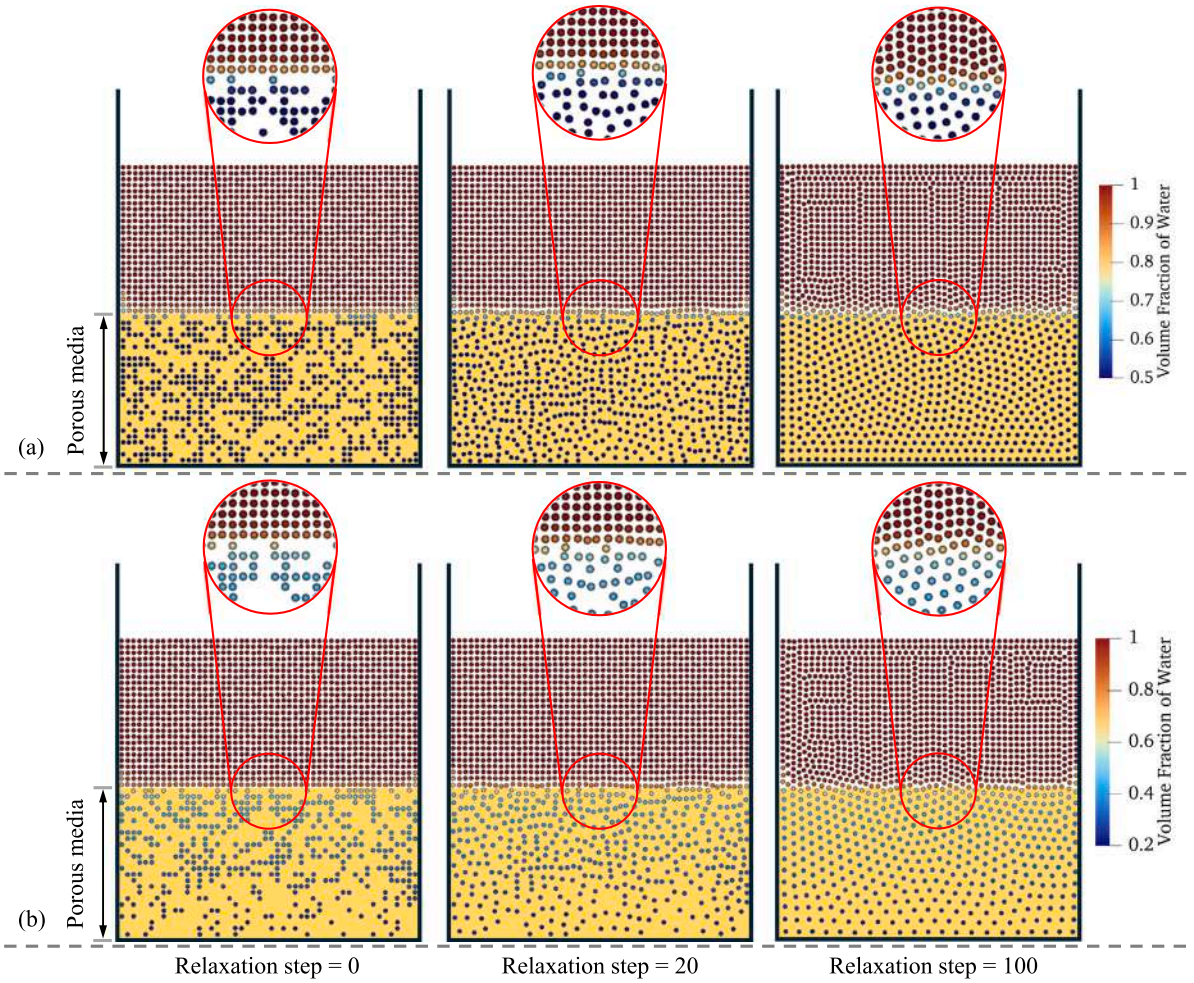

Fig. 3. Level-set-guided porosity-consistent particle relaxation: evolution of water-particle distributions in a submerged porous medium. (a) Uniform porosity of 0.5; (b) linearly varying porosity from 0.5 at the top to 0.2 at the bottom.

representative water-particle volume. However, its artificial transport correction is not constrained by the direction of the porosity gradient. Near a sharp transition in water volume fraction, it may therefore introduce an artificial displacement normal to the transition, even when the corresponding variation in particle spacing is required by the local porosity. The formulation is extended here by defining a porosity-dependent target volume and by conditionally projecting the artificial transport displacement near sharp porosity gradients.

In its original form, the additional transport displacement is written as [26]:

$$\Delta\mathbf{r}_i^{\mathrm{UTVF}} = \begin{cases} 2\alpha h^2 \sum_j \nabla_i W_{ij} V_j & i \notin \Gamma_f^w \\ 2\alpha h^2 \left(\mathbf{I} - \widetilde{\mathbf{n}}_i \otimes \widetilde{\mathbf{n}}_i\right) \cdot \sum_j \nabla_i W_{ij} V_j & i \in \Gamma_f^w \end{cases}, \tag{87}$$

where $\alpha = 0.2$ is the transport coefficient, Γ_f^w denotes the set of free-surface water particles, and $\widetilde{\mathbf{n}}_i$ is the corrected free-surface normal [26]. For the present water phase, the representative volume $V_i^w = m_i^w/(n_i^w \rho_i^w)$ contains both the porosity-dependent volume variation and the instantaneous density variation associated with weak compressibility. The volume in the regularization term is therefore replaced by the reference-density target volume $V_i^{w,\mathrm{tar}} = m_i^w/\rho_0^w n_i^w$, so that the target particle spacing is determined by the local water volume fraction rather than by instantaneous density fluctuations.

The porosity-consistent transport displacement used in the present simulations is then expressed as

$$\Delta\mathbf{r}_i^{w,\mathrm{pc}} = \begin{cases} 2\alpha h^2 \mathbf{P}_i^p \cdot \sum_{j\in w} \nabla_i W_{ij}^w V_j^{w,\mathrm{tar}} & i \notin \Gamma_f^w \\ 2\alpha h^2 \mathbf{P}_i^p \cdot \left(\mathbf{I} - \widetilde{\mathbf{n}}_i \otimes \widetilde{\mathbf{n}}_i\right) \cdot \sum_{j\in w} \nabla_i W_{ij}^w V_j^{w,\mathrm{tar}} & i \in \Gamma_f^w \end{cases}. \tag{88}$$

The two modifications in Eq. (88) serve distinct purposes. The target-volume weighting defines the porosity-dependent particle spacing to be preserved by the regularization procedure. The operator $\mathbf{P}_i^p$ acts only on the additional artificial transport displacement and is introduced to prevent this regularization step from smoothing out a sharp porosity-induced spacing transition. It does not directly modify the physical advection velocity, pressure force, viscous force, drag force, or density evolution.

The target-volume-weighted porosity gradient and the corresponding projection operator are evaluated as

$$\mathbf{P}_i^p = \begin{cases} \mathbf{I} - \mathbf{n}_i^p \otimes \mathbf{n}_i^p & h^w |\mathbf{q}_i^n| > \gamma_p \\ \mathbf{I} & \text{otherwise} \end{cases} \qquad \mathbf{q}_i^n = \sum_{j \in w} \left(n_j^w - n_i^w \right) \nabla_i W_{ij}^w V_j^{w,\mathrm{tar}} \qquad \mathbf{n}_i^p = \frac{\mathbf{B}_i \mathbf{q}_i^n}{|\mathbf{B}_i \mathbf{q}_i^n|}. \tag{89}$$

Here, $\mathbf{q}_i^n$ is the target-volume-weighted porosity-gradient vector, and the correction matrix for the kernel gradient is evaluated from the same target-volume-weighted neighbor configuration as $\mathbf{B}_i = -\left(\sum_{j \in w} \mathbf{r}_{ij} \otimes \nabla_i W_{ij}^w V_j^{w,\mathrm{tar}} \right)^{-1}$ [63]. The parameter γ_p is the prescribed threshold for activating the porosity-gradient projection, with $\gamma_p = 0.1$ used in the present simulations.

When the projection is activated, $\mathbf{P}_i^p$ removes only the component of the artificial transport displacement parallel to the local porosity-gradient direction $\mathbf{n}_i^p$, while retaining the tangential component for particle regularization. It therefore does not force the artificial displacement to vanish and does not prevent physical water-particle motion normal to the interface caused by advection, pressure, gravity, or interphase drag. For smoothly varying porosity fields, $\mathbf{P}_i^p = \mathbf{I}$ and the target-volume-weighted transport correction is recovered.

Finally, the transport-corrected position is written as $\mathbf{r}_i^{\mathrm{tc}} = \mathbf{r}_i + \Delta \mathbf{r}_i^{w,\mathrm{pc}}$. Following the transport correction, n_i^w is reconstructed from the updated particle configuration and V_i^w is updated through Eq. (27). Thus, the porosity-consistent correction enters through the target volume $V_j^{w,\mathrm{tar}}$ in Eq. (88) and through the conditional projection that removes the artificial transport component normal to sharp gradients of n^w.

The density-based particle-shifting formulation of Tsuji et al. [39] similarly seeks consistency among porosity, apparent density, and particle volume for a prescribed porous-medium description, whereas the present formulation evaluates the target volume from the water volume fraction reconstructed from the deforming soil skeleton.

3.5. Multi-resolution strategy

In practical engineering simulations, the geometric scales of rock/structural components, particularly in their thickness direction, are often significantly smaller than the extensive domains of the soil and water phases. To ensure numerical accuracy, the SPH discretization typically requires a minimum of four particle layers across the thickness of a solid body. Imposing a uniform particle resolution governed by the finest scale of the structure would necessitate an excessively small particle spacing for the entire domain, resulting in an exorbitant number of particles in the soil and water phases, thereby imposing a prohibitive computational burden.

The previously established multi-resolution treatment for coupled SPH phases [42,43] is adopted here as an implementation component to reduce the particle count while maintaining sufficient resolution of thin rock and structural components. A high-resolution discretization is applied exclusively to the rock/structure phase to capture its geometric details, while a coarser resolution is employed for the soil and water phases. Consequently, the smoothing lengths associated with different phases are distinct, satisfying the relation $h^s = h^w > h^{rs}$.

For the computation of interaction forces between phases with disparate resolutions (*e.g.*, the interaction between soil and rock), a specific smoothing length selection criterion is required to ensure the symmetry of the particle neighbor search. Specifically, the larger of the two smoothing lengths is utilized for the kernel support domain. This ensures that if a soil particle falls within the search radius of a rock particle, the reciprocal condition holds true (*i.e.*, the rock particle is also identified as a neighbor of the soil particle). Given the condition $h^s > h^{rs}$, the smoothing length of the soil phase h^s is adopted for the soil–rock interaction.

Based on this discussion, the total contact force exerted by the rock/structure phase on a soil particle i (originally presented in Eq. (69)) is reformulated to explicitly incorporate the multi-resolution treatment:

$$\mathbf{F}_i^{s \leftarrow rs} = \sum_{j \in rs} \left\{ 2\tilde{\sigma}_i^s \cdot \mathbf{e}_{ij}^{s \leftarrow rs} + \beta^s \rho_{0i}^s c_{0i}^s \left[(\mathbf{v}_i^s - \mathbf{v}_j^{rs,d}) \cdot \mathbf{n}_j^{rs} \right] \mathbf{n}_j^{rs} \right\} \frac{\partial W^{s \leftarrow rs}(\mathbf{r}_{ij}, h^s)}{\partial r_{ij}} V_i^s V_j^{rs}, \tag{90}$$

where the kernel derivative $\partial W^{s \leftarrow rs}(\mathbf{r}_{ij}, h^s)/\partial r_{ij}$ is calculated using the smoothing length of the soil phase h^s, which is larger than that of the rock/structure phase. Similarly, the total contact force exerted by the soil particle i on the rock/structure phase (originally presented in Eq. (70)) can be obtained by replacing the kernel derivative with $\partial W^{s \leftarrow rs}(\mathbf{r}_{ij}, h^s)/\partial r_{ij}$.

The forces from rock/structure to water (Eqs. (73) and (74)) and from water to rock/structure (Eqs. (76) and (77)) are modified in a similar manner by employing the larger smoothing length h^w of the water phase for the kernel evaluations.

3.6. Time integration

To make the 3D calculations tractable, previously established dual-criteria time stepping and phase-decoupled subcycling strategies are incorporated into the present multiphysics framework [42–44].

For the water and soil phases, a dual-criteria time stepping scheme is adopted [44] to decouple the updates of particle configuration and physical state. This approach utilizes two distinct time steps: a larger advection time step (Δt_{ad}) and a smaller acoustic time step (Δt_{ac}). The particle configuration, including the computationally expensive neighbor search and connectivity updates, is performed only at the interval of Δt_{ad}. In contrast, the evolution of physical variables is integrated using the finer Δt_{ac}.

By reducing the frequency of neighbor list updates without compromising the acoustic wave propagation accuracy, this strategy significantly enhances the computational efficiency for both water and soil phases.

The time-step criteria for the advection and acoustic evolution are determined by:

$$\Delta t_{ad}^{s} = CFL_{ad}^{s}\frac{h^{s}}{|\mathbf{v}^{s}|_{\max}},\quad \Delta t_{ad}^{w} = CFL_{ad}^{w}\min\left(\frac{h^{w}}{|\mathbf{v}^{w}|_{\max}},\frac{\rho_0^{w}(h^{w})^2}{\eta^{w}}\right), \tag{91}$$

$$\Delta t_{ac}^{s} = CFL_{ac}^{s}\frac{h^{s}}{c_0^{s}+|\mathbf{v}^{s}|_{\max}},\quad \Delta t_{ac}^{w} = CFL_{ac}^{w}\frac{h^{w}}{c_0^{w}+|\mathbf{v}^{w}|_{\max}}, \tag{92}$$

The Courant–Friedrichs–Lewy (CFL) numbers are set to $CFL_{ad}^{s} = CFL_{ad}^{w} = 0.2$ and $CFL_{ac}^{s} = CFL_{ac}^{w} = 0.4$. To ensure the synchronized evolution and numerical stability of both phases, the unified operational time steps are determined as the minimum values between the two phases:

$$\Delta t_{ad} = \min\left(\Delta t_{ad}^{s},\Delta t_{ad}^{w}\right),\quad \Delta t_{ac} = \min\left(\Delta t_{ac}^{s},\Delta t_{ac}^{w}\right). \tag{93}$$

In addition, regarding the interaction between the soft phases (soil/water) and the stiff phases (rock/structure), the stability requirements for the latter typically dictate a time step significantly smaller than that required for the former, due to the high sound speed in solids ($c^{rs} > c^{s}\&c^{rs} > c^{w}$). Adopting a unified global time step constrained by the stiffest material would incur unnecessary computational costs for the soil and water phases. Therefore, a decoupled time stepping (or sub-cycling) strategy [42,43] is employed. The soil and water phases evolve with the larger time step Δt_{ac}, while the rock/structure phase is integrated using a suitably smaller time step Δt^{rs}:

$$\Delta t^{rs} = CFL^{rs}\min\left(\frac{h^{rs}}{c_0^{rs}+|\mathbf{v}^{rs}|_{\max}},\sqrt{\frac{h^{rs}}{|\mathrm{d}\mathbf{v}^{rs}/\mathrm{d}t|_{\max}}}\right), \tag{94}$$

where $CFL^{rs} = 0.6$. Consequently, within a single update cycle of the soil or water phase, the rock/structure phase is updated $\kappa = \lceil \Delta t_{ac}/\Delta t^{rs}\rceil$ times, where $\lceil\cdot\rceil$ denotes the ceiling operation which maps the value to the least integer greater than or equal to the argument.

The implementation of distinct time integration steps for the fluid and solid governing equations can give rise to force mismatches at the fluid–structure interface. Specifically, during the calculation of imaginary pressure $p^{rs,d}$ (Eqs. (73) and (76)) and velocity $\mathbf{v}^{rs,d}$ (Eqs. (69), (70), (74) and (77)), the velocity and acceleration of solid particles may undergo multiple updates within a single fluid time step due to the smaller Δt^{rs}. This discrepancy can lead to inconsistencies and potentially violate momentum conservation in the coupled system. To resolve this force-calculation mismatch, we redefine the imaginary pressure $p_i^{rs,d}$ and velocity $\mathbf{v}_i^{rs,d}$ as follows:

$$\begin{cases} p_i^{rs,d} = p_j^{\Psi} + \rho_j^{\Psi}\max\left[0,\left(\mathbf{g}-\widetilde{\frac{\mathrm{d}\mathbf{v}_i^{rs}}{\mathrm{d}t}}\right)\cdot\mathbf{n}_i^{rs}\left(\mathbf{r}_{ij}^{rs\leftarrow\Psi}\cdot\mathbf{n}_i^{rs}\right)\right] \\ \mathbf{v}_i^{rs,d} = 2\widetilde{\mathbf{v}_i^{rs}} - \mathbf{v}_j^{\Psi} \end{cases}, \tag{95}$$

where $\Psi \in \{s,w\}$ denotes the soil or water phase. The terms $\widetilde{\frac{\mathrm{d}\mathbf{v}_i^{rs}}{\mathrm{d}t}}$ and $\widetilde{\mathbf{v}_i^{rs}}$ represent the average acceleration and velocity of a rock/structure particle i over the κ sub-steps in acoustic time step Δt_{ac}. These time-averaged quantities are substituted into Eqs. (70), (76), and (77) to determine the dummy states $p_i^{rs,d}$ and $\mathbf{v}_i^{rs,d}$. Analogously, for the reciprocal interaction where a soil/water particle $i \in \Psi$ interacts with a rock/structure neighbor j, the corresponding dummy variables $p_j^{rs,d}$ and $\mathbf{v}_j^{rs,d}$ are obtained using the identical formulation by simply applying the index j.

The integration follows a position-based Verlet scheme. For the soil/water phases (where $\Psi \in \{s,w\}$ denotes the soil or water phase), the primary scalar variable χ (representing the volume fraction n^{s} for soil or density ρ^{w} for water) and the particle position are first updated to the mid-point $(n+\frac{1}{2})$:

$$\begin{cases} \chi_i^{\Psi,n+\frac{1}{2}} = \chi_i^{\Psi,n} + \frac{1}{2}\Delta t_{ac}\dot{\chi}_i^{\Psi,n} \\ \mathbf{r}_i^{\Psi,n+\frac{1}{2}} = \mathbf{r}_i^{\Psi,n} + \frac{1}{2}\Delta t_{ac}\mathbf{v}_i^{\Psi,n} \end{cases}, \tag{96}$$

where $\dot{\chi} = \mathrm{d}\chi/\mathrm{d}t$ represents the rate of change of χ. Subsequently, the particle velocity is updated to the new time step $(n+1)$ using the forces computed based on the mid-point configuration:

$$\mathbf{v}_i^{\Psi,n+1} = \mathbf{v}_i^{\Psi,n} + \Delta t_{ac}\frac{\mathrm{d}\mathbf{v}_i^{\Psi}}{\mathrm{d}t}. \tag{97}$$

Finally, the position and scalar variables are updated to the end of the step:

$$\begin{cases} \mathbf{r}_i^{\Psi,n+1} = \mathbf{r}_i^{\Psi,n+\frac{1}{2}} + \frac{1}{2}\Delta t_{ac}\mathbf{v}_i^{\Psi,n+1} \\ \chi_i^{\Psi,n+1} = \chi_i^{\Psi,n+\frac{1}{2}} + \frac{1}{2}\Delta t_{ac}\dot{\chi}_i^{\Psi,n+1} \end{cases}. \tag{98}$$

During this interval Δt_{ac}, the rock/structure phase (rs) undergoes κ sub-steps. Let index $\varkappa = 0, \dots, \kappa-1$ denote the sub-step index. The deformation tensor, density, and particle position are first updated to the midpoint ($\varkappa + \frac{1}{2}$) as:

$$\begin{cases} \mathbb{F}_i^{rs,\varkappa+\frac{1}{2}} = \mathbb{F}_i^{rs,\varkappa} + \frac{1}{2}\Delta t^{rs}\dot{\mathbb{F}}_i^{rs,\varkappa} \\ \rho_i^{rs,\varkappa+\frac{1}{2}} = \rho_{0i}^{rs}\frac{1}{J_i} \\ \mathbf{r}_i^{rs,\varkappa+\frac{1}{2}} = \mathbf{r}_i^{rs,\varkappa} + \frac{1}{2}\Delta t^{rs}\mathbf{v}_i{}^{rs,\varkappa} \end{cases}, \tag{99}$$

The velocity is then updated:

$$\mathbf{v}_i^{rs,\varkappa+1} = \mathbf{v}_i^{rs,\varkappa} + \Delta t^{rs}\frac{\mathrm{d}\mathbf{v}_i^{rs}}{\mathrm{d}t}. \tag{100}$$

And the final configuration for the sub-step is obtained by:

$$\begin{cases} \mathbb{F}_i^{rs,\varkappa+1} = \mathbb{F}_i^{rs,\varkappa+\frac{1}{2}} + \frac{1}{2}\Delta t^{rs}\dot{\mathbb{F}}_i^{rs,\varkappa+1} \\ \rho_i^{rs,\varkappa+1} = \rho_{0i}^{rs}\frac{1}{J_i} \\ \mathbf{r}_i^{rs,\varkappa+1} = \mathbf{r}_i^{rs,\varkappa+\frac{1}{2}} + \frac{1}{2}\Delta t^{rs}\mathbf{v}_i{}^{rs,\varkappa+1} \end{cases}. \tag{101}$$

This loop is repeated κ times until the rock/structure phase is synchronized with the soil/water phases at $t + \Delta t_{ac}$.

The detailed implementation of the time integration scheme is summarized in Algorithm 2.

Algorithm 2: Time integration scheme for porosity-consistent soil–water–rock–structure interaction.

Input: Initial geometries, material parameters, and simulation end time T_{end}
Generate the initial soil, water, and rock/structure particle sets;
if *the soil and water phases overlap initially* **then**
  Perform the level-set-guided porosity-consistent relaxation of equal-mass water particles;
end
Initialize the physical states of all phases;
Set $\rho_i^w = \rho_0^w$, reconstruct n_i^w, and compute $\tilde{\rho}_i^w = n_i^w \rho_i^w$ and $V_i^w = m_i^w / \tilde{\rho}_i^w$;
Perform the initial neighbor search and compute kernel gradients;
Compute the initial rock/structure normal directions and corrected reference configurations;
while $t < T_{\text{end}}$ **do**
  Determine $\Delta t_{ad} = \min(\Delta t_{ad}^s, \Delta t_{ad}^w, T_{\text{end}} - t)$;
  Reinitialize the required density and volume-fraction fields;
  Update the rock/structure normal directions;
  Set $\tau_{ac} = 0$;
  while $\tau_{ac} < \Delta t_{ad}$ **do**
    Determine $\Delta t_{ac} = \min(\Delta t_{ac}^s, \Delta t_{ac}^w, \Delta t_{ad} - \tau_{ac})$;
    Update the soil and water phases using the position-based Verlet scheme;
    Reconstruct n_i^w and update $\tilde{\rho}_i^w = n_i^w \rho_i^w$ and $V_i^w = m_i^w / \tilde{\rho}_i^w$;
    Compute the interaction forces between the rock/structure and soil/water phases;
    Set $\tau_{rs} = 0$;
    while $\tau_{rs} < \Delta t_{ac}$ **do**
      Determine $\Delta t^{rs} = \min(\Delta t_{\text{crit}}^{rs}, \Delta t_{ac} - \tau_{rs})$;
      Integrate the rock/structure phase using the position-based Verlet scheme;
      Set $\tau_{rs} \leftarrow \tau_{rs} + \Delta t^{rs}$;
    end
    Compute the time-averaged rock/structure velocity and acceleration;
    Set $t \leftarrow t + \Delta t_{ac}$ and $\tau_{ac} \leftarrow \tau_{ac} + \Delta t_{ac}$;
  end
  Update the neighbor lists, kernel gradients, and interphase particle configurations;
end
Output the simulation results.

4. Validation of two-phase coupling mechanisms

In this section, a series of benchmark tests are conducted to systematically evaluate the accuracy, stability, and predictive capability of the proposed multiphase SPH framework. By comparing the present numerical results with established experimental measurements and previous numerical solutions, the effectiveness of the pairwise phase coupling mechanisms is rigorously validated.

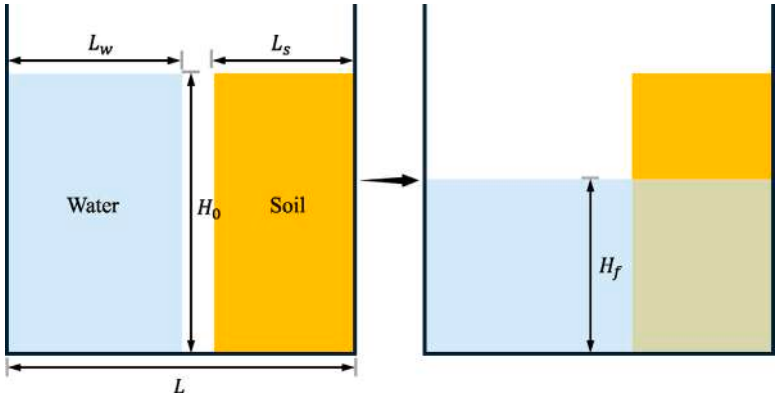

Fig. 4. Volume conservation of the fluid phase: schematic diagram of the collapse-into-porous-media benchmark.

The linear viscous drag formulation in Eq. (29) is exclusively applied to the low-velocity U-tube seepage flow (Section 4.2). For all other highly dynamic test cases, the non-linear viscous drag term in Eq. (31) is activated to accurately capture the significant inertial resistance induced by large relative phase velocities.

The Wendland C^2 kernel [72] is uniformly employed for the SPH interpolation, which is defined as:

$$W(q,h) = C_d \begin{cases} (1-0.5q)^4(2q+1) & 0 \le q \le 2 \\ 0 & q > 2 \end{cases}, \tag{102}$$

where $q = |\mathbf{r}_{ij}|/h$ represents the normalized distance between interacting particles, and h is the smoothing length. The normalization coefficient C_d takes the values of $3/(4h)$, $7/(4\pi h^2)$, and $21/(16\pi h^3)$ for one-, two-, and three-dimensional domains, respectively. The smoothing lengths are set as $h^s = 1.3dp^s$ for the soil phase, $h^w = 1.8dp^w$ for the water phase, and $h^{rs} = 1.15dp^{rs}$ for the rock/structure phase. Here, dp^s, dp^w, and dp^{rs} denote the initial particle spacings of the soil, water, and rock/structure phases, respectively. For the water phase, dp^w refers to the reference particle spacing in the pure-water region, whereas the porosity-dependent spacing of water particles in the soil–water mixture region is denoted by $dp_i^{w\in m}$.

4.1. Volume conservation of the fluid phase

To verify the porosity-consistent representation of the water phase, a simple collapse-into-porous-media test is first considered. This benchmark is designed to examine whether the water-particle volume is consistently updated when water particles move from a pure-water region into a porous soil region. Although the present framework is intended for fully coupled soil–water–rock–structure interaction problems with deformable soil, the soil skeleton is fixed in this test so that the fluid-volume conservation property can be isolated from soil deformation and solid contact effects.

The configuration follows the volume-conservation benchmark of Zhu et al. [36]. As shown in Fig. 4, a rectangular tank of length L is partially filled with an initially quiescent water column on the left and a dry porous soil region on the right. The initial length and height of the water column are denoted by L_w and H_0, respectively, and the length of the fixed porous soil region is denoted by L_s. The soil skeleton is assumed to be undeformable and has a prescribed constant soil volume fraction n^s, so that the water volume fraction in the porous region is $n^w = 1 - n^s$. In this benchmark, the parameters are selected as:

$$L = 1.0\ \text{m}, \quad L_w = 0.5\ \text{m}, \quad L_s = 0.4\ \text{m}, \quad H_0 = 0.8\ \text{m}, \quad n^s = 0.5, \quad D_{50} = 0.016\ \text{m}.$$

In the proposed porosity-consistent formulation, the water-particle volume is evaluated from the apparent water density as:

$$V_i^w = \frac{m_i^w}{\tilde{\rho}_i^w} = \frac{m_i^w}{n_i^w \rho_i^w}. \tag{103}$$

Therefore, when a water particle moves from the pure-water region ($n^w = 1$) into the porous region ($n^w < 1$), its representative SPH volume increases accordingly. For an equal-mass water-particle representation, the corresponding target spacing is

$$dp_i^{w\in m} = dp^w \left(n_i^w\right)^{-1/d}, \tag{104}$$

where $dp_i^{w\in m}$ is the water-particle spacing in the soil–water mixture region and d is the spatial dimension.

At the final static state, the water should occupy both the pure-water region and the pore space of the porous soil region. By conserving the total physical volume of water, the analytical final water depth can be obtained as

$$H_f = \frac{H_0 L_w}{L - L_s n^s}. \tag{105}$$

This expression is independent of the tank width because the same width appears in both the initial and final water volumes.

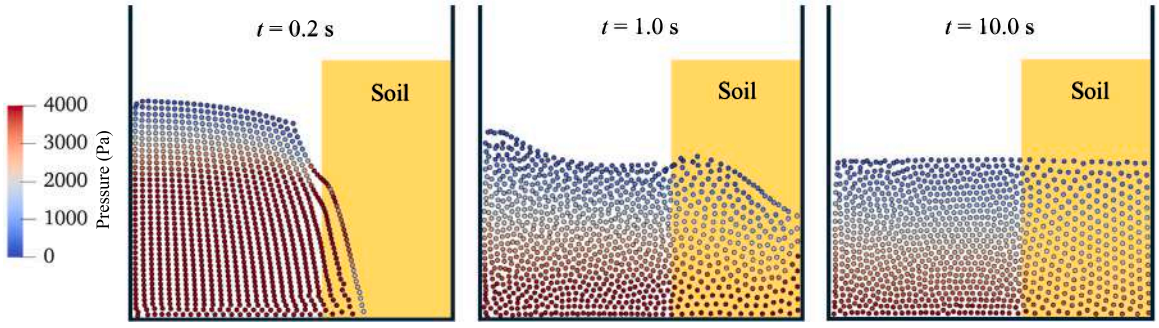

Fig. 5. Volume conservation of the fluid phase: pressure evolution in the collapse-into-porous-media test. Increased particle spacing inside the fixed soil skeleton reflects a porosity-consistent increase in the representative particle volume. $dp^w = 0.02$ m.

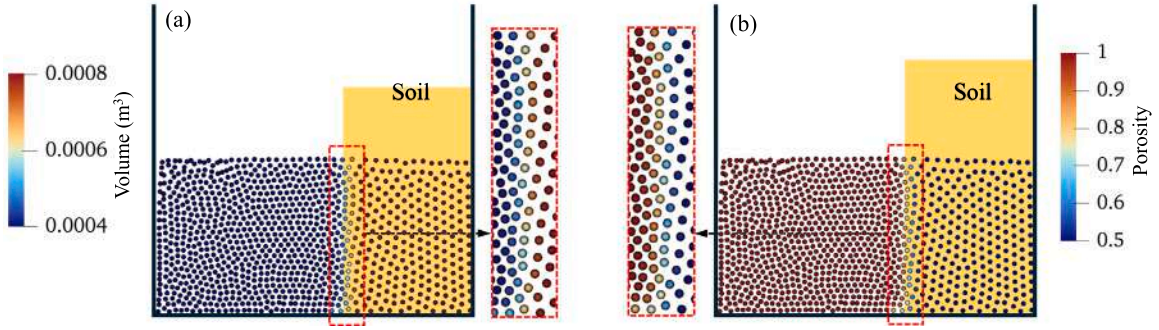

Fig. 6. Volume conservation of the fluid phase: final water-particle volume and porosity distributions. The water-particle volume approximately doubles as the porosity decreases from $n^w = 1$ to $n^w = 0.5$, with a continuous transition across the interface. $dp^w = 0.02$ m.

A 2D simulation is performed in this section to provide a direct visualization of the porosity-induced variation of water-particle volume and spacing. Fig. 5 shows the pressure field at $t = 0.2$ s, 1.0 s and 10.0 s. At the early stage, the water column collapses under gravity and the water front approaches the fixed porous soil skeleton. As water enters the porous region, the local water volume fraction decreases from $n^w = 1$ in the pure-water region to $n^w = 0.5$ inside the soil skeleton. According to Eq. (103), the representative volume of each equal-mass water particle therefore increases, which is reflected by the visibly enlarged particle spacing in the porous region. At $t = 10.0$ s, the system reaches a nearly static state with an approximately horizontal free surface, and the pressure field remains smooth across the pure-water/porous-medium interface.

The local consistency between water-particle volume and porosity at the final static state is further examined in Fig. 6. Here, the porosity shown in Fig. 6(b) corresponds to the water-accessible volume fraction. Since the water particles have equal mass and the intrinsic water density remains nearly constant, Eq. (103) gives the approximate relation $V_i^w \propto \frac{1}{n_i^w}$. Therefore, the water-particle volume inside the porous region should be approximately twice that in the pure-water region. This expected behavior is clearly observed in Fig. 6(a), where the representative particle volume increases from about 4.0×10^{-4} m^3 in the pure-water region to about 8.0×10^{-4} m^3 in the porous region. The magnified views near the interface further show that both the particle volume and porosity vary continuously across the transition region, avoiding an abrupt jump in the water-particle representation.

To further quantify the global volume conservation, simulations are conducted with the prescribed soil volume fraction $n^s = 0.5$ and three initial water-particle spacings, $dp^w = 0.04$, 0.02 and 0.01 m. For each case, the final water depth obtained from the SPH simulation is compared with the analytical solution in Eq. (105). The numerical final water depth is measured from the free-surface elevation at the horizontal center of the water domain.

For direct comparison, the same simulations are also performed using the formulation of Bui et al. [18]. In that formulation, the representative volume of a water particle does not vary with the local water volume fraction when the particle enters the porous region.

As shown in Fig. 7(a), the present formulation increases the representative water-particle volume inside the porous region according to the local water volume fraction, and the resulting equilibrium water level remains close to the theoretical value. In contrast, the water-particle volume in the formulation of Bui et al. [18] remains approximately unchanged after the particles enter the porous region, as shown in Fig. 7(b). The resulting water level is substantially lower than the theoretical value, indicating a loss of global physical water volume.

As shown in Table 1, for the present formulation, the predicted final water depth measured at the horizontal center of the water domain converges to the analytical value as the initial water-particle spacing is refined. The small non-monotonic variation between

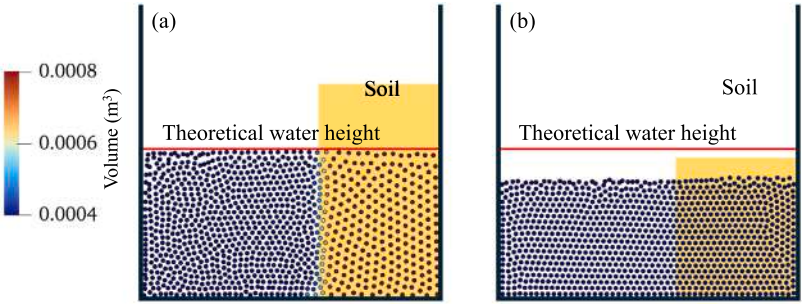

Fig. 7. Volume conservation of the fluid phase: comparison of the final water-particle distributions obtained using (a) the present porosity-consistent formulation and (b) the formulation of Bui et al. [18]. The red horizontal line denotes the theoretical equilibrium water level. $n^s = 0.5$ and $dp^w = 0.02$ m. (For interpretation of the references to color in this figure legend, the reader is referred to the web version of this article.)

Table 1
Volume conservation of the fluid phase: comparison of the final water depths obtained with different initial water-particle spacings.

Method	Soil fraction	Theory	SPH final water depth H_f^{SPH} (m)		
	n^s	H_f^{theory} (m)	$dp^w = 0.04$ m	$dp^w = 0.02$ m	$dp^w = 0.01$ m
Present study	0.5	0.500	0.518	0.493	0.504
Bui et al. [18]	0.5	0.500	0.396	0.394	0.397

the intermediate and finest resolutions is mainly attributed to residual free-surface fluctuation and the practical measurement of the equilibrium water level from discrete particles. At the finest resolution, $dp^w = 0.01$ m, the final water depth is 0.504 m, corresponding to a relative error of only 0.8%. In contrast, the formulation of Bui et al. [18] gives final water depths of 0.396, 0.394 and 0.397 m at the three resolutions, respectively. These values remain approximately 20.6%–21.2% below the theoretical solution.

This agreement confirms that the porosity-consistent water-particle volume preserves the global physical volume of the fluid phase in the collapse-into-porous-media test. Here, fluid-volume conservation should be understood within the accuracy of the weakly compressible SPH approximation. The mass of each water particle, and hence the total water mass, is conserved exactly. In contrast, the total physical water volume may vary slightly because the intrinsic water density ρ_i^w evolves through the equation of state in Eq. (26). Since the artificial speed of sound is selected to maintain density fluctuations below approximately 1%, the corresponding physical-volume variation is of the same order for these small density changes. Therefore, the present benchmark demonstrates that the porosity-consistent formulation avoids systematic fluid-volume errors associated with changes in the local water volume fraction, rather than implying exact incompressible-volume conservation.

4.2. U-tube flow

To rigorously validate the fluid–porous media interaction module within the proposed unified framework, the classical U-tube seepage test is examined first. Although the overarching goal of this study is to model fully coupled soil–water–rock–structure interactions where the soil is deformable, this benchmark isolates the seepage mechanism by enforcing a stationary solid skeleton. This critical simplification allows the full coupled SPH system to degenerate to a fixed porous medium problem, providing a fundamental verification of the fluid-phase governing equations and the inter-phase momentum exchange (drag force) algorithms.

Both 2D and 3D U-tube tests are considered in this benchmark. The 2D test is used to visualize the porosity-consistent water-particle relaxation and the associated particle-volume variation in the porous region, while the 3D test is used for quantitative validation of the hydraulic-head decay and spatial convergence. The 3D problem configuration consists of a U-shaped container with a square cross-section (1.0×1.0 m) and a thickness of $W = 1.0$ m. A porous soil specimen of length $L = 1.0$ m is located at the bottom center, separating two water columns. The simulation is initialized with a hydraulic head difference $\Delta H_0 = 1.0$ m between the left and right reservoirs. The fluid density is set to $\rho_0^w = 1000$ kg/m^3, and the water volume fraction, equivalent to the porosity of the soil specimen, is prescribed as $n^w = 0.4$. The geometric setup is illustrated in Fig. 8.

In this benchmark, the flow regime is assumed to be laminar and governed by Darcy's law. Consequently, the interaction force between the fluid and the fixed solid skeleton is dominated by the linear drag term, while turbulent resistance is negligible. Under these assumptions, the temporal evolution of the hydraulic head difference $\Delta H(t)$ follows an exponential decay:

$$\Delta H(t) = \Delta H_0 \exp\left(-\frac{2}{L} K^s t\right), \tag{106}$$

where K^s represents the hydraulic conductivity. The ability of the numerical model to reproduce this permeability-dependent head decay is a primary indicator of the accuracy of the inter-phase drag coupling.

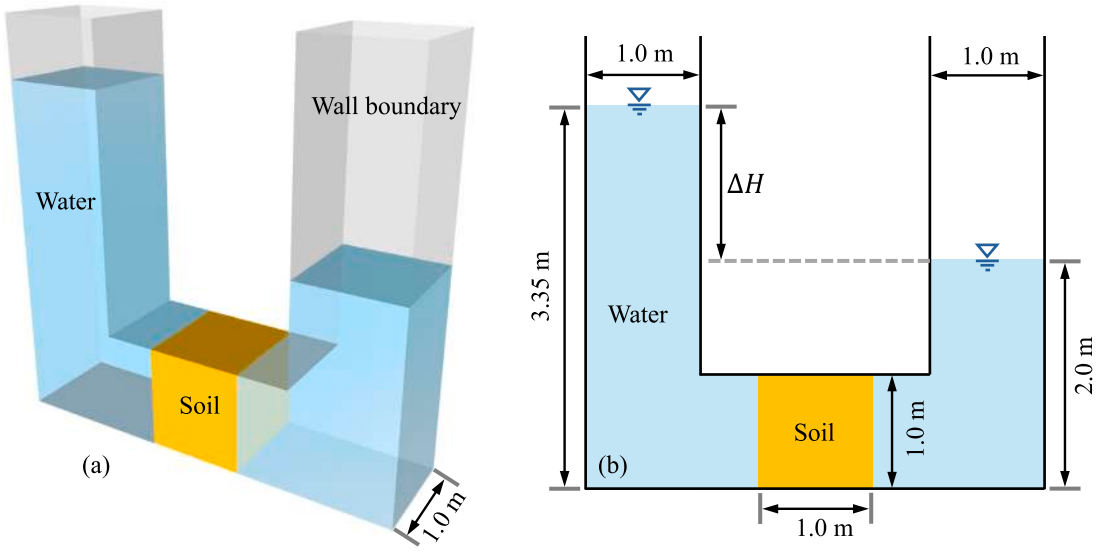

Fig. 8. U-tube flow: schematic diagram of the numerical model setup, including the (a) 3D configuration used for quantitative seepage validation and (b) 2D configuration used for visualizing porosity-consistent water-particle relaxation.

Before the physical seepage simulation, the water particles in the porous region are generated by the proposed level-set-guided porosity-consistent particle relaxation. Fig. 9 shows the relaxation process for both the 2D and 3D U-tube configurations. At relaxation step 0, the water particles in the porous soil region are randomly generated according to the prescribed pore-fluid volume. As the relaxation proceeds, the initially disordered particles gradually evolve into a regular porosity-consistent distribution. After 100 relaxation steps, a stable initial water-particle configuration is obtained in both 2D and 3D. The color distribution confirms that the water-particle number density and representative volume inside the porous specimen are consistent with the prescribed porosity field, while the transition between the pure-water reservoirs and the porous region remains smooth.

For the representative 3D pressure-field and permeability-comparison simulations, the water phase is discretized using a reference particle spacing $dp^w = 0.05$ m, while different spacings are used in the spatial convergence study. The corrected Shepard density filter [36] is employed here to restore C^1 particle consistency near the free surfaces. The evolution of the water pressure field is analyzed to verify the hydrostatic consistency and the interface stability of the unified framework. Fig. 10 illustrates the pressure fields on the longitudinal mid-plane at various time instants. Following the pressure-initialization strategy adopted by Zhu et al. [36], the water pressure field at $t = 0$ is configured to ensure hydraulic consistency across the domain. Specifically, fluid particles in the upstream and downstream reservoirs are initialized with uniform hydraulic heads corresponding to their respective initial water levels. To prevent numerical discontinuities at the start of the simulation, particles within the porous soil region are assigned a linearly decreasing hydraulic head connecting the high-head inlet to the low-head outlet. Consequently, a smooth yet significant pressure gradient is established across the porous soil section, acting as the accurate driving force for the seepage flow. As the simulation progresses and the water levels gradually equalize, this pressure gradient diminishes monotonically, eventually converging to a uniform hydrostatic distribution corresponding to the equilibrium state.

Subsequently, the spatial convergence of the proposed method is examined, as shown in Fig. 11. Fig. 11a presents the temporal evolution of the hydraulic head difference for a representative hydraulic conductivity of $K^s = 0.05$ m/s under varying particle resolutions. It can be clearly observed that as the resolution increases (*i.e.*, the particle spacing dp^w decreases), the SPH results progressively approach the theoretical solution. To further quantify the accuracy, Fig. 11b plots the relative L_2 norm error of the numerical results against the particle resolution. The error analysis reveals a convergence rate of approximately 1.2, demonstrating the consistent numerical behavior of the proposed unified framework.

To rigorously evaluate the robustness of the solver across varying permeabilities, four distinct hydraulic conductivity values ($K^s = 0.001, 0.005, 0.01, 0.05$ m/s) are examined. A comparison between the numerical results and the analytical solutions is presented in Fig. 12. The temporal evolution of the hydraulic head difference ΔH predicted by the proposed SPH framework exhibits good agreement with the theoretical solutions given by Eq. (106) for all considered K^s values. The results correctly capture the permeability-dependent exponential decay of the hydraulic head difference as the system approaches equilibrium. This quantitative consistency confirms that the linear Darcy resistance is accurately integrated into the three-dimensional momentum equation and validates the solver's capability in handling inter-phase momentum transfer within the fixed porous skeleton.

For the present U-tube configuration, the formulations of Bui et al. [18] and Zhu et al. [36] can also reproduce the theoretical evolution of the hydraulic-head difference. In the formulation of Bui et al. [18], the representative fluid-particle volume is not adjusted according to the local water volume fraction. Because the porous specimen is initially saturated, the omitted volume increase of clear-water particles entering the porous region is largely offset by the omitted volume decrease of particles initially

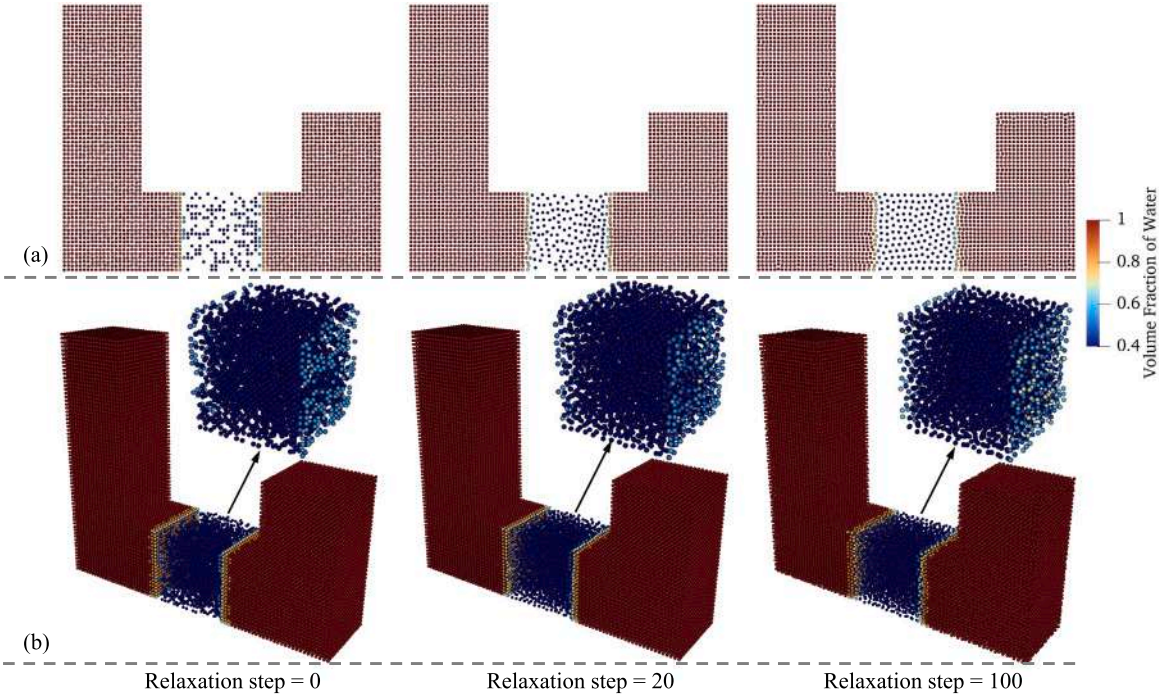

Fig. 9. U-tube flow: level-set-guided porosity-consistent particle relaxation for the initial water-particle distribution. (a) 2D U-tube configuration; (b) 3D U-tube configuration. (For interpretation of the references to color in this figure legend, the reader is referred to the web version of this article.)

inside the porous region as they leave it. Consequently, the associated volume errors have only a limited influence on the global response in this particular U-tube test. Such cancellation does not occur in the initially non-overlapping configuration considered in Section 4.1, where water enters an initially dry porous region without a compensating outflow of pore water, resulting in substantial fluid-volume loss with the formulation of Bui et al. [18]. In contrast, Zhu et al. [36] assign the same initial geometric volume but porosity-dependent masses to the water particles; particles initialized inside the porous region therefore have smaller masses. When these particles subsequently enter the clear-water region, their representative volumes decrease and they coexist with the originally larger-mass clear-water particles, producing heterogeneous particle volumes and a locally nonuniform distribution, as visible in Fig. 11 of Zhu et al. [36] Nevertheless, their particle masses and representative volumes remain mutually consistent. The present equal-mass initialization avoids this variable-mass particle mixture by representing porosity through the initial water-particle number density, spacing, and representative volume.

4.3. Submerged granular landslide-generated waves

To further evaluate the performance of the proposed multiphase SPH framework in capturing complex water–soil interactions, the bench-scale experiment of a submerged granular landslide [73] is investigated. This benchmark involves the rapid collapse of a submerged triangular sand mass and the subsequent generation of impulsive waves. As illustrated in Fig. 13, the computational domain consists of a water tank equipped with a rigid inclined slope. A granular column with an initial height of 0.65 m is positioned on the slope, fully submerged under 1.6 m of water.

The granular mass is initialized as a fully saturated soil–water mixture. With an initial solid volume fraction of $n_0^s = 0.62$, the corresponding water volume fraction is $n_0^w = 0.38$. The soil skeleton and pore water are represented by two spatially overlapping particle sets, and the equal-mass water particles inside the granular mass are initialized using the porosity-consistent relaxation procedure described in Section 3.3. During the collapse, water particles move independently from the soil skeleton and may enter or leave the deforming granular domain. The local porosity and representative water-particle volume are updated from the evolving soil configuration. The physical parameters are selected according to previous experimental [73] and numerical studies [36]. The soil intrinsic density is 2550 kg/m^3 with an initial volume fraction of 0.62. Its mechanical behavior is governed by an elastoplastic model with a Young's modulus of 1.5 MPa and a Poisson's ratio of 0.3. The yield criterion is defined by an internal friction angle of 35° with zero cohesion and dilation. A characteristic length $D_c = 4.5$ mm is adopted for the soil grains. For the fluid phase, the water is modeled with an intrinsic density of 1000 kg/m^3 and a dynamic viscosity of 0.001 Pa s. In the numerical discretization, an initial particle spacing $dp^w = dp^s = 0.01$ m is employed for the multiphase fields.

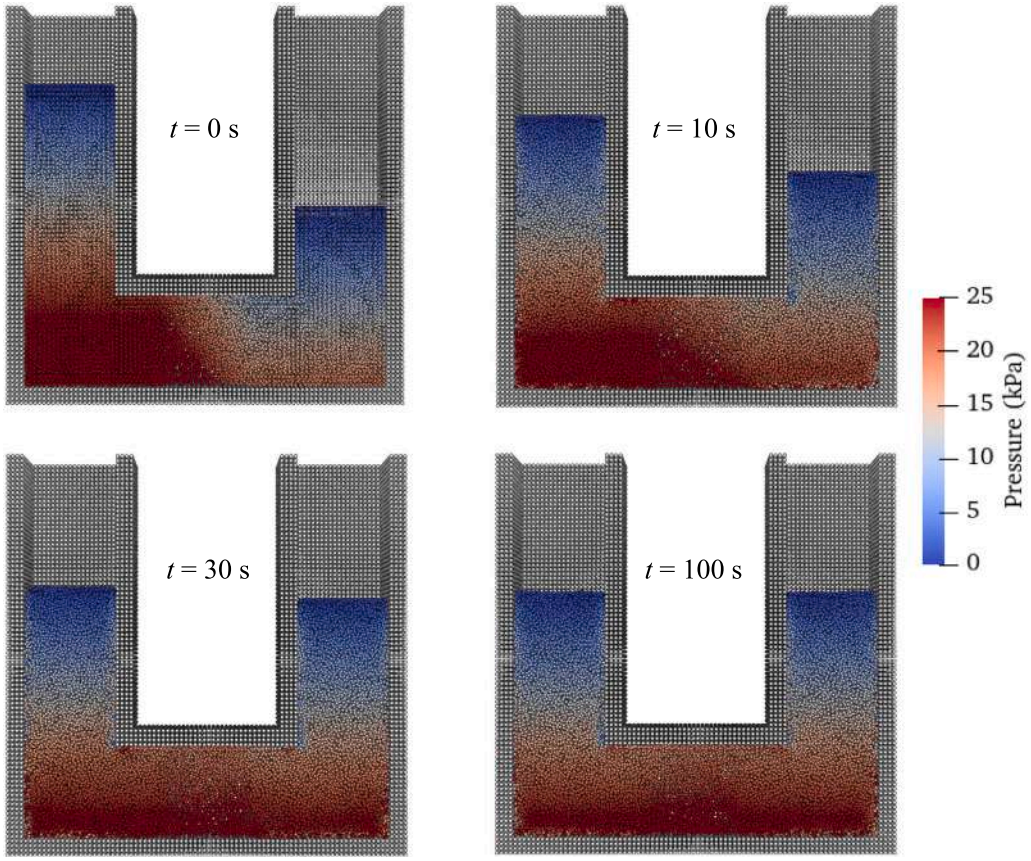

Fig. 10. U-tube flow: evolution of the water pressure field on the longitudinal mid-plane at different time instants. $dp^w = 0.05$ m and $K^s = 0.05$ m/s.

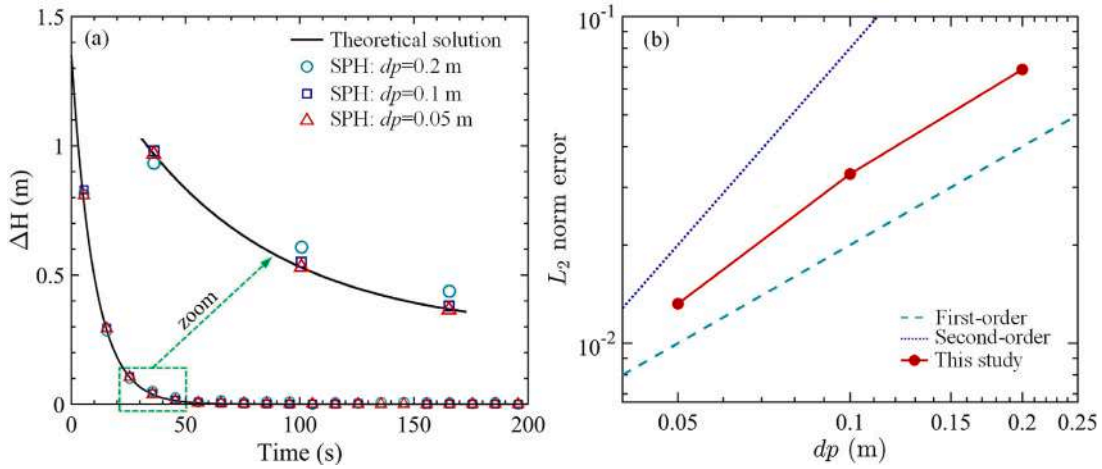

Fig. 11. U-tube flow: spatial convergence analysis for $K^s = 0.05$ m/s: (a) time histories of the hydraulic head difference ΔH obtained with different initial water-particle spacings dp^w; (b) the L_2 error norm relative to the theoretical solution, showing the convergence order.

Fig. 14 presents the snapshots of the spatiotemporal evolution of the system, illustrating the water pressure field and sediment velocity distribution. At the incipient stage of the collapse, the granular mass initiates a downward sliding motion while substantially maintaining its initial triangular configuration. Correspondingly, the free water surface exhibits a noticeable elevation at the slide front and a concurrent subsidence above the sliding body, forming a characteristic concave profile. As the landslide accelerates, the morphological features of the sediment body undergo significant changes: the tail of the slide gradually elongates and sharpens,

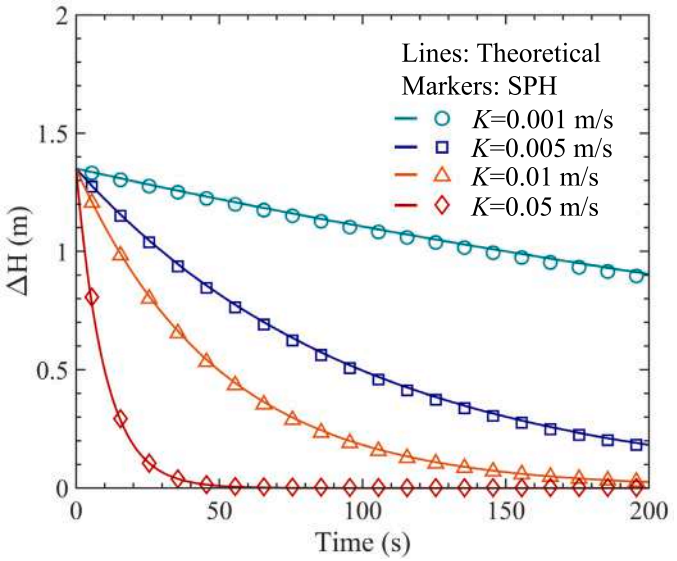

Fig. 12. U-tube flow: temporal evolution of the hydraulic head difference ΔH for different hydraulic conductivities. Lines denote analytical solutions and markers denote SPH results.

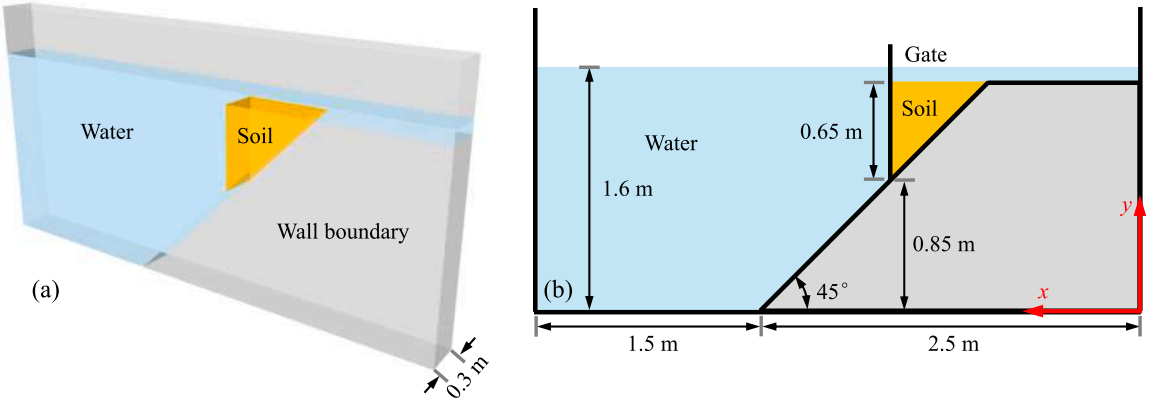

Fig. 13. Submerged granular landslide: (a) 3D isometric view illustrating the spatial configuration, and (b) cross-sectional view specifying the geometric dimensions.

whereas the front becomes relatively blunt and thickened due to the intense hydrodynamic resistance encountered during its propagation. These dynamic features, including the strong fluctuations of the water surface, are consistent with experimental observations.

The intricate water–sediment interaction and the internal exchange of phases are further detailed in Fig. 15. To track the phase migration, water particles are categorized into two groups based on their initial locations: the pure water initially outside the sediment domain (represented in blue) and the water initially contained within the mixture phase (represented in red), while the current position of the sediment phase is denoted in black. At the early stage of the sliding, the red pore water moves synchronously with the black soil skeleton, collectively triggering the initial downward movement of the free surface and the resulting impulse wave. However, as the sliding progresses, a "squeezing-out" effect becomes prominent at the rear of the landslide. Specifically, the blue ambient water penetrates the granular mass from the leading edge due to the high-pressure gradient at the front. Consequently, the original red pore water lags behind the fast-moving soil skeleton and is eventually expelled from the tail. The current SPH result is consistent with the numerical simulation by Zhu et al. [36], who also reported a similar phase-separation behavior during the submerged landslide process. This phenomenon indicates a significant phase separation and mass exchange. Simultaneously, a prominent vortex is observed to develop at the upper-left boundary of the sediment, driven by the shear-induced momentum exchange between the ambient blue water and the moving black sediment, further illustrating the complex multiphase coupling characteristic of submarine landslides.

Quantitative validations of the sediment morphology and the landslide-induced waves are provided in Figs. 16 and 17, respectively. As shown in Fig. 16, the simulated soil profiles at $t = 0.4$ s and $t = 0.8$ s demonstrate a satisfactory agreement with

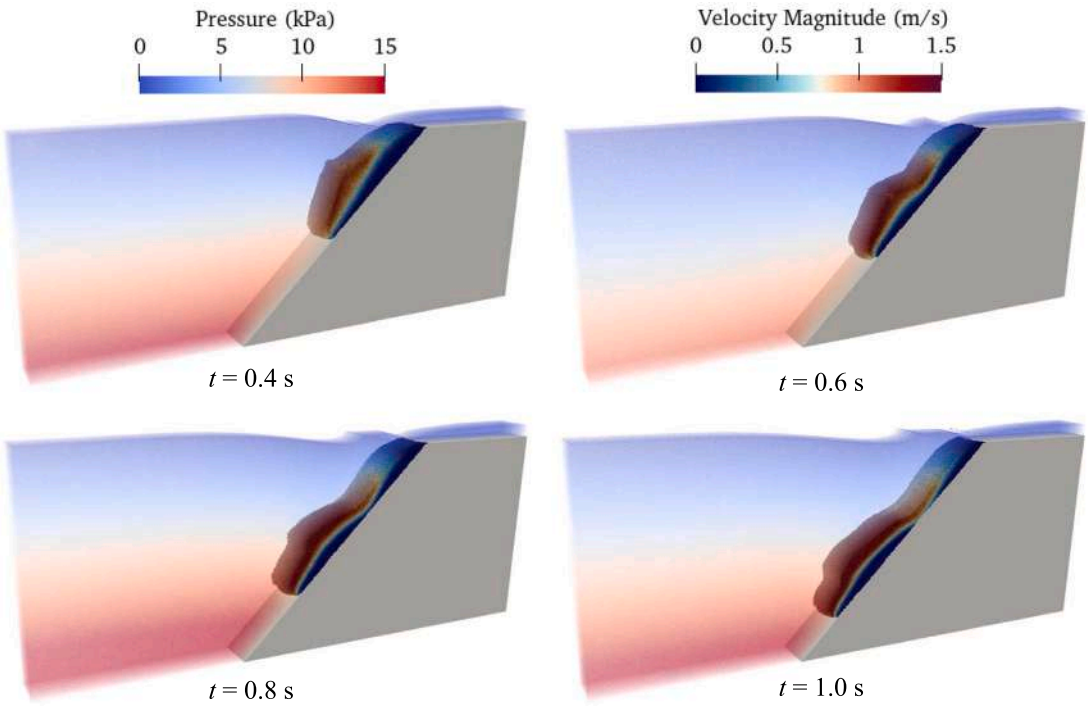

Fig. 14. Submerged granular landslide: snapshots showing the water pressure field and sediment velocity field at typical time instants.

the experimental data [73] and previous numerical benchmarks [36,74,75]. It is worth noting, however, that the experimental sediment profile appears slightly more expansive than our numerical predictions. The observed deviations between the present SPH predictions and experimental data are consistent with findings reported in prior numerical studies [36,74,76], underscoring a persistent challenge within current modeling frameworks. Such discrepancies are primarily governed by the "pump-out" of fine particles and the subsequent diffusive transport at the water–soil interface [36]. Since these interfacial mixing mechanisms transcend the predictive capabilities of conventional geomechanical constitutive laws, more sophisticated multi-scale or multiphase models are essential to fully characterize the late-stage morphological expansion of the sliding mass.

Finally, Fig. 17 compares the predicted landslide-generated waves with existing data. The proposed SPH model accurately captures the wave amplitude and the propagation of the leading wave, confirming that the current SPH framework is robust in handling the multi-physics coupling between the soil and water. The agreement with the results of Zhu et al. [36] further shows that the volume-compatible water formulation can be coupled with the deformable soil skeleton without degrading the predicted macroscopic wave response.

4.4. Low-speed impact craters

While the preceding cases primarily validated the soil–water coupling, this section focuses on the 3D interaction between the granular soil phase and the rock/structure phase. The formation of impact craters by dropping a sphere into a granular bed serves as a rigorous benchmark for assessing the coupling between the ULSPH-based granular solver and the TLSPH-based elastic solid solver. Following the foundational experiments by Uehara et al. [77] and Ambroso et al. [78], their results have been employed by subsequent studies [43,79] to validate numerical models.

The schematic configuration is presented in Fig. 18. An elastic ball of radius R is released from a height H and impacts a dry, non-cohesive granular medium. In this multiphase framework, the ball is modeled as a deformable solid using the TLSPH method, while the granular bed is represented using the ULSPH formulation. The penetration depth D is the primary metric for validation, which is compared against the following empirical relationship derived from experimental measurements [77,78]:

$$D_{ball} = \frac{0.14}{\mu}\left(\frac{\rho_{ball}}{\rho_{granular}}\right)^{1/2}\left(2R_{ball}\right)^{2/3}\left(H_{drop}\right)^{1/3}, \tag{107}$$

where $\mu = \tan\phi$ is the internal friction coefficient of the granular material, ρ_{ball} and $\rho_{granular}$ are the densities of the ball and granular medium, respectively, and H_{drop} is the total vertical distance traveled by the ball. The material properties are selected according to previous studies [43,77,79]. The ball is assigned an intrinsic density of 2200 $\mathrm{kg/m^3}$, a Young's modulus of 200 MPa, and a Poisson's ratio of 0.25. For the granular material, the density is 1510 $\mathrm{kg/m^3}$, the Young's modulus is 2 MPa, and the Poisson's ratio

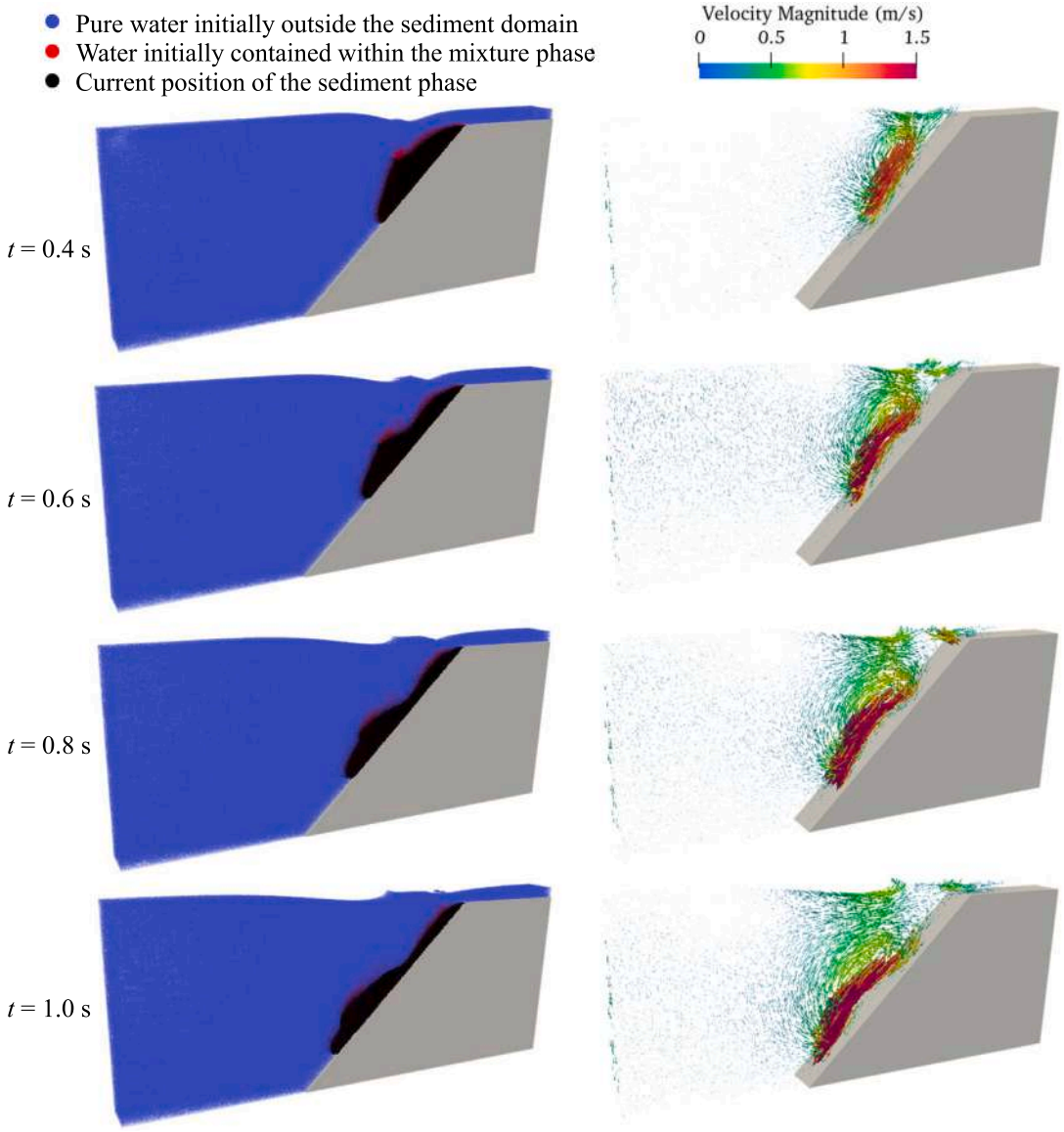

Fig. 15. Submerged granular landslide: snapshots of phase distribution (left) and velocity vector (right) illustrating the water–sediment interaction process. (For interpretation of the references to color in this figure legend, the reader is referred to the web version of this article.)

is 0.3, with zero cohesion and a zero dilation angle. The coefficient ξ^s in the dissipation limiter is set to $50d$ for this case [43], with d being the spatial dimension. A total of 12 computational cases are conducted by varying the ball radius (0.0125 m and 0.02 m), friction coefficient (0.3 and 0.5), and drop height (0.05 m, 0.1 m, and 0.2 m). The initial particle spacing is uniformly set to $dp^s = dp^{rs} = 0.002\,\text{m}$.

Fig. 19 illustrates the spatiotemporal evolution of the velocity vector fields for a representative scenario ($R = 0.02\,\text{m}, H = 0.2\,\text{m}, \mu = 0.5$). Upon impact ($t = 0$ s), the kinetic energy is rapidly transferred from the deformable sphere to the granular bed. The directional evolution of the velocity vectors provides further insight into the cratering mechanics. During the initial stages of penetration ($t = 0.01$ s, 0.02 s, and 0.05 s), the velocity vectors clearly highlight an intense momentum exchange, with granular particles being predominantly expelled upward and outward from the impact zone, leading to the formation of the characteristic raised crater rim. In the subsequent stage ($t = 0.10$ s), as the deformable ball gradually decelerates and approaches its final equilibrium position, the trajectory of the splashed granular material shifts, moving back toward the bottom of the crater under the influence of gravity.

The quantitative validation is summarized in Fig. 20, comparing the simulated penetration depths with empirical benchmarks [77,78] across all cases. The numerical results demonstrate good agreement with the experimental data [77,78], accurately

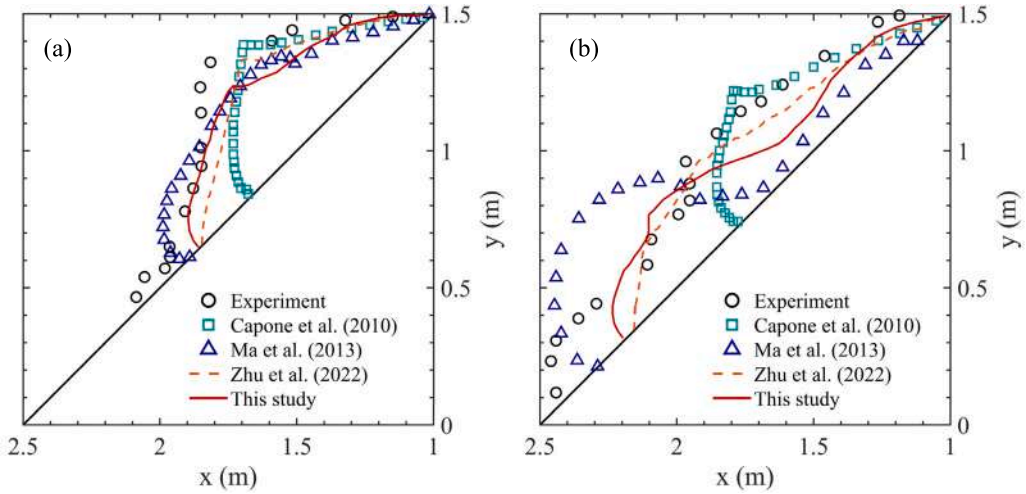

Fig. 16. Submerged granular landslide: comparison of the simulated soil profiles with experimental data [73] and previous numerical results [36,74,75] at (a) $t = 0.4$ s and (b) $t = 0.8$ s.

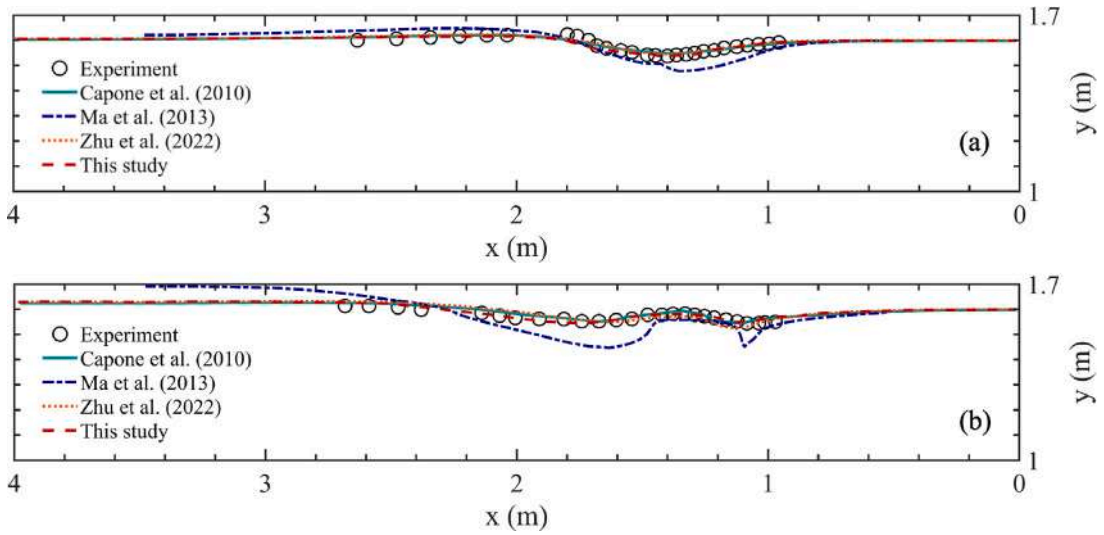

Fig. 17. Submerged granular landslide: comparison of the simulated landslide-induced wave surface with experimental data [73] and previous numerical results [36,74,75] at (a) $t = 0.4$ s and (b) $t = 0.8$ s.

reflecting the sensitivity of the penetration process. This successful verification confirms that the proposed framework is highly robust in resolving dynamic interactions between granular materials and deformable rocks/structures with varying mechanical properties.

A detailed analysis of the interfacial contact force is conducted, as shown in Fig. 21. The temporal evolution of the total vertical contact force exerted by the granular bed on the deformable ball is monitored and compared across three distinct resolution configurations: uniformly fine ($dp^s = 1\,\text{mm}, dp^{rs} = 1\,\text{mm}$), uniformly coarse ($dp^s = 2\,\text{mm}, dp^{rs} = 2\,\text{mm}$), and the proposed multi-resolution setup ($dp^s = 2\,\text{mm}, dp^{rs} = 1\,\text{mm}$). The contact force profiles exhibit high-frequency oscillations during the dynamic penetration phase. These fluctuations are characteristic of SPH contact formulations, primarily originating from discrete particles dynamically entering and exiting the local kernel support domains. Notably, compared to the uniformly coarse configuration, the uniformly fine resolution yields force oscillations with a distinctly higher frequency but noticeably smaller amplitudes. This higher frequency corresponds to the smaller time step constrained by the finer particle spacing, while the reduced amplitude is attributed to the statistically smoother discrete integration over a denser particle distribution. In contrast, the uniformly coarse resolution produces lower-frequency, larger-amplitude fluctuations. As expected, the transient force profile of the multi-resolution scheme naturally falls between the two uniform cases, inheriting the macroscopic interaction radius of the coarse soil phase while benefiting from the refined integration points of the solid phase. Most importantly, despite these microscopic transient variations, the total vertical contact forces in all three configurations converge to the same macroscopic steady-state value as the ball reaches its final

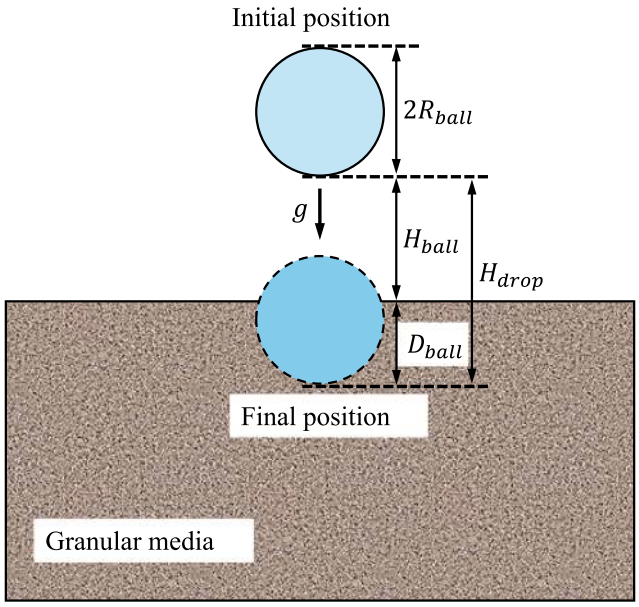

Fig. 18. Low-speed impact craters: schematic illustration of the initial model setup and computational configuration.

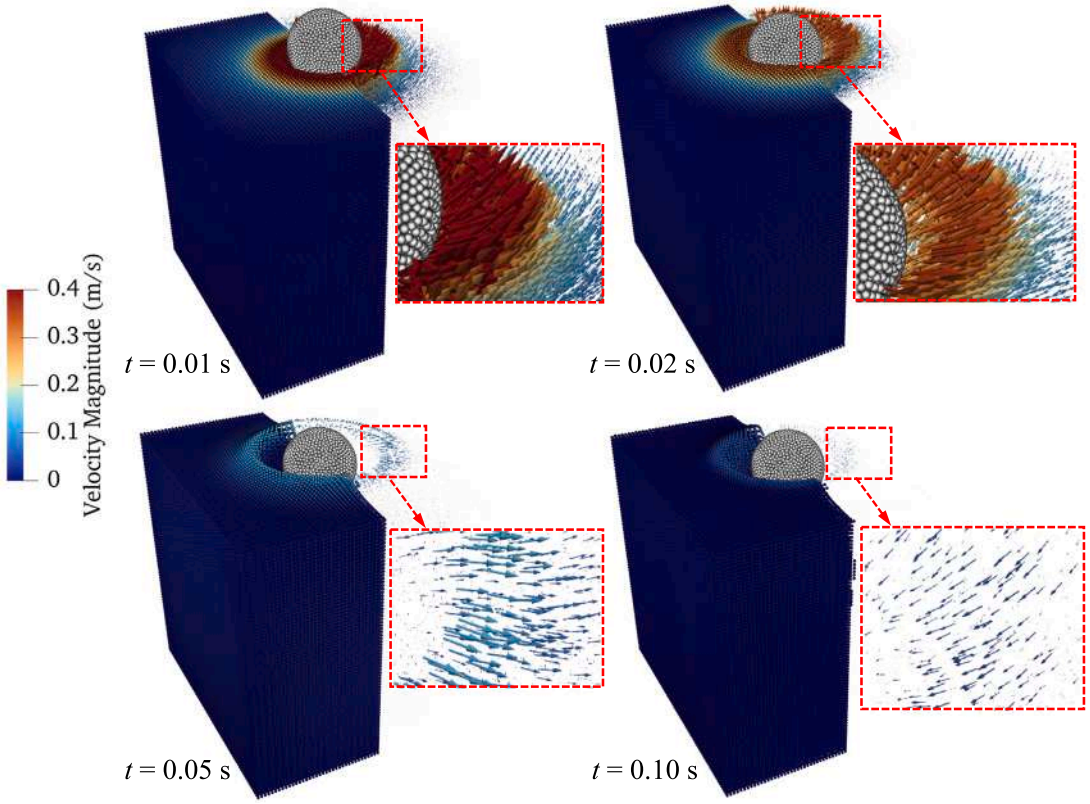

Fig. 19. Low-speed impact craters: spatiotemporal evolution of velocity vector fields at typical time instants ($R = 0.02$ m, $H = 0.2$ m, $\mu = 0.5$).

equilibrium. This quantitative evidence conclusively demonstrates that the present multi-resolution coupling strategy is consistent, preserving global momentum and macroscopic kinematics while avoiding the prohibitive computational costs associated with a uniformly fine discretization.

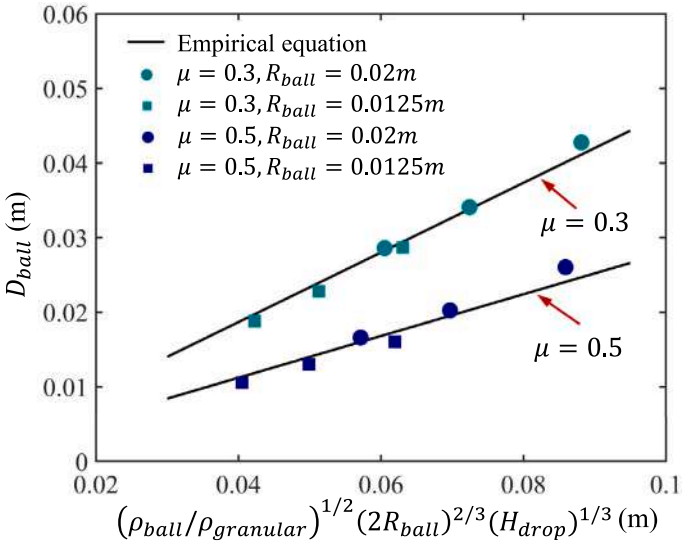

Fig. 20. Low-speed impact craters: comparative analysis of penetration depth across varying friction coefficients, ball radii, and drop heights, validated against empirical benchmarks [77,78].

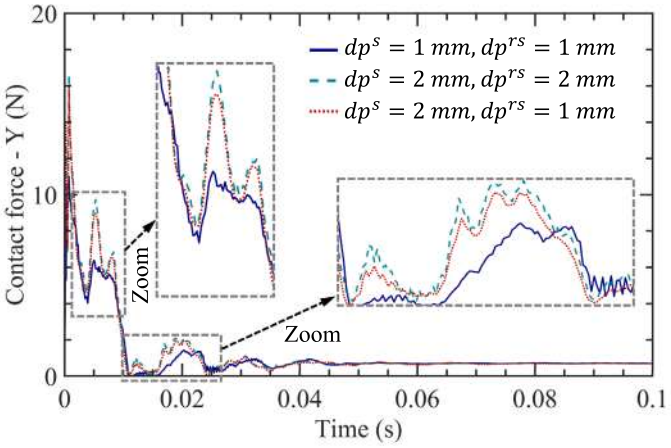

Fig. 21. Low-speed impact craters: temporal evolution of the total vertical contact force exerted by the granular bed on the ball under different spatial resolution configurations ($R = 0.02$ m, $H = 0.2$ m, $\mu = 0.5$).

4.5. Dam-break impact on an elastic plate

To evaluate the robustness of the proposed multiphase framework in resolving hydroelastic problems involving violent free-surface flows and significant structural response, we simulate the benchmark case of a dam-break flow impacting a flexible barrier. This study replicates the experimental configuration established by Liao et al. [80], which has become a standard test for validating fluid–structure interaction (FSI) solvers [81–83].

The model configuration is depicted in Fig. 22. The system consists of a water column ($H = 0.2$ m, $L = 0.4$ m) initially confined in a rectangular tank. An elastic rubber plate is vertically fixed to the tank floor at a distance of 0.2 m downstream from the water column. The water density is $\rho_0^w = 1000$ kg/m^3. The plate possesses a density $\rho_0^{rs} = 1164.0$ kg/m^3, a Young's modulus $E = 3.5$ MPa, and a Poisson's ratio $\nu = 0.49$. To accurately model the gate removal, which significantly influences the initial wave front, the vertical motion of the gate is prescribed using the experimentally-derived polynomial $h_g(t) = -285.115t^3 + 72.305t^2 + 0.1463t$ [84].

A key feature of the present simulation is the employment of a multi-resolution discretization strategy to balance local accuracy with global computational efficiency. The water phase is discretized using a particle spacing of $dp^w = 2$ mm, while the thin elastic plate is locally refined with a spacing of $dp^{rs} = 1$ mm, ensuring four layers of particles across its thickness ($d = 4$ mm). By utilizing this 2:1 resolution ratio, the total particle count for the water domain is maintained at approximately 2 million. In contrast, a uniform discretization at the finer resolution ($dp^w = dp^{rs} = 1$ mm) would necessitate roughly 16 million water particles. This multi-resolution

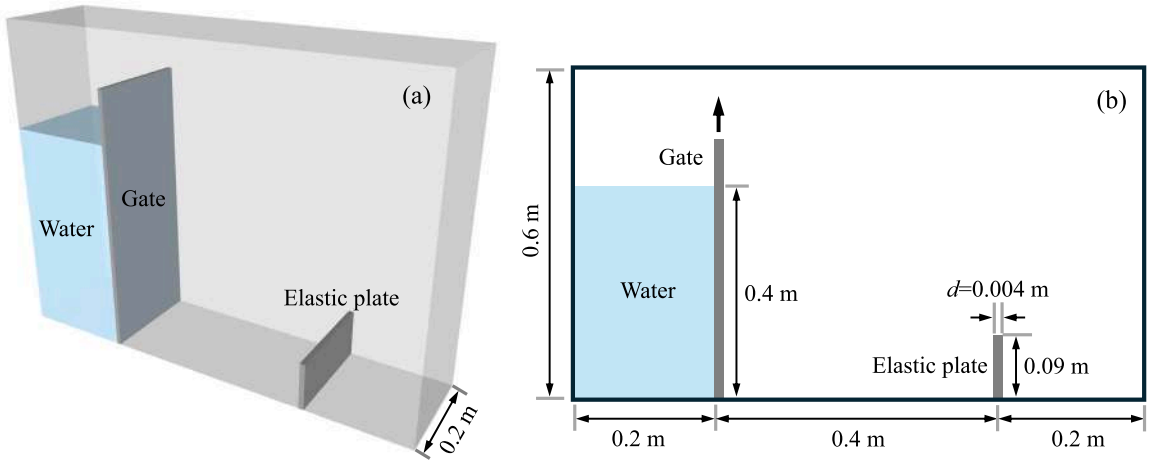

Fig. 22. Dam-break impact on an elastic plate: (a) 3D view of the model setup, and (b) front view with geometric dimensions indicated.

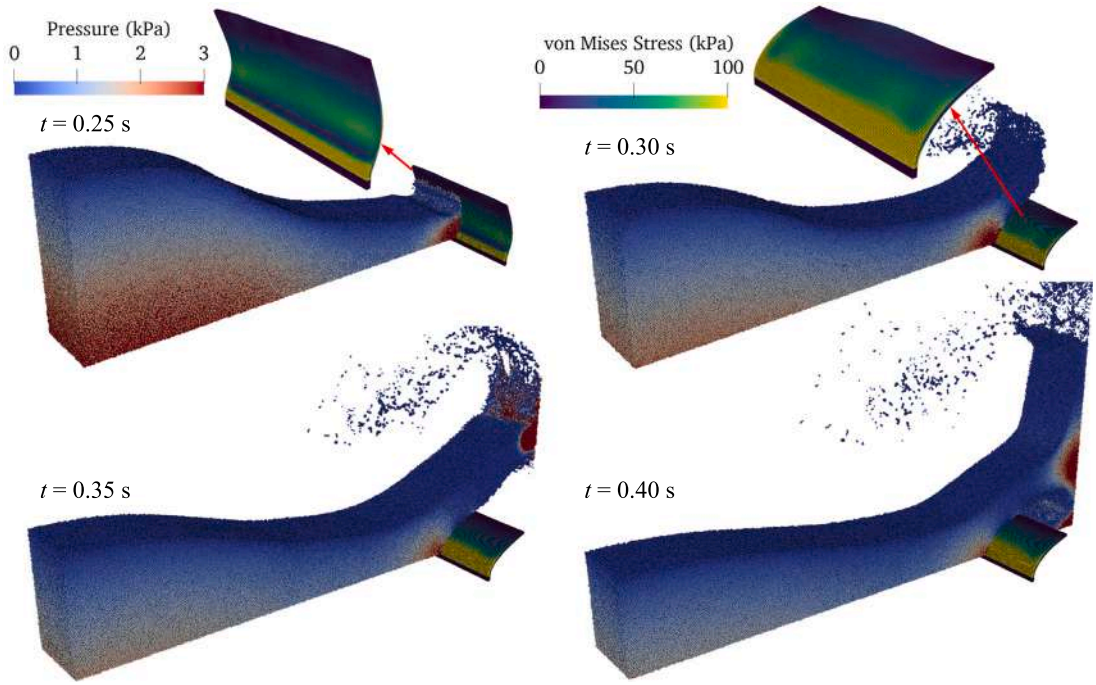

Fig. 23. Dam-break impact on an elastic plate: snapshots of fluid pressure and solid von Mises stress at typical time instants, illustrating the dynamic fluid–structure interaction. To facilitate visualization, only half of the water domain is displayed.

approach achieves an eight-fold reduction in the fluid particle count, significantly accelerating the simulation without compromising the structural resolution required to capture bending modes.

The dynamic evolution of the system is illustrated in Fig. 23, which showcases the fluid pressure field and the corresponding von Mises stress within the plate. At $t = 0.25$ s, the collapsing water column impinges on the elastic plate, with the hydrodynamic loading predominantly concentrated on its lower-middle section. Consequently, the plate exhibits a clear arc-shaped deflection. By $t = 0.3$ s, as the water volume continues to surge against the structure, the plate undergoes further bending. Under the guidance of the inclined plate profile, the fluid momentum is redirected toward the upper-right portion of the tank. During the later stages ($t = 0.35$–0.4 s), the water column strikes the right wall, where a portion of the fluid splashes upward while the remainder descends to the tank floor under the influence of gravity. Throughout the entire interaction process, both the fluid pressure and the structural von Mises stress maintain smooth and continuous distributions. This demonstrates the numerical stability of the proposed multi-resolution coupling scheme, which avoids spurious oscillations even during violent impact and large structural deformations. The free-surface

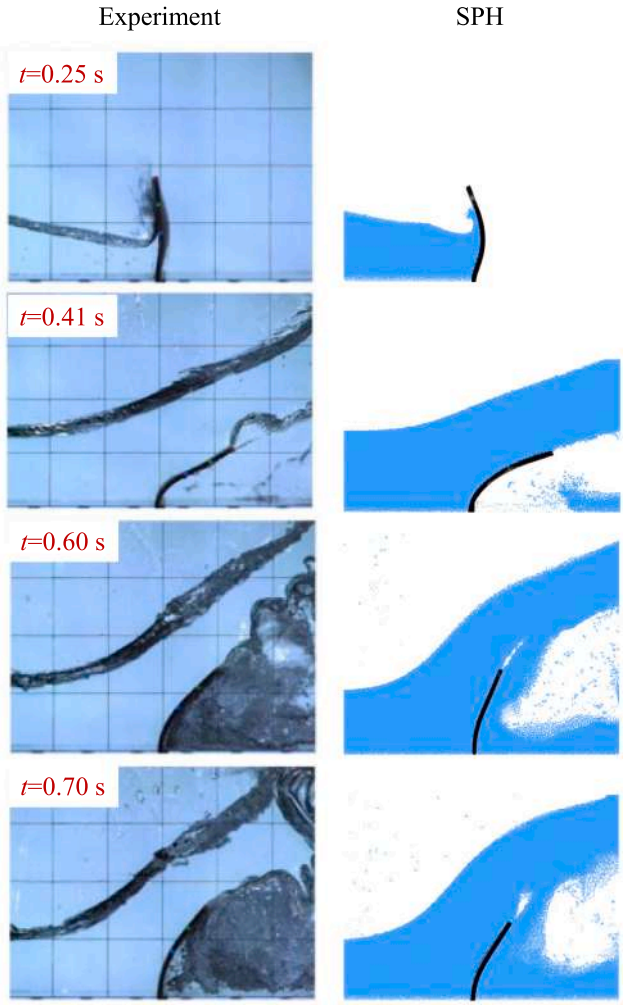

Fig. 24. Dam-break impact on an elastic plate: morphological evolution of the water–structure system compared with experimental observations [80] at typical time stages.

morphology and structural deformation are qualitatively compared with experimental snapshots in Fig. 24, demonstrating that the current SPH method faithfully captures the splashing, run-up, and structural bending observed in the physical tests.

Quantitatively, the structural response is evaluated by monitoring the horizontal tip displacement of the elastic plate. As shown in Fig. 25, the simulated time history of the tip displacement is compared with the experimental measurements of Liao et al. [80] and previous numerical results [81,82]. The simulated time-history profile of the tip displacement matches the experimental data well. Although a slight deviation is observed after $t = 0.45$ s — likely due to the absence of the "air-cushion" effect [81,85] since the air phase is not explicitly modeled — the overall accuracy confirms that the proposed multi-resolution SPH framework is highly effective for simulating complex 3D FSI problems with high efficiency and precision.

To evaluate the stability of the decoupled time-stepping scheme and thoroughly investigate the energy evolution and transfer during fluid–structure interactions, the time history of the total mechanical energy of the water body is analyzed. As depicted in Fig. 26, the total mechanical energy profiles under three different spatial resolutions are monitored. Prior to the fluid impinging on the elastic plate ($t < 0.25$ s), the total mechanical energy remains exceptionally stable and nearly constant. Noticeable reductions in the water's mechanical energy occur precisely at three key dynamic events: striking the elastic plate at $t \approx 0.25$ s, impacting the right tank wall at $t \approx 0.35$ s, and subsequently at $t \approx 0.88$ s when the splashed water mass plunges back down and violently interacts with the underlying fluid pool. These discrete drops are physically reasonable, corresponding to the macroscopic energy transfer to the deforming solid structure (as structural strain and kinetic energy) and the inevitable energy dissipation associated with violent free-surface fragmentation, fluid mixing, and viscous effects. Importantly, the energy profiles evolve smoothly without exhibiting any non-physical, high-frequency oscillations throughout the entire interaction process. Moreover, the energy curves clearly converge as the fluid resolution is refined from $dp^w = 4$ mm to 2 mm, further validating the accuracy and robustness of the proposed multi-resolution coupling strategy.

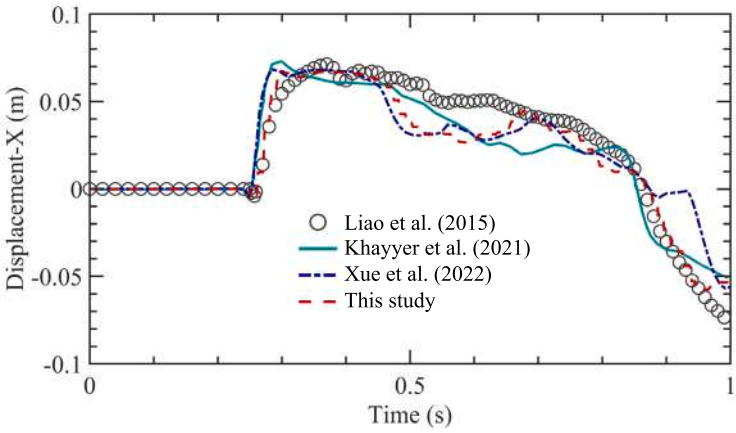

Fig. 25. Dam-break impact on an elastic plate: temporal evolution of the plate's horizontal tip displacement compared with experimental data (Liao et al., 2015 [80]) and previous numerical results (Khayyer et al., 2021 [81]; Xue et al., 2022 [82]).

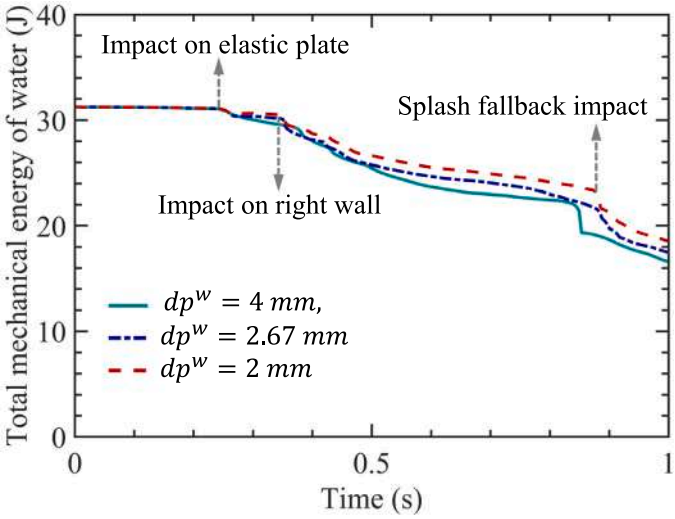

Fig. 26. Dam-break impact on an elastic plate: temporal evolution of the total mechanical energy of the water body under three different spatial resolutions ($dp^w = 4, 2.67, 2$ mm), while maintaining a constant resolution ratio of $dp^{rs} = 0.5dp^w$.

4.6. Colliding rubber balls

To validate the proposed algorithm in handling solid–solid interactions (*e.g.*, contact between rocks or structures) involving large deformations, the 3D collision of two hollow rubber balls [86,87] is simulated using the total Lagrangian framework. The geometric configuration is illustrated in Fig. 27. Two identical hollow spheres, each with an inner radius of $R_{in} = 0.03$ m and an outer radius of $R_{out} = 0.04$ m, are positioned with an initial center-to-center distance of 0.09 m. They are initialized with opposite velocity vectors of magnitude $v_0 = 0.08c_0$ (where c_0 is the speed of sound and can be calculated by Eq. (53)), resulting in a high-speed head-on collision. Two observation points, S1 and S2, are located at the leftmost and rightmost extremities of the left and right balls, respectively. To ensure a high-quality initial discretization, a level-set-based packing algorithm [40] is employed to generate a uniform particle distribution with an initial spacing of $dp^{rs} = 0.001$ m. Following Refs. [16,86,87], the material properties are: the density is set to $\rho_0 = 1200$ kg/m^3, Young's modulus to $E = 10$ MPa, and Poisson's ratio to $\nu = 0.4$.

The qualitative performance of the solver is demonstrated in Fig. 28, which depicts the spatiotemporal evolution of the von Mises stress distribution. For clarity, a cross-sectional view of the stress field is presented. As the spheres make contact, the kinetic energy is rapidly converted into internal strain energy, creating high-stress zones at the impact interface. The results show that the stress field remains smooth and continuous throughout the compression and rebound phases. Moreover, the particle configuration maintains its geometric integrity without exhibiting numerical instabilities.

To provide a quantitative assessment of the conservation properties, Fig. 29a analyzes the time history of the system's energy components. A reciprocal conversion between kinetic energy and elastic strain energy is clearly observed. The kinetic energy reaches

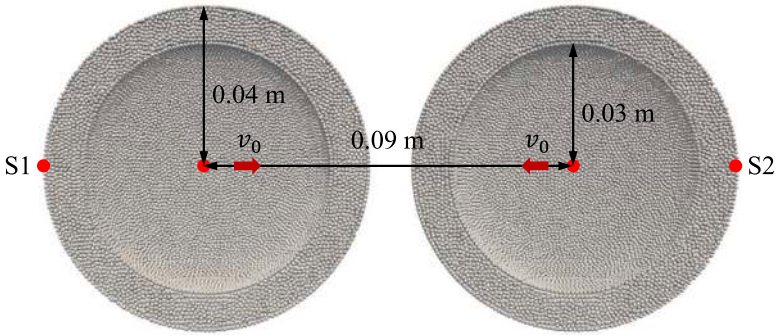

Fig. 27. Colliding rubber balls: schematic illustration of the initial geometric setup.

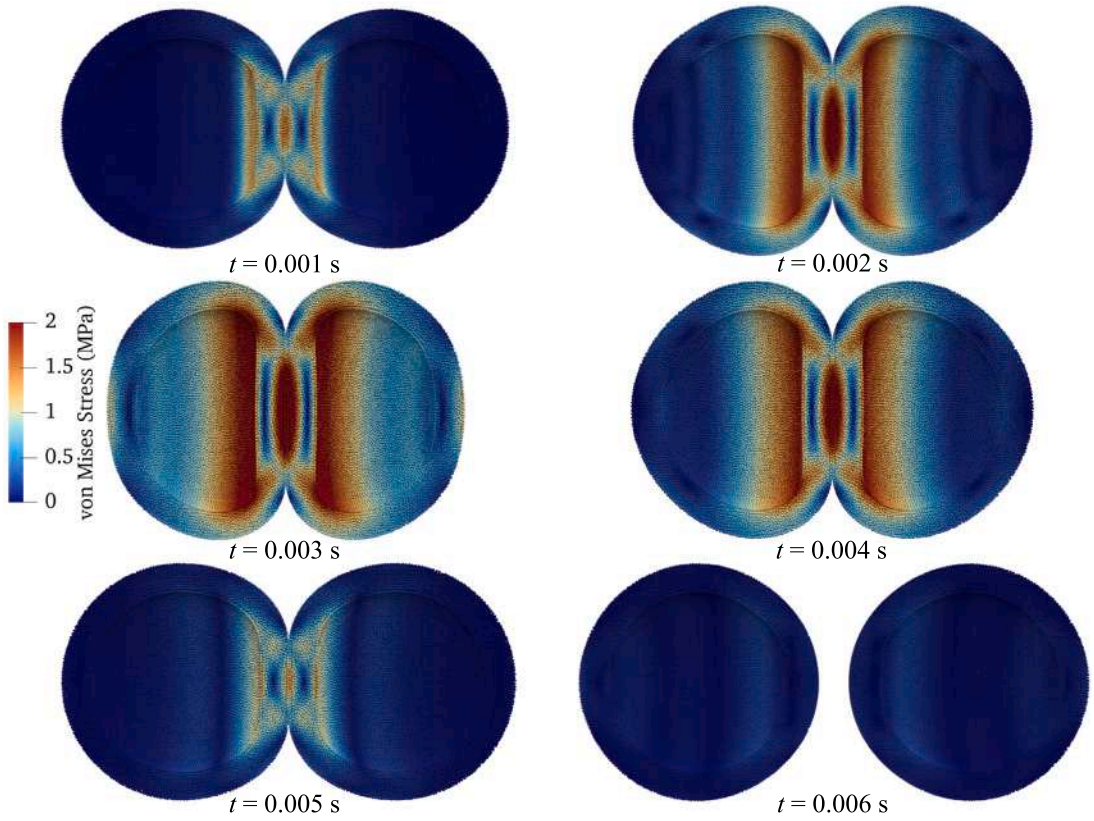

Fig. 28. Colliding rubber balls: spatiotemporal evolution of the von Mises stress distribution during the impact process ($v_0 = 0.08c_0$).

its minimum at approximately $t \approx 0.003$ s (the moment of maximum compression), coinciding with the peak of the elastic strain energy. Following the rebound, the stored strain energy is released back into kinetic energy. This energy evolution, including the phase and magnitude of the conversion, is in good agreement with the results reported by Zhang et al. [87] using the SPH-GNOG formulation, as shown in Fig. 29a. Additionally, Fig. 29b tracks the displacement history of the observation points on the balls. The symmetric trajectories further validate the physical consistency of the collision dynamics captured by the present method.

5. Validation of three-phase granular–water–rock/structure interactions

5.1. Leakage of granular–water mixture with an immersed elastic plate

To validate the proposed framework in handling complex three-phase interactions (granular–water–structure coupling), a simulation of a granular–water mixture leaking through a bottom crack is conducted. This benchmark is adapted from the

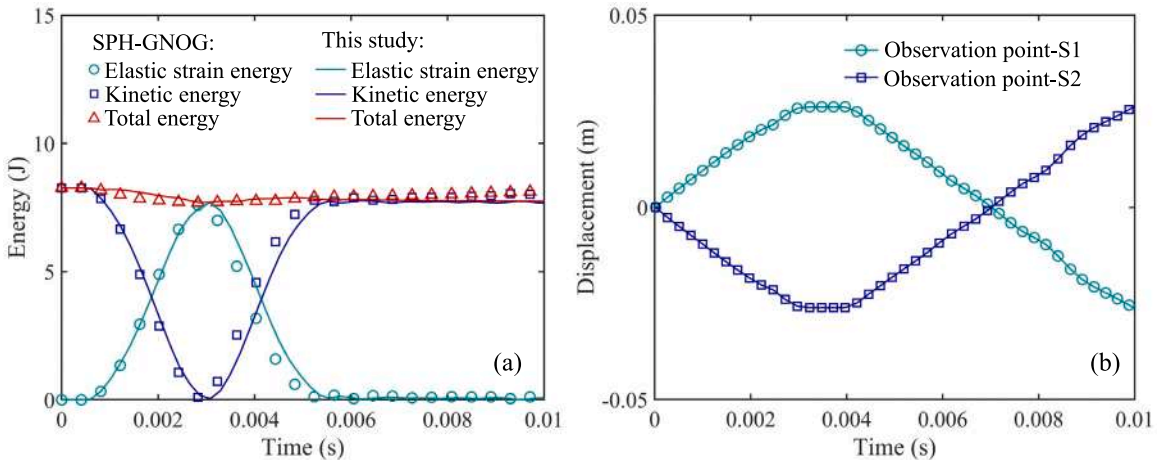

Fig. 29. Colliding rubber balls: quantitative analysis of the impact dynamics. (a) Time evolution of the system energy components; (b) displacement histories of the two observation points.

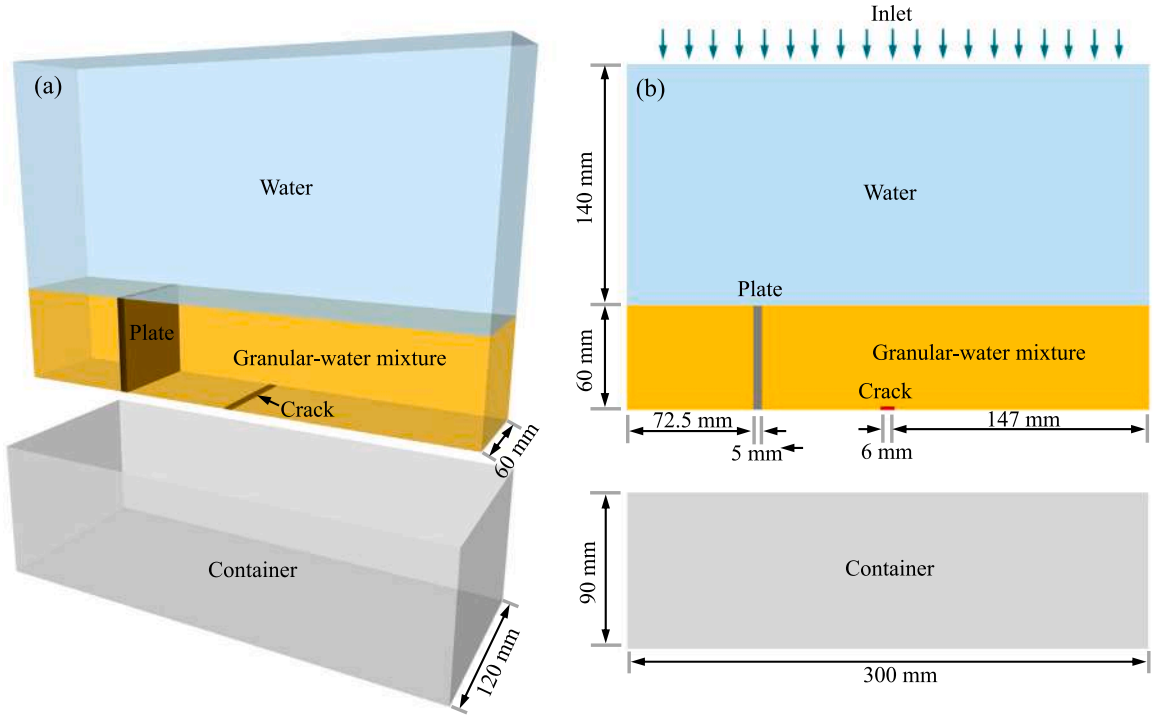

Fig. 30. Leakage of granular–water mixture: (a) 3D view of the model setup, and (b) front view with geometric dimensions indicated.

experimental work by Zhang et al. [88]. Unlike the previous cases involving external impact, this scenario focuses on the hydroelastic response of an elastic plate immersed within the granular bed, where the structural deformation is driven by the internal flow and particle movements during the discharge process.

As shown in Fig. 30, the geometric setup consists of a rectangular tank containing a mixture of water and granular materials. An elastic plate is vertically installed, with its lower end completely clamped to the bottom wall. The plate is fully submerged in the water, and its top end is initially flush with the free surface of the granular bed. The water and granular materials discharge through a bottom crack and fall into a receiving container below. Although the original physical experiment did not record the kinematic states of the mixture after exiting the crack, the present study explicitly simulates the complete dynamic process, including the outflow and subsequent accumulation, to comprehensively validate the stability and robustness of the proposed numerical framework. The

water phase follows the standard Newtonian fluid model, with a reference density of $\rho_0^w = 1000\,\mathrm{kg/m^3}$ and a dynamic viscosity of $\mu_f = 0.001\,\mathrm{Pa\,s}$. The elastic plate is characterized by a density of $\rho_{rs} = 1000\,\mathrm{kg/m^3}$, a Young's modulus of $E_{rs} = 10\,\mathrm{MPa}$, and a Poisson's ratio of $\nu_{rs} = 0.4$ [88].

It is important to note that while the reference experiment utilized discrete steel balls, the present study models the granular phase as a continuum elastoplastic material using the proposed SPH formulation. This macroscopic approach is valid for dense granular flows where the collective behavior dominates. According to the physical experiment [88], the granular phase is assigned a density of $\rho_s = 7850\,\mathrm{kg/m^3}$, a Poisson's ratio of 0.25, and zero cohesion. While the intrinsic Young's modulus of solid steel is typically around 200 GPa (as adopted in the reference DEM modeling [88] for microscopic particle contacts), using such a high value in an explicit continuum solver like SPH would yield an excessive speed of sound, leading to prohibitively small time steps. From a physical perspective, the Young's modulus in the present continuum D–P model represents the equivalent macroscopic stiffness of the bulk granular matrix. According to micromechanical contact theories [89] and particulate mechanics [90], this macroscopic stiffness is governed by the compliance of the inter-particle contact network rather than the intrinsic solid mineral stiffness, and is naturally several orders of magnitude lower. This phenomenological reduction is a standard practice in continuum modeling of granular media [17]. Thus, an equivalent macroscopic Young's modulus of $E_s = 100\,\mathrm{MPa}$ is adopted in this study.

In the continuum SPH modeling of the granular phase, the macroscopic internal friction angle must be carefully assigned. The reference DEM study assumed a frictionless microscopic contact ($\mu_s = 0$) for the submerged steel balls. However, as fundamentally demonstrated by Refs. [91,92], the macroscopic shear strength of a random assembly of spherical particles is dominated by geometric interlocking and kinematic constraints rather than mere interparticle sliding. Skinner's experiments [92] confirmed that even under heavily lubricated conditions with minimal microscopic friction, the macroscopic constant-volume friction angle of spherical assemblies remains stable (approximately 26°). Therefore, to accurately account for this geometric interlocking effect within the homogenized SPH framework, a macroscopic internal friction angle of $\phi = 26°$ is adopted in the present simulation.

Appropriate boundary conditions are crucial for reproducing the physical leakage process accurately and efficiently. No-slip boundary conditions are applied to the left, right, and bottom walls of the tank. A pressure boundary condition is imposed at the top boundary of the water domain, acting as an inlet (pressure is zero) to maintain a constant water level throughout the discharge process.

Fig. 31 illustrates the dynamic evolution of the fluid–granular–structure interaction during the leakage process at four representative time instants (t = 1.6, 3.2, 4.8, and 6.0 s). In these visualizations, the water and granular materials are rendered in blue and yellow, respectively, focusing on the kinematic and morphological progression of the multiphase system. As the mixture discharges through the bottom crack, the macroscopic flow in the upper tank continuously drives the progressive bending of the immersed elastic plate. Meanwhile, the post-discharge accumulation in the bottom receiving container exhibits distinct multiphase dynamic features. In the early stage (t = 1.6 s), the granular materials are severely flushed and dispersed laterally by the initial high-momentum water flow, leaving the central impact zone relatively devoid of granular accumulation. However, as the discharge progresses and the solid mass flux increases at subsequent times ($t \geq 3.2$ s), the granular phase gradually dominates the deposition process. The discharged particles continuously pile up at the center, overcoming the initial fluid wash-out effect, and eventually form a distinct heap characterized by a higher central peak and lower edges. This transition from fluid-driven dispersion to gravity-dominated granular accumulation vividly demonstrates the robust capability of the proposed SPH framework in capturing complex, large-deformation multiphase behaviors.

Fig. 32 illustrates the frontal-view evolution of the granular–water mixture and the immersed elastic plate at t = 1.6, 3.2, 4.8, and 6.0 s. As the leakage proceeds, the granular bed develops a progressive inward subsidence, eventually forming a distinct triangular crater. To quantitatively validate the macroscopic soil flow, the dynamic angle of the resulting granular slope is measured. The SPH-predicted slope angles at the four respective instants are 19.1°, 19.5°, 20.2°, and 20.1°. These results align well with the experimental measurements of 19.8°, 20.4°, and 19.9° recorded at t = 1.6, 4.8, and 6.0 s [88]. Furthermore, as shown in the bottom-left inset of Fig. 32, the von Mises stress distribution within the severely deformed elastic plate remains highly smooth and free of non-physical numerical oscillations, verifying the robustness of the fluid–soil–structure coupling.

To achieve both high computational efficiency and structural accuracy, a multi-resolution strategy is employed in this simulation. As depicted in the top-left enlarged view of Fig. 32, the initial particle spacing for the granular and water phases is set to $dp^s = dp^w = 2.5$ mm, while a finer resolution of $dp^{rs} = 1.25$ mm is assigned to the elastic plate. This localized refinement ensures that four layers of particles are arranged across the plate's thickness, providing sufficient resolution to accurately capture the structural bending modes. Benefiting from this multi-resolution scheme, the total number of initial fluid and soil particles is successfully constrained to 391.5 thousand. By contrast, if a uniform high resolution of 1.25 mm were adopted for the entire domain, the total particle count for the mixture would soar to approximately 3.13 million. Therefore, the proposed multi-resolution approach significantly reduces the computational burden while maintaining high-fidelity physical responses.

Next, we proceed to compare the SPH-predicted horizontal tip displacement of the plate with the experimental measurements. As depicted in Fig. 33, the experimental displacement exhibits a distinct S-shaped transient response with noticeable local fluctuations, whereas the SPH continuum results present a smoother, strictly monotonic ascent. Specifically, the SPH simulation initiates macroscopic movement slightly earlier than the experiment; at $t \approx 1.0$ s, the SPH tip deflection reaches approximately 0.2 mm, while the physical measurement remains constrained below 0.1 mm. Subsequently, the physical experiment demonstrates a sharp acceleration, crossing over and surpassing the SPH prediction around $t = 4.4$ s. Eventually, by the end of the experimental recording period at $t \approx 6.4$ s, both curves converge to a similar magnitude of approximately 14.6 mm. This phenomenological discrepancy is fundamentally rooted in the physical differences between discrete granular mechanics and continuum homogenization. In the physical experiment, the dense granular bed initially resists movement due to strong inter-particle interlocking and static friction.

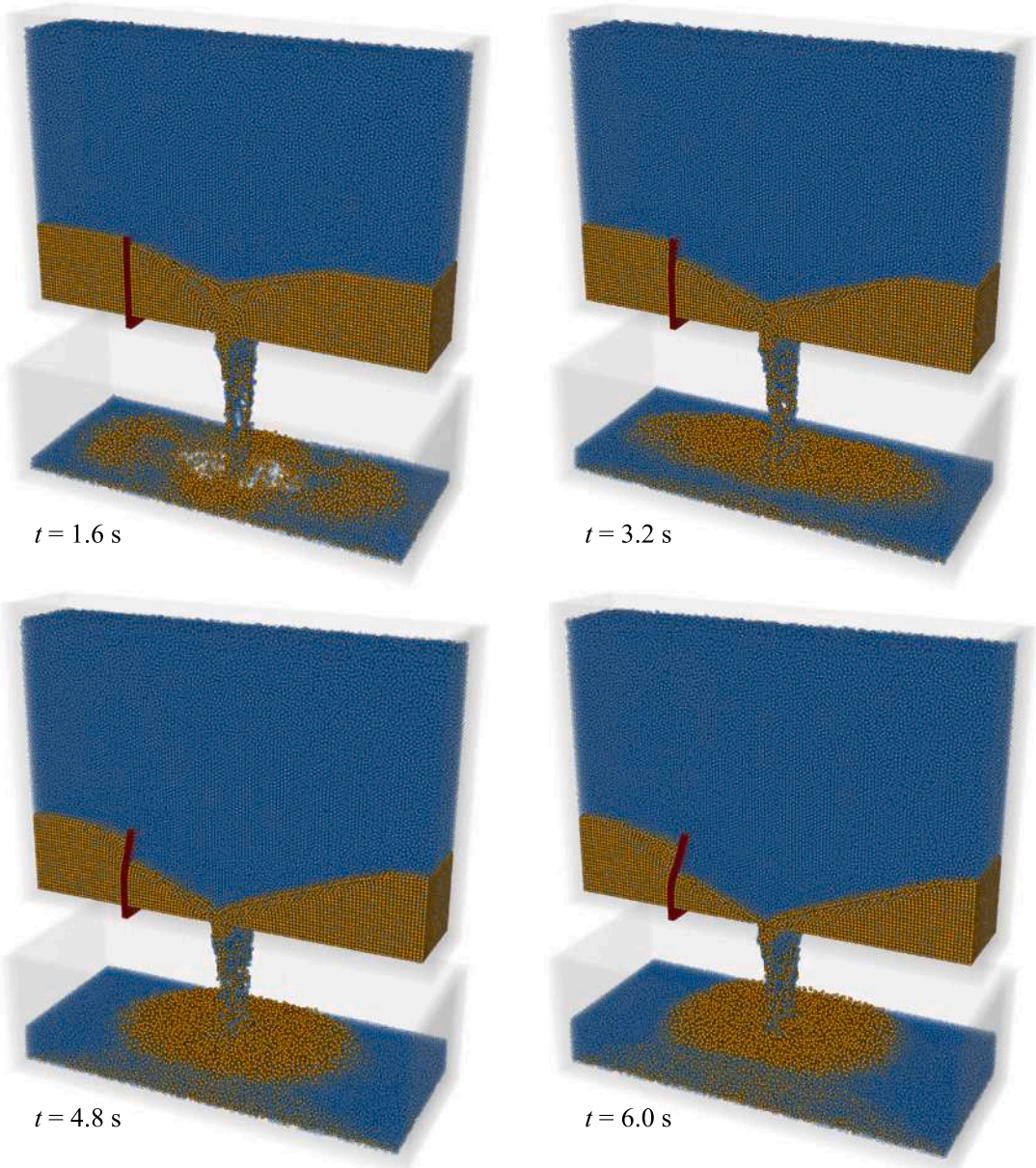

Fig. 31. Leakage of granular–water mixture: sequential snapshots illustrating the multiphase flow dynamics and the concurrent deformation of the immersed elastic plate at representative time instants. (For interpretation of the references to color in this figure legend, the reader is referred to the web version of this article.)

This localized mechanism is evidenced by the minor fluctuations in the experimental data (*e.g.*, the oscillation observed between $t = 1.5$ s and $t = 2.0$ s), where internal force-chains intermittently build up and collapse. In contrast, the SPH framework utilizes a macroscopic D–P elastoplastic model. By homogenizing the particulate medium, this continuum approach responds to stress gradients continuously and monotonically. Lacking the discrete capability to capture micro-mechanical static interlocking and stick–slip energy release, the SPH model yields an earlier but more uniformly distributed, viscous-like macroscopic flow. The transient deviation in the late stage can be attributed to the combined effects of the constitutive simplification and the boundary treatment. Physical granular media naturally arrest and dissipate shear traction via Coulomb friction as the material discharge loses momentum. However, the ideal perfectly-plastic yielding assumed in the current D–P model may over-predict residual flowing tendencies. Compounded by the no-slip boundary condition adopted in the SPH framework, the continuum soil artificially maintains a continuous downward “drag” on the structure.

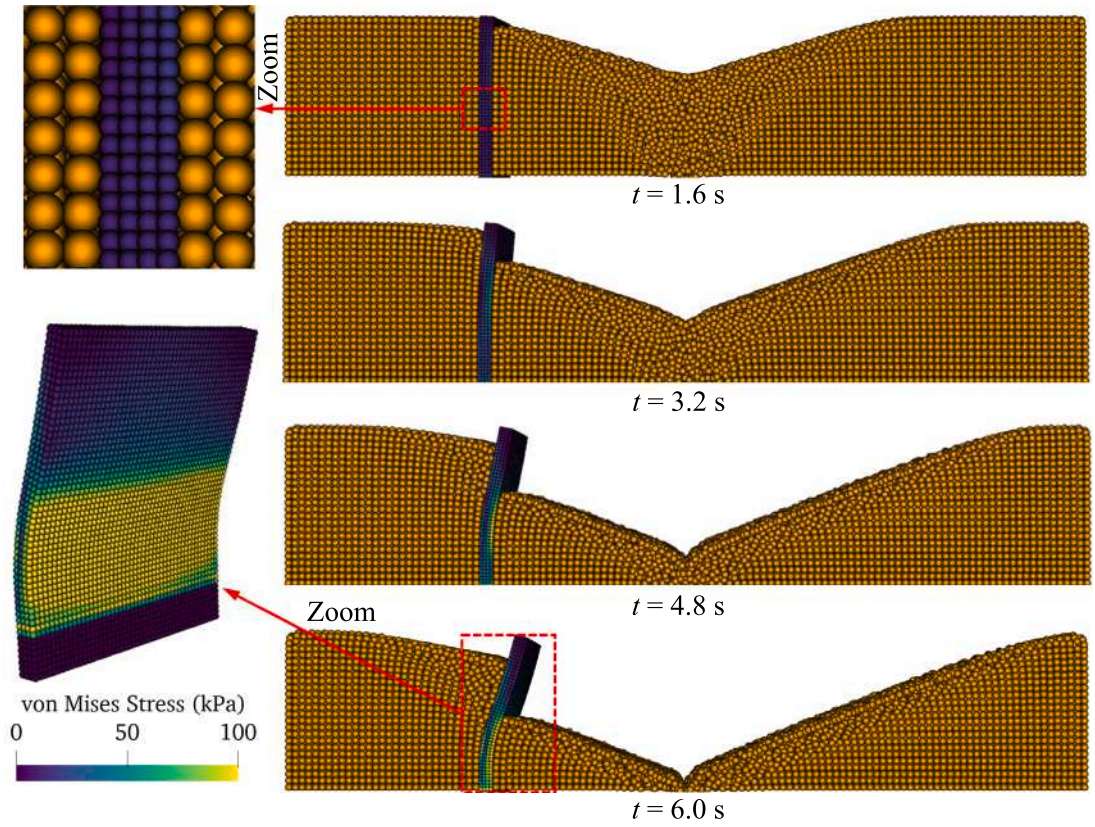

Fig. 32. Leakage of granular–water mixture: frontal-view snapshots depicting the dynamic flow of the granular materials and the structural bending of the elastic plate (colored by von Mises stress) at representative time instants. (For interpretation of the references to color in this figure legend, the reader is referred to the web version of this article.)

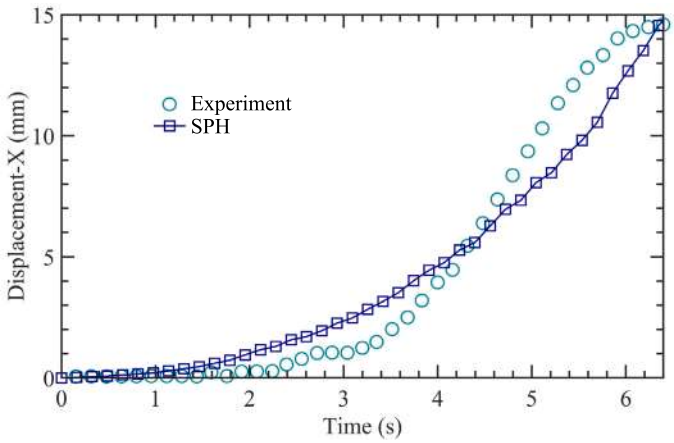

Fig. 33. Leakage of granular–water mixture: temporal evolution of the horizontal tip deflection of the elastic plate, validated against experimental measurements [88].

Despite these transient deviations arising from the inherent continuum approximations, the proposed SPH solver demonstrates a robust capability in capturing the fluid–soil–structure coupling dynamics, effectively predicting the final deformation state and providing a highly computationally efficient macroscopic framework for complex engineering applications.

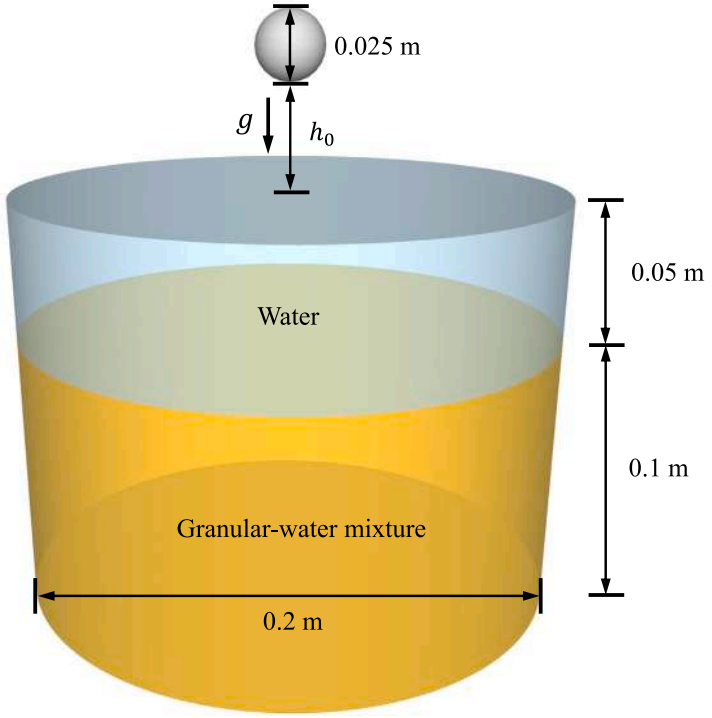

Fig. 34. Sphere impacting a submerged granular bed: model setup.

5.2. Crater formation by a sphere impacting a submerged granular bed

To further assess the capability of the proposed multiphase SPH solver in capturing highly dynamic fluid-particle interactions under extreme strain rates, the physical experiment of a sphere impacting a submerged granular bed, as reported by Grimaldi and Dressaire [93], is simulated. While the previous leakage case features a quasi-static discharge process, this benchmark is characterized by a violent collision that triggers instantaneous local fluidization, rapid pore water ejection, and subsequent macroscopic crater formation.

The computational domain consists of a cylindrical container with a diameter of 0.2 m, partially filled with a densely packed granular bed with a height of 0.1 m. The granular bed is fully submerged under a supernatant water layer with a depth of 0.05 m. As illustrated in Fig. 34, the spherical projectile, having a diameter of $D = 0.025$ m, is released from an initial drop height h_0, measured from the bottom of the sphere to the undisturbed water surface. The ambient fluid is treated as a standard Newtonian fluid with a reference density of $\rho_0^w = 1000\,\mathrm{kg/m^3}$ and a dynamic viscosity of $\mu_f = 0.001$ Pa s. The projectile is explicitly modeled with a density of $\rho_{rs} = 2200\,\mathrm{kg/m^3}$, an equivalent Young's modulus of $E_{rs} \approx 500$ MPa, and a Poisson's ratio of $\nu_{rs} = 0.46$ to match the properties of the Teflon sphere used in the experiments.

For the continuum representation of the granular phase, the required macroscopic properties are estimated from established particulate physics to compensate for the missing micromechanical parameters in the original visual report [93]. The bed consists of monodisperse 500 μm glass beads, dictating a characteristic length of $D_c = 0.0005$ m for the evaluation of the non-linear fluid–solid drag forces. As the experimental bed is explicitly described as "densely packed", the initial solid volume fraction is set to 0.64, which is consistent with the commonly adopted random-close-packing limit for approximately monodisperse spheres. The intrinsic solid density of the glass material is set to $\rho_s = 2500\,\mathrm{kg/m^3}$.

Mechanically, the submerged glass beads are modeled as a cohesionless elastoplastic material obeying the D–P yield criterion. The macroscopic cohesion is strictly set to zero ($c = 0$). Physically, the complete submergence eliminates all air–water interfaces, thereby neutralizing any apparent cohesion induced by capillary bridge effects. Furthermore, due to the macroscopic size of the particles (500 μm), inter-particle physico-chemical interactions are negligible. The macroscopic internal friction angle is set to $\phi = 26°$. This value is a well-documented constant-volume residual shear strength for spherical glass assemblies subjected to large deformations, as experimentally validated by Skinner [92].

Additionally, an equivalent macroscopic Young's modulus of $E_s = 20$ MPa and a Poisson's ratio of $\nu_s = 0.3$ are adopted for the granular skeleton. This severe phenomenological reduction from the intrinsic stiffness of solid glass (~70 GPa) explicitly accounts for the extreme compliance of the inter-particle contact network under the very low confining pressures typical of shallow submerged beds [89,90]. The reference particle spacing is $dp^s = dp^w = dp^{rs} = 0.001$ m. Here, dp^w denotes the clear-water reference spacing. Equal-mass water particles inside the saturated granular bed are generated by the proposed relaxation procedure. No-slip solid

boundaries are imposed on the walls and bottom of the tank. During the simulation, the high-speed penetration of the sphere violently displaces the interstitial water, generating immense transient pore pressures and non-linear drag forces. This benchmark serves as a stringent test for the proposed coupling scheme's ability to smoothly handle localized fluidization and fluid-driven granular cratering without numerical instability.

Fig. 35a illustrates the spatiotemporal evolution of the multiphase system, depicting the positions and particle distributions of the fluid, the granular bed, and the projectile ($h_0 = 1$ m). The temporal sequence is anchored at $t = 0$ ms, defined as the precise instant the sphere contacts the free water surface. Upon entry, the projectile aggressively displaces the fluid, carving out an expanding open cavity while ejecting a pronounced splash crown radially outward. At $t = 14.6$ ms, the sphere strikes the submerged granular surface. At this juncture, the fluid phase exhibits a characteristic U-shaped open void, which is wider at the free surface and narrows toward the projectile. As the penetration proceeds, the sphere forcefully displaces the granular material radially and downward, excavating a distinct macroscopic crater. In the late stages of the simulation, following the maximum penetration, a prominent upward fluid column — characteristically known as a Worthington jet [94–96] — emerges above the sphere, driven by the violent hydrodynamic collapse of the fluid cavity.

Fig. 35b provides a direct visual comparison of the macroscopic fluid distribution between the SPH simulation and the experimental photographs at two critical instants: the initial granular impact ($t = 14.6$ ms) and the late-stage cratering ($t = 114.6$ ms). At $t = 14.6$ ms, the SPH solver successfully captures the general macroscopic envelope of the fluid displacement, with the overall height and width of the splash crown aligning adequately with the experiment. However, subtle kinematic deviations are already discernible. In the experimental observation, aerodynamic drag and surface tension cause the splash to spread radially while its edges begin to decelerate and curl downward. In contrast, the SPH fluid particles, uninhibited by an ambient air phase, maintain a purely ballistic upward and outward trajectory.

Noticeable phenomenological discrepancies become more prominent at the late stage ($t = 114.6$ ms). In the physical experiment, the splashed water has decelerated and closed inward, forming an umbrella-like surface seal (dome) over the cavity. The isolated droplet column visible at the top is essentially a weak upward jet generated by the pinch-off of this surface seal above the free surface [96]. In reality, the formation of a classic, thick Worthington jet from the deep cavity is physically suppressed in this experimental setup; the relatively shallow water depth and the rapid penetration of the projectile into the granular bed effectively block the deep radial fluid convergence necessary for a bottom-up jet. Conversely, the SPH results exhibit a decoupled hydrodynamic response: the upper splash crown continues its unrestrained outward expansion, while a thick Worthington-like jet erupts forcefully from the deep cavity base. This fundamental divergence is a direct consequence of modeling the fluid domain without an explicit gas phase. At the free surface, the lack of inward aerodynamic pressure differentials prevents the cavity from sealing at the top [97]. Deep underwater, hydrostatic pressure drives the collapse of the cavity, squeezing the fluid radially inward against the impinging sphere and the impenetrable granular boundary. As this inward-flowing fluid violently converges at the central axis, the absence of a sealed, pressurized air buffer above dictates that the concentrated kinetic energy must be redirected entirely upward. The open cavity thus serves as the path of least resistance for pressure relief, artificially inducing the pronounced deep jet [98].

Furthermore, this late-stage morphological divergence is exacerbated by the surface properties of the projectile. The experiment utilizes a Teflon sphere [93], which is highly hydrophobic. In physical fluid dynamics, a hydrophobic surface strongly resists wetting, thereby promoting a wider, more persistent air-entraining cavity trailing the sphere. The current macroscopic SPH contact algorithm primarily exerts repulsive forces to prevent particle penetration, lacking the explicit micromechanical thermodynamic models required to capture contact angles and dynamic wetting transitions. Consequently, the implicit numerical treatment of the solid–fluid interface alters the cavity pinch-off timing and the subsequent jet dynamics. Nevertheless, since these deviations are strictly confined to the free-surface aerodynamics and cavity sealing mechanisms, they have a negligible influence on the primary focus of this study: the highly confined, fluid-driven granular cratering and structural penetration beneath the surface.

To quantitatively validate the numerical framework, the final penetration depth of the projectile is evaluated against the experimental data across a wide range of initial release heights, spanning from $h_0 = 20$ cm to 120 cm. As presented in Fig. 36, the experimental results are plotted as the mean of 10 independent trials, with the shaded error bands denoting the standard deviation, encapsulating the inherent physical uncertainties and statistical variations of the physical granular bed. Overall, the SPH-predicted penetration depths exhibit a satisfactory agreement with the experimental trend. The solver successfully captures the nonlinear positive correlation between the crater depth and the impact momentum (governed by h_0). Although minor deviations are observed at certain intermediate heights, potentially due to the idealized macroscopic continuum representation of discrete and stochastic granular interlocking mechanisms, the overall trend confirms the robustness and quantitative accuracy of the proposed multiphase SPH formulation in predicting extreme fluid–granular-structure interactions.

6. Application

6.1. Rainfall-induced bouldery debris flow on natural terrain

To demonstrate the robustness and scalability of the proposed multiphase SPH framework, a large-scale, 3D boundary value problem is simulated. This application models the initiation of a bouldery debris flow on a complex natural terrain triggered by rainfall infiltration, and its subsequent impact against a rigid slit dam. This scenario encapsulates the full sequence of a geotechnical disaster: from localized hydrological triggering and multiphase fluidization to violent fluid–structure–soil interactions.

The geometric configuration of the computational model is established based on a digitized 3D natural mountain terrain, imported via an STL (Stereolithography) surface boundary, as depicted in Fig. 37. An initial soil–boulder mixture deposit is situated

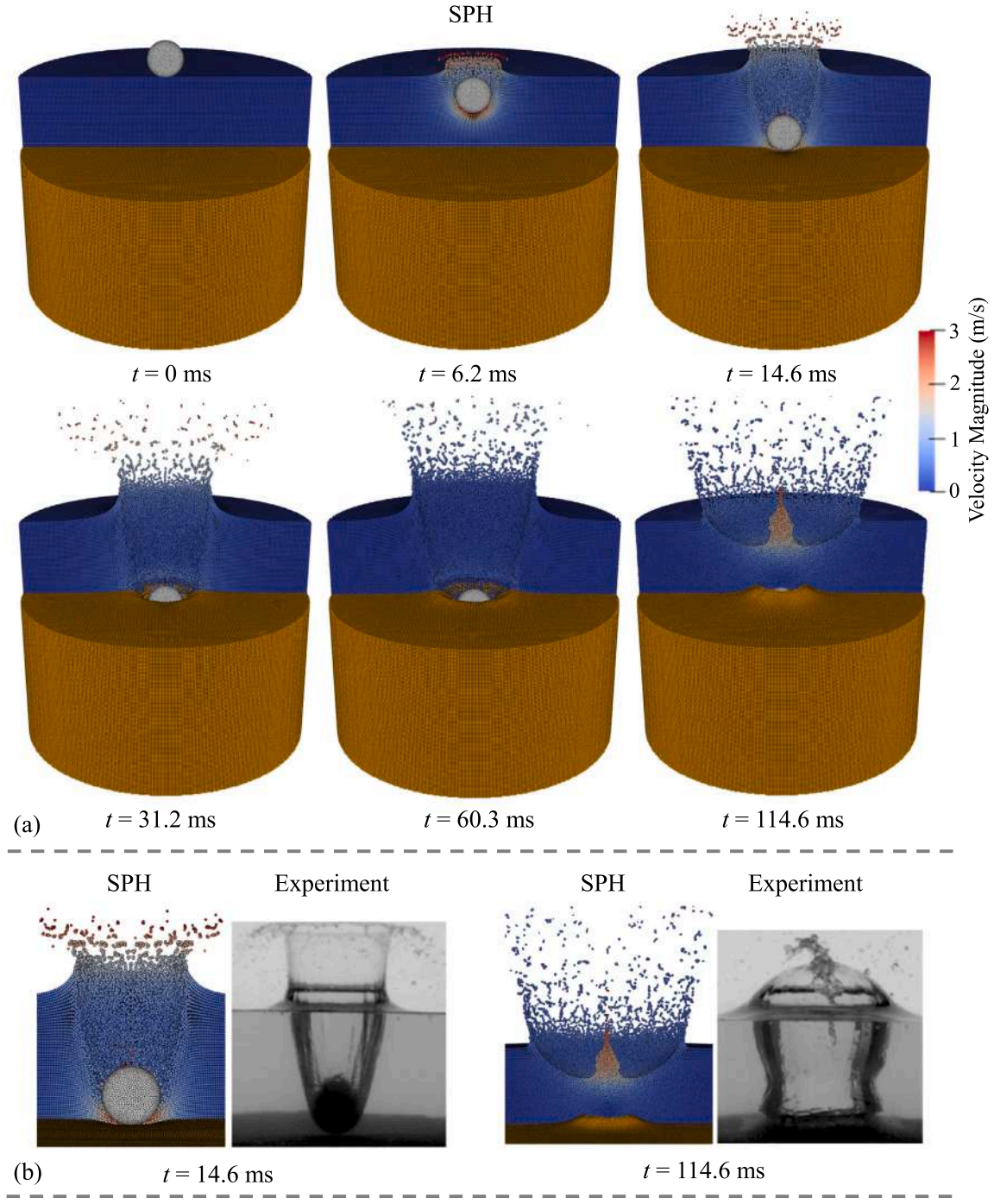

Fig. 35. Sphere impacting a submerged granular bed: (a) multiphase flow dynamics and crater morphology at selected instants, and (b) comparison of the macroscopic fluid distribution against experimental snapshots. To clearly visualize the internal flow dynamics, only a halved section of the water phase is shown. $h_0 = 1$ m.

on the upper reaches of the slope. This mixture is modeled as a binary granular system comprising a continuous fine-grained soil matrix and discrete rigid boulders. To simulate a rainfall event, a virtual “rain cloud” is positioned directly above the initial deposit, with a water inlet established at its base. Water particles are continuously emitted from this inlet at a steady velocity of (0, 0, −2) m/s, thereafter infiltrating the porous soil matrix.

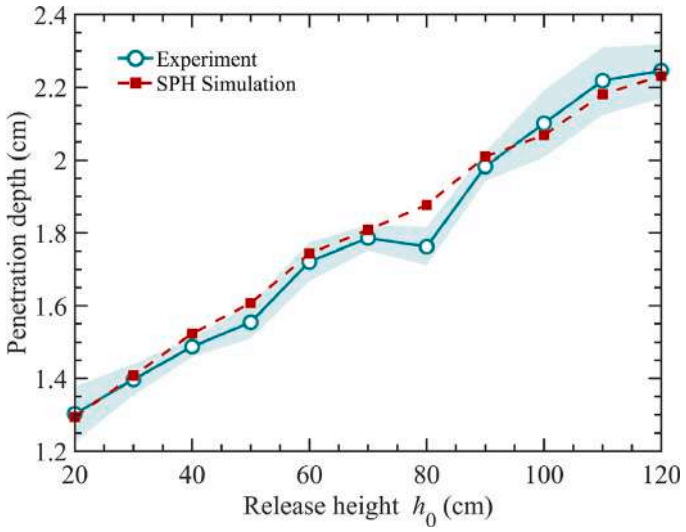

Fig. 36. Sphere impacting a submerged granular bed: comparison of the experimental [93] and SPH-predicted penetration depths as a function of the initial release height h_0. The experimental data points represent the mean values obtained from 10 independent trials, with the shaded error bands indicating the corresponding standard deviation.

Table 2
Material parameters for the multiphase bouldery debris flow simulation.

Parameter	Soil	Boulders	Water
Intrinsic density, ρ (kg/m^3)	2650	2650	1000
Young's modulus, E (MPa)	5.0	20.0	–
Poisson's ratio, ν	0.3	0.2	–
Initial volume fraction of soil, n^s	0.64	–	–
Internal friction angle, ϕ (°)	30.0	–	–
Initial cohesion, c_{ini} (kPa)	20.0	–	–
Saturated cohesion, c_{sat} (kPa)	0.0	–	–
Characteristic length, D_c (mm)	0.5	–	–
Dynamic viscosity, μ_f (Pa s)	–	–	1.0×10^{-3}

Further downstream along the main drainage channel, a rigid slit dam is installed to intercept the mobilized debris flow. The dam comprises a row of discrete vertical columns. The distance between the centers of two adjacent columns is set at 2 m, with each column measuring 1 m in both length and width. Based on the study by Ng et al. [99], such dam heights are strategically set within the range of $0.75\sim1.5h_f$, where h_f denotes the peak upstream approach flow depth. To accommodate the highly irregular natural topography, the absolute elevation of the slit dam's crest is maintained at a uniform horizontal level. Consequently, the effective height of the barrier varies between 10 m and 15.5 m relative to the local terrain.

The soil matrix is modeled to represent Completely Decomposed Granite (CDG), a broadly graded residual soil widely distributed in mountainous regions such as Hong Kong. Based on established geotechnical properties of CDG [100,101], the characteristic length of the soil matrix is set to $D_c = 0.5$ mm, representing the typical mean grain size (d_{50}) of the fine fraction. To accurately capture the rainfall-induced triggering mechanism, a saturation-dependent cohesion model is employed. The CDG matrix initially possesses an apparent cohesion of $c_{\text{ini}} = 20$ kPa, which maintains the static equilibrium of the slope prior to rainfall. As water infiltrates and the local degree of saturation (S_r) increases, this apparent cohesion linearly degrades following the relationship [18]:

$$c = c_{\text{sat}} + (1 - S_r)(c_{\text{ini}} - c_{\text{sat}}), \tag{108}$$

where $c_{\text{sat}} = 0$ kPa denotes the residual cohesion at full saturation. The introduction of non-zero cohesion allows the granular material to endure tension, which frequently triggers tensile instability. The original UTVF of Ref. [26] is applied to the cohesive soil phase to mitigate tensile instability, whereas the porosity-consistent water-phase extension introduced in Section 3.4 is applied to regularize the water distribution. The physical and mechanical parameters for the water, soil, and boulder phases are summarized in Table 2. The initial particle spacing is set to $dp^s = dp^w = dp^{rs} = 0.25$ m.

Fig. 38 presents a sequence of snapshots illustrating the temporal evolution of the debris flow. Initially at $t = 2.5$ s (Fig. 38a), the rainfall has not yet reached the deposit, leaving the soil–boulder mixture completely stable on the steep terrain. By $t = 12.5$ s (Fig. 38b), the precipitation reaches the deposit and gradually infiltrates. The left-side inset of Fig. 38b provides a water-only side view, clearly demonstrating the generation and steady accumulation of pore-water pressure. As the internal pore-water pressure rises (Fig. 38c), the apparent cohesion diminishes, causing the deposit to begin sliding downwards under the influence of the infiltrating water.

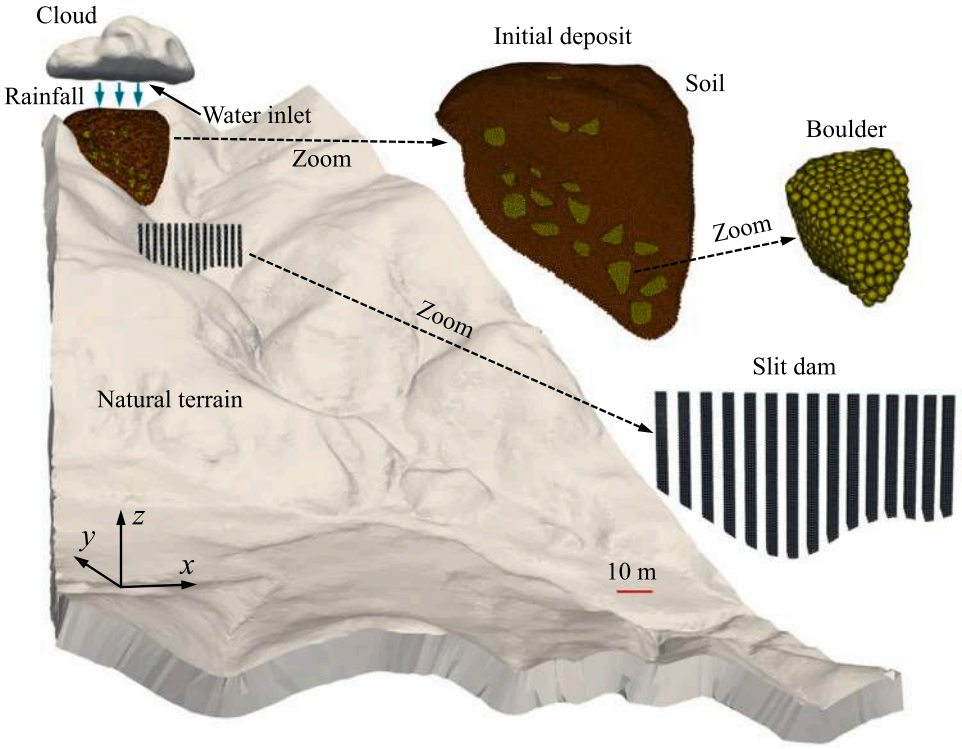

Fig. 37. Rainfall-induced bouldery debris flow: model setup.

Once the soil matrix yields, the mixture rapidly fluidizes. The discrete boulders, initially embedded within the soil, are entrained by the remolded soil–water slurry. Driven by gravity and the intense drag forces exerted by the interstitial water, the bouldery debris flow accelerates down the tortuous natural channel.

At t = 17.5 s (Fig. 38d), the mobilized deposit reaches the slit dams and begins to accumulate in front of the structures (Fig. 38e). Driven by the progressive accumulation and continuous rainfall, the soil and water gradually seep through the gaps of the slit dams (Fig. 38e–f). During this filtering stage, only the soil and water bypass the barrier, while the boulders are completely intercepted. As the upstream deposition intensifies, the debris volume eventually exceeds the dam height, triggering an overtopping event at the crest (Fig. 38g), during which a small fraction of boulders also overtop the barrier. Subsequently, sustained by the continuous rainfall, the soil–water slurry maintains its runout trajectory down to the bottom of the slope at t = 30.0 s (Fig. 38h). The zoomed-in view on the right side of Fig. 38h isolates the spatial distribution of the boulders, revealing that while the vast majority are successfully arrested behind the dams, a few manage to bypass the barrier laterally owing to the continuous scouring action of the fluid phases. As the debris flow reaches the downstream section, it violently impacts the rigid slit dam. The unique structural geometry of the slit dam allows the fine-grained soil–water slurry to pass through the vertical gaps, effectively draining the fluid phase and reducing the hydrodynamic pressure. Conversely, the massive boulders, possessing a diameter larger than the slit spacing, are successfully intercepted and arrested by the barrier. This "filter-and-block" mechanism highlights the distinct coupling interactions handled by the SPH solver: water–soil seepage, soil–structure flow, and boulder–structure rigid body collisions.

To quantitatively evaluate the system's macroscopic behavior, the temporal evolution of the global kinetic energy for each phase is plotted in Fig. 39. The evolutionary process can be distinctly categorized into three stages: infiltration, acceleration, and impact & runout, strictly corresponding to the kinematic observations in Fig. 38. During the initial infiltration stage, the kinetic energy of all phases remains nearly constant at zero as the deposit maintains its stability. In the subsequent acceleration stage, a synchronized surge in kinetic energy signifies the catastrophic failure of the slope and the onset of the debris flow. At approximately t = 18.7 s, the kinetic energy of the soil and boulders reaches a primary local maximum (impact peak) as the mixture violently strikes the slit dams. Following this initial impact, the kinetic energy begins to decline due to intense structural interception. Notably, the local maximum of the water's kinetic energy exhibits a slight temporal lag compared to that of the soil. This delay is physically reasonable, as the water, acting as the interstitial fluid and trailing from the continuous rainfall, maintains its forward momentum slightly longer before fully decelerating against the intercepted soil mass and the rigid barrier. During the impact & runout stage, the soil and water continuously accumulate behind the dams. As the kinetic energy drops to a certain threshold, significant seepage and dam overtopping occur. The soil and water that bypass the barrier accelerate once again down the steep downstream topography, leading to a continuous and substantial resurgence in kinetic energy that eventually surpasses the primary impact peak. Conversely, the kinetic energy of the boulders drops abruptly post-impact and remains relatively stable, exhibiting minor subsequent growth when a limited number of boulders either overtop the crest or are scoured around the lateral sides of the dams.

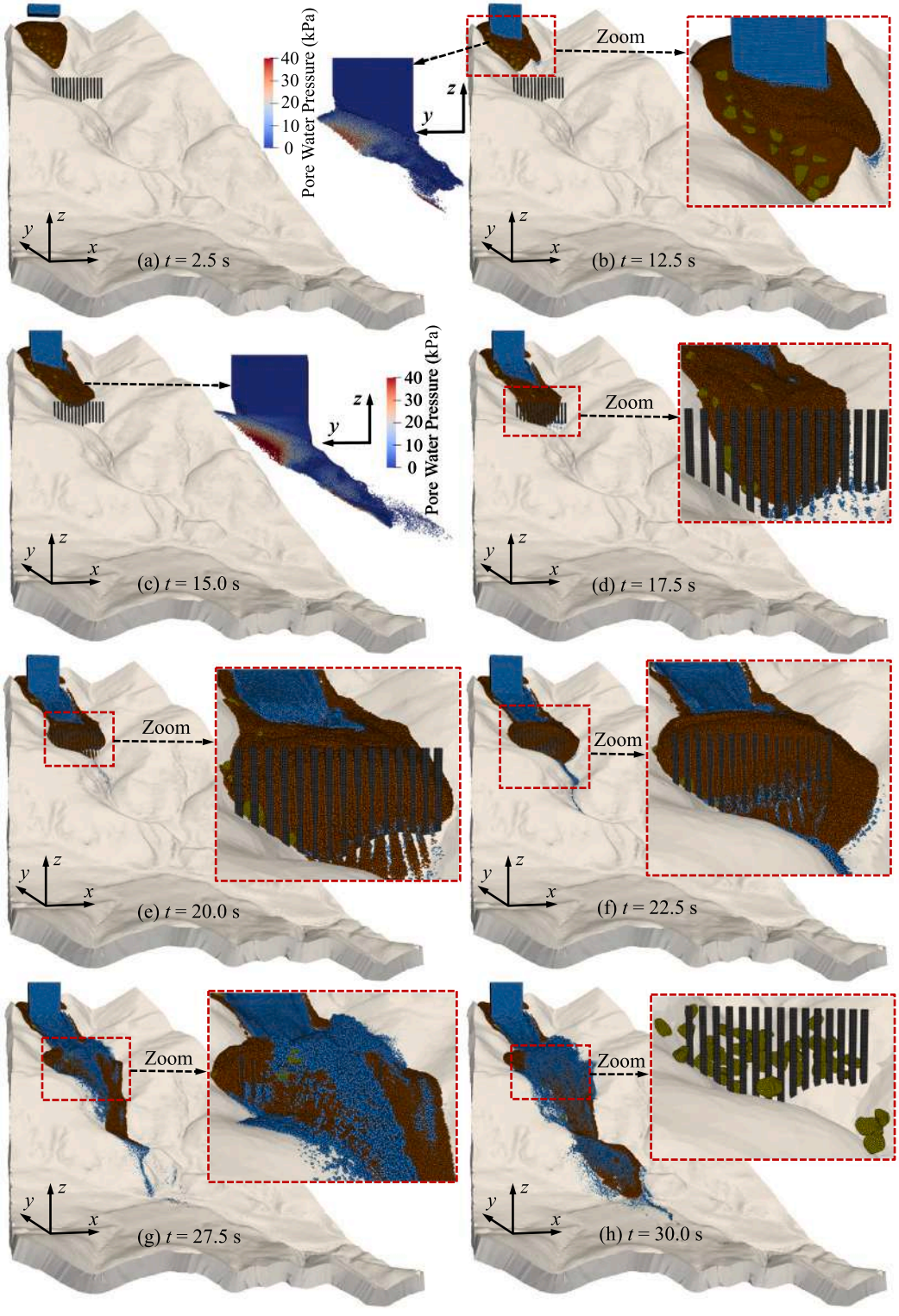

Fig. 38. Rainfall-induced bouldery debris flow: sequential simulation snapshots from $t = 2.5$ s to 30.0 s. The sequence illustrates the complete disaster mechanism: initial rainfall infiltration, subsequent fluidization of the deposit, rapid acceleration down the natural channel, and the final fluid–structure interactions characterized by structural impact, slurry discharging through the slits, and eventual dam overtopping.

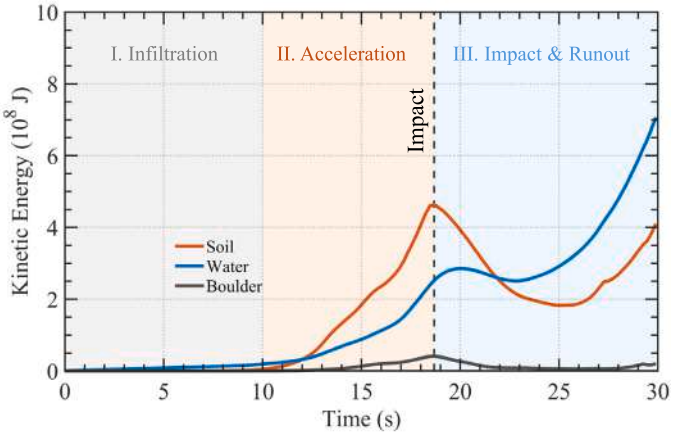

Fig. 39. Rainfall-induced bouldery debris flow: time histories of the global kinetic energy for the individual phases (soil, water, and boulders) throughout the simulation process.

Table 3
Physical and mechanical parameters for the 3D wave–seabed–cobble–mangrove interaction model.

Parameter	Soil	Cobbles	Water
Intrinsic density, ρ (kg/m^3)	2650	2650	1000
Young's modulus, E (MPa)	5.0	20.0	–
Poisson's ratio, ν	0.3	0.25	–
Initial volume fraction of soil, n^s	0.64	–	–
Internal friction angle, ϕ (°)	33.0	–	–
Cohesion, c (kPa)	0.0	–	–
Characteristic length, D_c (mm)	0.5	–	–
Dynamic viscosity, μ_f (Pa s)	–	–	1.0×10^{-3}

6.2. Wave–seabed–cobble–mangrove interaction in a coastal environment

To demonstrate the full capability of the proposed multiphase SPH framework in handling highly complex, large-scale engineering and ecological scenarios, the 3D wave–seabed–cobble–mangrove interaction in a coastal environment is investigated. Mangrove forests serve as vital natural barriers for coastal protection, dissipating wave energy and mitigating seabed erosion. Simulating this phenomenon requires a robust coupling mechanism that can simultaneously resolve the fluid dynamics of the breaking waves, the elastoplastic response of the seabed soil, the collision of discrete cobbles, and the hydrodynamic interaction with the rigid mangrove roots.

The overall model setup is illustrated in Fig. 40. As depicted in the 2D side view (Fig. 40a), the 3D computational domain is established to represent a typical coastal transect with specific geometric dimensions and initial water depth. Three velocity probes (P1, P2, and P3) are strategically deployed along the longitudinal mid-plane of the domain, positioned 0.2 m below the initial free surface, to monitor the transient flow velocity. At the bottom of the domain, a multi-stage seabed soil bed is constructed, featuring a deep-water flat base, a transition slope, a mangrove-planting zone, and a rear wave-absorbing beach. Fig. 40b presents the 3D schematic of the computational domain. A highly complex 3D mangrove tree model is embedded into the soil bed. In this study, the mangrove tree is fixed in place and considered to undergo negligible macroscopic deformation owing to its robust root anchorage system. Furthermore, to capture the dynamic response of discrete bed loads under severe wave actions, a group of 30 independent cobbles, modeled as elastic materials with random geometric perturbations, are distributed around the mangrove tree within a predefined exclusion radius to avoid initial geometrical intersections with the roots. To generate the incident waves, a fully Lagrangian piston-type wave maker is implemented at the offshore boundary of the domain [102,103]. The target incident wave parameters are set to a wave height of $H = 0.32$ m and a period of $T = 2.0$ s.

The physical and mechanical parameters of the active phases are summarized in Table 3. For the seabed soil, an internal friction angle of $\phi = 33°$ with zero cohesion and a characteristic particle size of $D_c = 0.5$ mm are adopted to represent the typical behavior of medium-dense, saturated marine quartz sand.

Fig. 41 presents a sequence of simulation snapshots illustrating the highly dynamic water–soil–cobble–mangrove interaction process. The figure is organized into two columns: Fig. 41a displays the velocity profile of the water phase, while Fig. 41b renders the water transparent to explicitly reveal the morphodynamic evolution of the seabed soil. As the incident waves propagate over the transition slope, distinct wave deformation, breaking, and significant energy attenuation are vividly captured around the complex

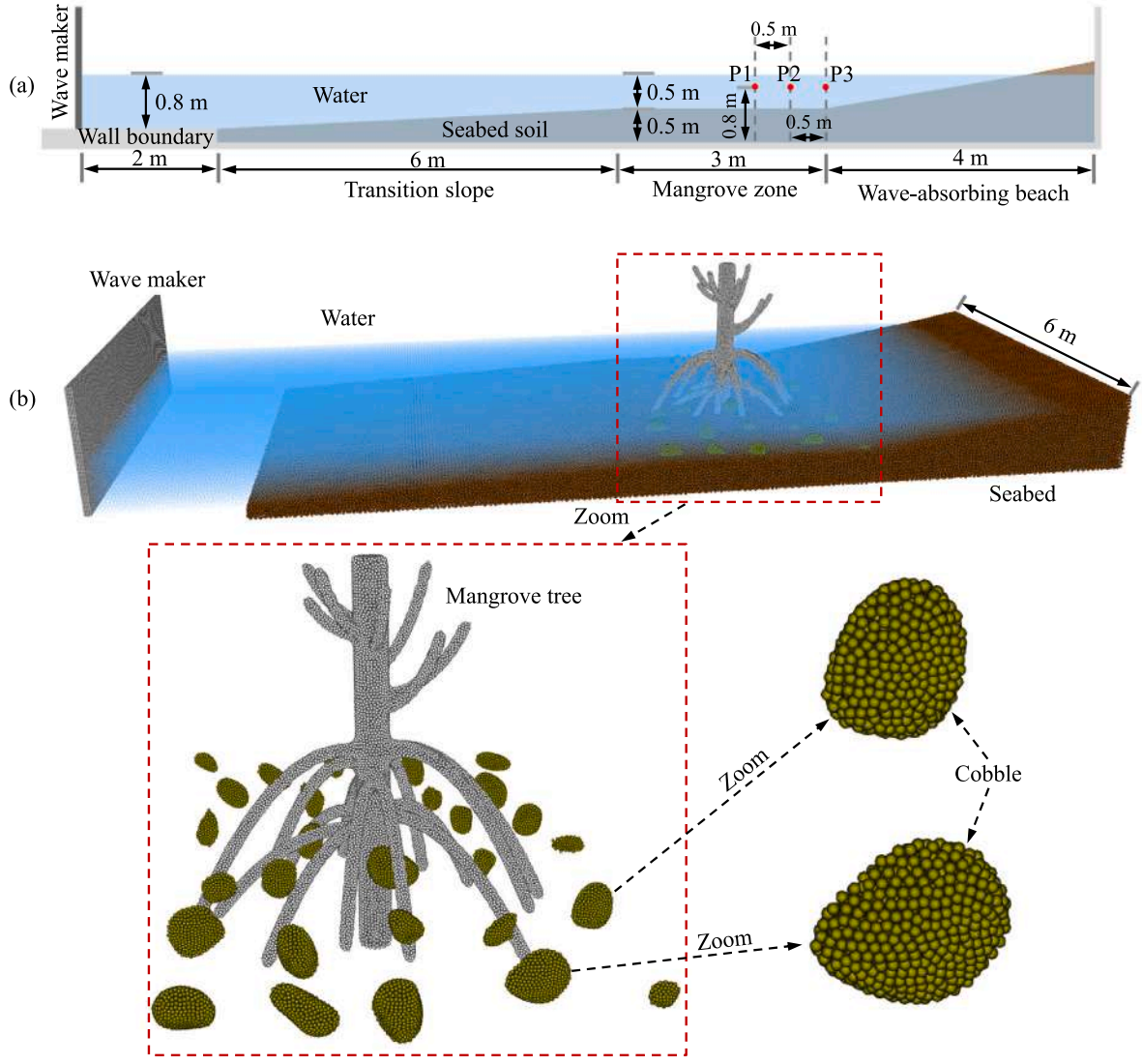

Fig. 40. Wave–seabed–cobble–mangrove interaction: configuration of the numerical model setup, comprising (a) a 2D side view with geometric dimensions and velocity probe locations (P1–P3), and (b) a 3D schematic view with zoomed-in illustrations of the discrete cobbles and the complex mangrove roots.

root system of the mangrove tree, corresponding to a visually observable decrease in wave height. The intense hydrodynamic forces concurrently drive morphological changes in the soil phase. Notably, as observed in Fig. 41b near the upstream fluid–soil interface, the cyclic wave shear induces localized seabed erosion. Governed by the two-layer SPH formulation, the superficial soil particles are mobilized and transported leftward (offshore) along the bottom boundary into the pure water region, macroscopically reproducing the wave-induced scour and bedload transport mechanisms. Furthermore, as the residual waves propagate to the far right of the domain, they impact the emergent wave-absorbing beach. The fluid undergoes runup along the exposed soil bed and rapidly dissipates, demonstrating the effectiveness of the sloping topography in neutralizing the remaining wave energy.

To quantify the influence of the mangrove root system on the local flow response, Fig. 42 compares the velocity histories recorded at probes P1–P3 for the cases with and without the mangrove tree. During the initial wave arrivals, local velocity amplification is observed at some probes because the roots constrict the available flow passages. At later stages, the case with the mangrove tree generally exhibits reduced velocity amplitudes and delayed velocity peaks, indicating that the modeled root system modifies and attenuates the local wave-induced flow. This comparison is intended to illustrate the coupled response represented by the numerical framework rather than to provide a quantitative validation of mangrove-induced wave attenuation.

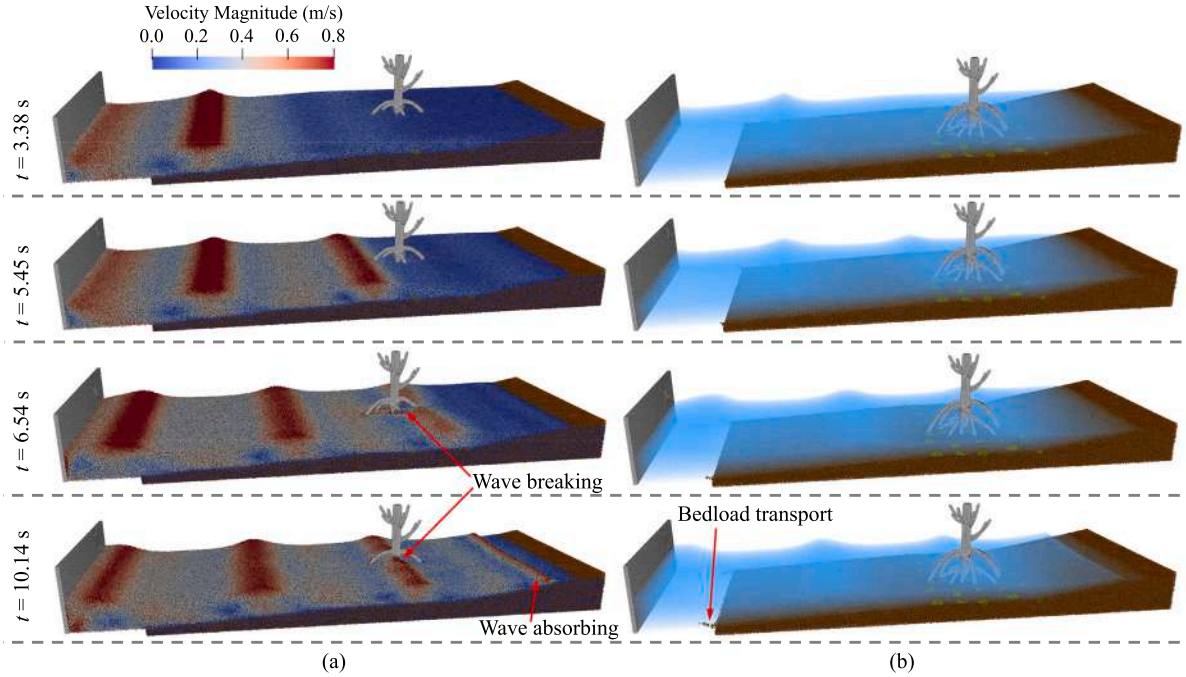

Fig. 41. Wave–seabed–cobble–mangrove interaction: sequential simulation snapshots illustrating the spatiotemporal evolution of wave shoaling and breaking. (a) The velocity profile of the water phase. (b) The morphological evolution of the seabed soil, with the water phase rendered transparent to highlight wave-induced bedload transport.

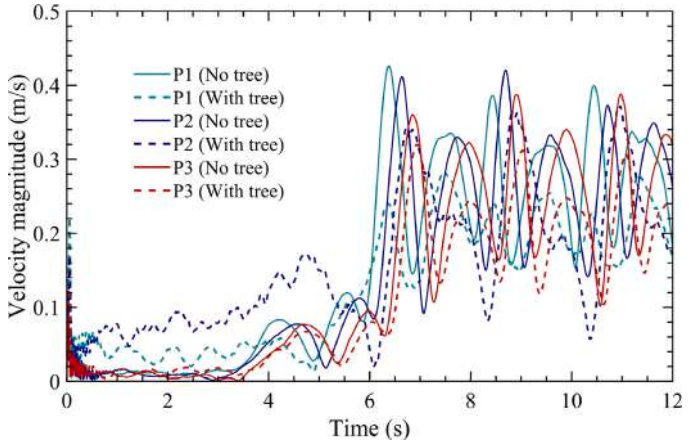

Fig. 42. Wave–seabed–cobble–mangrove interaction: time histories of the velocity recorded by the three probes (P1, P2, and P3) throughout the simulation process, comparing the hydrodynamic responses with and without the mangrove tree.

7. Conclusions and outlook

This study assembled and assessed a three-dimensional SPH framework for coupled soil–water–rock–structure dynamics, with particular attention to a porosity-consistent representation of the water phase. The principal findings are summarized as follows.

1. Porosity-consistent water representation. The soil and water phases are represented by overlapping particle sets within two-phase mixture theory. The water phase employs an intrinsic-density formulation in which the representative mixture volume associated with a water particle is evaluated as $V_i^w = \frac{m_i^w}{n_i^w \rho_i^w}$. Consequently, the representative volume varies as a water particle moves between clear-fluid and porous regions, whereas the physical water volume represented by the particle is

$n_i^w V_i^w = m_i^w / \rho_i^w$. The collapse-into-porous-media benchmark and the U-tube test support the fluid-volume consistency and seepage accuracy of this formulation.

2. Equal-mass porosity-consistent initialization. A level-set-guided particle-relaxation procedure was introduced for configurations in which soil and water overlap initially. Unlike a variable-mass, uniform-geometric-volume initialization, the procedure retains a common water-particle mass and adjusts the initial number density, spacing, and representative volume according to the prescribed porosity. This treatment provides porosity-consistent initial water distributions for saturated beds, submerged granular deposits, and related applications.
3. Porosity-consistent particle regularization. A porosity-consistent extension of the unified transport-velocity formulation was introduced for the water phase. The target particle volume is evaluated from the current water volume fraction reconstructed from the soil skeleton, and the artificial transport displacement is projected near sharp porosity gradients. The treatment regularizes the water-particle distribution without driving porous-region particles toward the clear-fluid spacing.
4. Integrated multiphysics capability. The updated-Lagrangian soil and water phases were coupled with total-Lagrangian Neo-Hookean rocks and structures. The benchmark calculations cover soil–water seepage, soil–solid contact, fluid–structure interaction, solid–solid contact, and three-phase granular–water–solid interaction. The two three-dimensional applications further illustrate the ability of the framework to handle large deformation, free surfaces, moving porous interfaces, and multiple solid inclusions within one solver.

The low-dissipation Riemann solvers, UL/TL coupling, spatial multi-resolution, dual-criteria time stepping, and phase-decoupled subcycling used in the calculations are previously established components incorporated to support numerical robustness and computational tractability.

The present formulation is limited to clear-water regions and locally saturated soil–water coexistence. The air phase, matric suction, soil–water retention, capillarity, wetting effects, and surface tension are not included. In addition, the soil skeleton is represented as a continuum and therefore does not explicitly resolve grain crushing, segregation, or individual grain contacts. Future work should address these limitations and provide broader quantitative validation of the initialization and transport-regularization procedures under evolving and strongly heterogeneous porosity fields.

CRediT authorship contribution statement

Shuaihao Zhang: Writing – review & editing, Writing – original draft, Visualization, Validation, Software, Methodology, Investigation, Formal analysis, Conceptualization. **Jidong Zhao:** Writing – review & editing, Supervision, Resources, Funding acquisition, Conceptualization. **Ruofeng Feng:** Writing – review & editing, Formal analysis. **Honghu Zhu:** Writing – review & editing, Investigation.

Declaration of competing interest

The authors declare that they have no known competing financial interests or personal relationships that could have appeared to influence the work reported in this paper.

Acknowledgments

This research was financially supported by the National Natural Science Foundation of China (Key Project 52439001), the Research Grants Council of Hong Kong (GRF 16203123, 16208224, 16214525, CRF C7085-24G, RIF R6008-24, and TRS T22-607/24 N), and the State Key Laboratory of Climate Resilience for Coastal Cities (SKLCRCC) (ITC-SKLCRCC26EG01). The opinions, findings, conclusions, or recommendations expressed in this material are those of the authors and do not necessarily reflect the views of the funding agencies.

Data availability

Data will be made available on request.

References

[1] J. Aaron, J. Langham, R. Spielmann, J. Hirschberg, B. McArdell, S. Boss, C.G. Johnson, J.M. Gray, Detailed observations reveal the genesis and dynamics of destructive debris-flow surges, Commun. Earth Environ. 6 (1) (2025) 556.
[2] D. Song, C. Choi, C. Ng, G.G. Zhou, J. Kwan, H. Sze, Y. Zheng, Load-attenuation mechanisms of flexible barrier subjected to bouldery debris flow impact, Landslides 16 (12) (2019) 2321–2334.
[3] S. Temmerman, P. Meire, T.J. Bouma, P.M. Herman, T. Ysebaert, H.J. De Vriend, Ecosystem-based coastal defence in the face of global change, Nature 504 (7478) (2013) 79–83.
[4] Z. Hu, S. Temmerman, Q. Zhu, X. Wang, J. Wu, T. Xu, K. Schoutens, T. Suzuki, Z. Yang, T.J. Bouma, Predicting nature-based coastal protection by mangroves under extreme waves, Proc. Natl. Acad. Sci. 122 (12) (2025) e2410883122.
[5] O.C. Zienkiewicz, A.H.C. Chan, M. Pastor, B.A. Schrefler, T. Shiomi, Computational Geomechanics with Special Reference to Earthquake Engineering, first ed., John Wiley & Sons, Chichester, UK, 1999.

[6] T.J. Hughes, W.K. Liu, T.K. Zimmermann, Lagrangian–Eulerian finite element formulation for incompressible viscous flows, Comput. Methods Appl. Mech. Engrg. 29 (3) (1981) 329–349.
[7] C.W. Hirt, B.D. Nichols, Volume of fluid (VOF) method for the dynamics of free boundaries, J. Comput. Phys. 39 (1) (1981) 201–225.
[8] D.J. Benson, Computational methods in Lagrangian and Eulerian hydrocodes, Comput. Methods Appl. Mech. Engrg. 99 (2–3) (1992) 235–394.
[9] G. Qiu, S. Henke, J. Grabe, Application of a coupled Eulerian–Lagrangian approach on geomechanical problems involving large deformations, Comput. Geotech. 38 (1) (2011) 30–39.
[10] T. Belytschko, W.K. Liu, B. Moran, K. Elkhodary, Nonlinear Finite Elements for Continua and Structures, John Wiley & Sons, 2014.
[11] D. Sulsky, Z. Chen, H.L. Schreyer, A particle method for history-dependent materials, Comput. Methods Appl. Mech. Engrg. 118 (1–2) (1994) 179–196.
[12] L.B. Lucy, A numerical approach to the testing of the fission hypothesis, Astron. J. 82 (1977) 1013–1024.
[13] R.A. Gingold, J.J. Monaghan, Smoothed particle hydrodynamics: theory and application to non-spherical stars, Mon. Not. R. Astron. Soc. 181 (3) (1977) 375–389.
[14] G.R. Liu, Smoothed particle hydrodynamics (SPH): an overview and recent developments, Arch. Comput. Methods Eng. 17 (1) (2010) 25–76.
[15] H.H. Bui, G.D. Nguyen, Smoothed particle hydrodynamics (SPH) and its applications in geomechanics: From solid fracture to granular behaviour and multiphase flows in porous media, Comput. Geotech. 138 (2021) 104315.
[16] S. Zhang, Stability-Enhanced Smoothed Particle Hydrodynamics for Geomaterials: Methods and Applications (Ph.D. thesis), The University of Hong Kong, Pokfulam, Hong Kong SAR, 2025.
[17] H.H. Bui, R. Fukagawa, K. Sako, S. Ohno, Lagrangian meshfree particles method (SPH) for large deformation and failure flows of geomaterial using elastic–plastic soil constitutive model, Int. J. Numer. Anal. Methods Geomech. 32 (12) (2008) 1537–1570.
[18] H.H. Bui, G.D. Nguyen, A coupled fluid-solid SPH approach to modelling flow through deformable porous media, Int. J. Solids Struct. 125 (2017) 244–264.
[19] C. Peng, G. Xu, W. Wu, H.-s. Yu, C. Wang, Multiphase SPH modeling of free surface flow in porous media with variable porosity, Comput. Geotech. 81 (2017) 239–248.
[20] R. Feng, J. Zhao, G. Fourtakas, B.D. Rogers, GeoDualSPHysics: a high-performance SPH solver for large deformation modelling of geomaterials with two-way coupling to multi-body systems, Comput. Phys. Comm. 320 (2026) 109965.
[21] S. Zhang, S.D. Lourenço, X. Hu, Multiphase SPH for surface tension: Resolving zero-surface-energy modes and achieving high Reynolds number simulations, Comput. Methods Appl. Mech. Engrg. 444 (2025) 118147.
[22] Y. Lian, H.H. Bui, G.D. Nguyen, S. Zhao, A. Haque, A computationally efficient SPH framework for unsaturated soils and its application to predicting the entire rainfall-induced slope failure process, Géotechnique 74 (8) (2024) 787–805.
[23] R. Feng, J. Zhao, J. Chen, A 3D multiphase SPH framework for modelling soil-water interaction in rainfall-landslide-tsunami cascades, Eng. Geol. 361 (2026) 108495.
[24] J.J. Monaghan, R.A. Gingold, Shock simulation by the particle method SPH, J. Comput. Phys. 52 (2) (1983) 374–389.
[25] C. Zhang, X. Hu, N.A. Adams, A weakly compressible SPH method based on a low-dissipation Riemann solver, J. Comput. Phys. 335 (2017) 605–620.
[26] S. Zhang, F. Wang, X. Hu, S.D. Lourenço, A unified transport-velocity formulation for SPH simulation of cohesive granular materials, Comput. Geotech. 181 (2025) 107139.
[27] S. Zhang, C. Zhang, X. Hu, S.D. Lourenço, A Riemann-based SPH method for modelling large deformation of granular materials, Comput. Geotech. 167 (2024) 106052.
[28] M.A. Hafeez, R. Vacondio, A. English, G. Fourtakas, B.D. Rogers, A low dissipation formulation for weakly compressible Riemann-based SPH schemes, Comput. Part. Mech. 14 (2026) 193–210.
[29] M. Asai, S. Fujioka, Y. Saeki, D.S. Morikawa, K. Tsuji, A class of second-derivatives in the smoothed particle hydrodynamics with 2nd-order accuracy and its application to incompressible flow simulations, Comput. Methods Appl. Mech. Engrg. 415 (2023) 116203.
[30] T. Matsunaga, S. Koshizuka, Stabilized LSMPS method for complex free-surface flow simulation, Comput. Methods Appl. Mech. Engrg. 389 (2022) 114416.
[31] K. Shobuzako, S. Yoshida, Y. Kawada, R. Nakashima, S. Fujioka, M. Asai, A generalized smoothed particle hydrodynamics method based on the moving least squares method and its discretization error estimation, Results Appl. Math. 26 (2025) 100594.
[32] R. Feng, G. Fourtakas, B.D. Rogers, D. Lombardi, A general smoothed particle hydrodynamics (SPH) formulation for coupled liquid flow and solid deformation in porous media, Comput. Methods Appl. Mech. Engrg. 419 (2024) 116581.
[33] S. Shao, Incompressible SPH flow model for wave interactions with porous media, Coast. Eng. 57 (3) (2010) 304–316.
[34] D.S. Morikawa, M. Asai, A phase-change approach to landslide simulations: Coupling finite strain elastoplastic TLSPH with non-Newtonian IISPH, Comput. Geotech. 148 (2022) 104815.
[35] H.H. Bui, K. Sako, R. Fukagawa, Numerical simulation of soil–water interaction using smoothed particle hydrodynamics (SPH) method, J. Terramechanics 44 (5) (2007) 339–346.
[36] C. Zhu, C. Peng, W. Wu, C. Wang, A multi-layer SPH method for generic water–soil dynamic coupling problems. Part I: Revisit, theory, and validation, Comput. Methods Appl. Mech. Engrg. 396 (2022) 115106.
[37] M. Jandaghian, A. Pilechi, S. Baker, A weakly-compressible SPH-porous media model to simulate wave–breakwater interactions, Coast. Eng. 201 (2025) 104811.
[38] C. De Sousa, M. Lallemand, G. Oger, J. Michel, D. Le Touzé, D. Violeau, SPH modelling of water flow inside a fixed and undeformable porous medium using a Riemann based formulation, J. Comput. Phys. 549 (2026) 114588.
[39] K. Tsuji, S. Fujioka, D.S. Morikawa, M. Asai, A reliable SPH (2) formulation for Darcy–Forchheimer–Brinkman equation using a density-based particle shifting in the ALE description, Comput. Part. Mech. 12 (2) (2025) 1045–1073.
[40] Y. Yu, Y. Zhu, C. Zhang, O.J. Haidn, X. Hu, Level-set based pre-processing techniques for particle methods, Comput. Phys. Comm. 289 (2023) 108744.
[41] C. Zhao, Y. Yu, O.J. Haidn, X. Hu, Physics-driven complex relaxation for multi-body systems of SPH method, Comput. Phys. Comm. 313 (2025) 109615.
[42] C. Zhang, M. Rezavand, X. Hu, A multi-resolution SPH method for fluid-structure interactions, J. Comput. Phys. 429 (2021) 110028.
[43] S. Zhang, D. Wu, X. Hu, C.E. Choi, S.D. Lourenço, An efficient SPH framework for modeling binary granular mixtures and implications for granular flows, Int. J. Numer. Anal. Methods Geomech. 49 (3) (2025) 815–838.
[44] C. Zhang, M. Rezavand, X. Hu, Dual-criteria time stepping for weakly compressible smoothed particle hydrodynamics, J. Comput. Phys. 404 (2020) 109135.
[45] A.J. Crespo, J.M. Domínguez, B.D. Rogers, M. Gómez-Gesteira, S. Longshaw, R. Canelas, R. Vacondio, A. Barreiro, O. García-Feal, DualSPHysics: Open-source parallel CFD solver based on smoothed particle hydrodynamics (SPH), Comput. Phys. Comm. 187 (2015) 204–216.
[46] J.M. Domínguez, G. Fourtakas, C. Altomare, R.B. Canelas, A. Tafuni, O. García-Feal, I. Martínez-Estévez, A. Mokos, R. Vacondio, A.J. Crespo, et al., DualSPHysics: from fluid dynamics to multiphysics problems, Comput. Part. Mech. 9 (5) (2022) 867–895.
[47] C. Zhang, M. Rezavand, Y. Zhu, Y. Yu, D. Wu, W. Zhang, J. Wang, X. Hu, SPHinXsys: an open-source multi-physics and multi-resolution library based on smoothed particle hydrodynamics, Comput. Phys. Comm. 267 (2021) 108066.
[48] M.A. Biot, Theory of propagation of elastic waves in a fluid-saturated porous solid. II. Higher frequency range, J. Acoust. Soc. Am. 28 (2) (1956) 179–191.
[49] O.C. Zienkiewicz, A. Chan, M. Pastor, D. Paul, T. Shiomi, Static and dynamic behaviour of soils: a rational approach to quantitative solutions. I. Fully saturated problems, Proc. R. Soc. A 429 (1877) (1990) 285–309.

[50] O. Zienkiewicz, T. Shiomi, Dynamic behaviour of saturated porous media; the generalized Biot formulation and its numerical solution, Int. J. Numer. Anal. Methods Geomech. 8 (1) (1984) 71–96.
[51] D.C. Drucker, W. Prager, Soil mechanics and plastic analysis or limit design, Quart. Appl. Math. 10 (2) (1952) 157–165.
[52] R.I. Borja, Plasticity: Modeling & Computation, Springer, 2013.
[53] J.J. Monaghan, Simulating free surface flows with SPH, J. Comput. Phys. 110 (2) (1994) 399–406.
[54] J.P. Morris, P.J. Fox, Y. Zhu, Modeling low Reynolds number incompressible flows using SPH, J. Comput. Phys. 136 (1) (1997) 214–226.
[55] M.A. Biot, General theory of three-dimensional consolidation, J. Appl. Phys. 12 (2) (1941) 155–164.
[56] Y. Huang, W. Zhang, Z. Dai, Q. Xu, Numerical simulation of flow processes in liquefied soils using a soil–water-coupled smoothed particle hydrodynamics method, Nat. Hazards 69 (1) (2013) 809–827.
[57] C. Wang, Y. Wang, C. Peng, X. Meng, Smoothed particle hydrodynamics simulation of water-soil mixture flows, J. Hydraul. Eng. 142 (10) (2016) 04016032.
[58] S. Ergun, A.A. Orning, Fluid flow through randomly packed columns and fluidized beds, Ind. Eng. Chem. 41 (6) (1949) 1179–1184.
[59] R.W. Ogden, Non-linear Elastic Deformations, Courier Corporation, 1997.
[60] J.J. Monaghan, Smoothed particle hydrodynamics, Annu. Rev. Astron. Astrophys. 30 (1992) 543–574.
[61] J.J. Monaghan, Smoothed particle hydrodynamics, Rep. Progr. Phys. 68 (8) (2005) 1703.
[62] D. Wu, C. Zhang, X. Tang, X. Hu, An essentially non-hourglass formulation for total Lagrangian smoothed particle hydrodynamics, Comput. Methods Appl. Mech. Engrg. 407 (2023) 115915.
[63] P. Randles, L.D. Libersky, Smoothed particle hydrodynamics: some recent improvements and applications, Comput. Methods Appl. Mech. Engrg. 139 (1–4) (1996) 375–408.
[64] J. Bonet, S. Kulasegaram, A simplified approach to enhance the performance of smooth particle hydrodynamics methods, Appl. Math. Comput. 126 (2–3) (2002) 133–155.
[65] R. Vignjevic, J. Campbell, Review of development of the smooth particle hydrodynamics (SPH) method, in: Predictive Modeling of Dynamic Processes: A Tribute to Professor Klaus Thoma, Springer, 2009, pp. 367–396.
[66] S. Adami, X.Y. Hu, N.A. Adams, A generalized wall boundary condition for smoothed particle hydrodynamics, J. Comput. Phys. 231 (21) (2012) 7057–7075.
[67] D. Wu, S. Zhang, W. Kong, G. Ma, Y. Yu, X. Hu, A projection-based SPH framework for shell-related fluid coupling and contact interactions, Comput. Methods Appl. Mech. Engrg. 461 (2026) 119243.
[68] S.J. Lind, R. Xu, P.K. Stansby, B.D. Rogers, Incompressible smoothed particle hydrodynamics for free-surface flows: A generalised diffusion-based algorithm for stability and validations for impulsive flows and propagating waves, J. Comput. Phys. 231 (4) (2012) 1499–1523.
[69] P. Rastelli, R. Vacondio, J. Marongiu, G. Fourtakas, B.D. Rogers, Implicit iterative particle shifting for meshless numerical schemes using kernel basis functions, Comput. Methods Appl. Mech. Engrg. 393 (2022) 114716.
[70] P. Rastelli, R. Vacondio, J. Marongiu, An arbitrarily Lagrangian–Eulerian SPH scheme with implicit iterative particle shifting procedure, Comput. Methods Appl. Mech. Engrg. 414 (2023) 116159.
[71] S. Adami, X. Hu, N.A. Adams, A transport-velocity formulation for smoothed particle hydrodynamics, J. Comput. Phys. 241 (2013) 292–307.
[72] H. Wendland, Piecewise polynomial, positive definite and compactly supported radial functions of minimal degree, Adv. Comput. Math. 4 (1) (1995) 389–396.
[73] S.A. Rzadkiewicz, C. Mariotti, P. Heinrich, Numerical simulation of submarine landslides and their hydraulic effects, J. Waterw. Port Coast. Ocean. Eng. 123 (4) (1997) 149–157.
[74] T. Capone, A. Panizzo, J.J. Monaghan, SPH modelling of water waves generated by submarine landslides, J. Hydraul. Res. 48 (sup1) (2010) 80–84.
[75] G. Ma, J.T. Kirby, F. Shi, Numerical simulation of tsunami waves generated by deformable submarine landslides, Ocean. Model. 69 (2013) 146–165.
[76] Y. Fang, Q. Xu, J. Chen, A Riemann-based two-phase two-layer SPH method for simulating submarine landslide tsunamis, Comput. Geotech. 184 (2025) 107247.
[77] J. Uehara, M. Ambroso, R. Ojha, D.J. Durian, Low-speed impact craters in loose granular media, Phys. Rev. Lett. 90 (19) (2003) 194301.
[78] M. Ambroso, C. Santore, A. Abate, D.J. Durian, Penetration depth for shallow impact cratering, Phys. Rev. E 71 (5) (2005) 051305.
[79] W. Hu, M. Rakhsha, L. Yang, K. Kamrin, D. Negrut, Modeling granular material dynamics and its two-way coupling with moving solid bodies using a continuum representation and the SPH method, Comput. Methods Appl. Mech. Engrg. 385 (2021) 114022.
[80] K. Liao, C. Hu, M. Sueyoshi, Free surface flow impacting on an elastic structure: Experiment versus numerical simulation, Appl. Ocean Res. 50 (2015) 192–208.
[81] A. Khayyer, Y. Shimizu, H. Gotoh, S. Hattori, Multi-resolution ISPH-SPH for accurate and efficient simulation of hydroelastic fluid-structure interactions in ocean engineering, Ocean Eng. 226 (2021) 108652.
[82] B. Xue, S.-P. Wang, Y.-X. Peng, A.-M. Zhang, A novel coupled Riemann SPH–RKPM model for the simulation of weakly compressible fluid–structure interaction problems, Ocean Eng. 266 (2022) 112447.
[83] B. Zhang, J. Zhu, X. Hu, Corrected Riemann smoothed particle hydrodynamics method for multi-resolution fluid–structure interaction, Phys. Fluids 37 (4) (2025) 042122.
[84] P. Sun, D. Le Touzé, A.-M. Zhang, Study of a complex fluid-structure dam-breaking benchmark problem using a multi-phase SPH method with APR, Eng. Anal. Bound. Elem. 104 (2019) 240–258.
[85] P.-N. Sun, D. Le Touze, G. Oger, A.-M. Zhang, An accurate FSI-SPH modeling of challenging fluid-structure interaction problems in two and three dimensions, Ocean Eng. 221 (2021) 108552.
[86] S. Zhang, S.D. Lourenço, D. Wu, C. Zhang, X. Hu, Essentially non-hourglass SPH elastic dynamics, J. Comput. Phys. 510 (2024) 113072.
[87] S. Zhang, D. Wu, S.D. Lourenço, X. Hu, A generalized non-hourglass updated Lagrangian formulation for SPH solid dynamics, Comput. Methods Appl. Mech. Engrg. 440 (2025) 117948.
[88] D.-M. Zhang, L. Han, Z.-K. Huang, A numerical approach for fluid-particle-structure interactions problem with CFD-DEM-CSD coupling method, Comput. Geotech. 152 (2022) 105007.
[89] J.D. Goddard, Nonlinear elasticity and pressure-dependent wave speeds in granular media, Proc. R. Soc. Lond. Ser. A 430 (1878) (1990) 105–131.
[90] J.C. Santamarina, K.A. Klein, M.A. Fam, Soils and Waves: Particulate Materials Behavior, Characterization and Process Monitoring, first ed., John Wiley & Sons, Chichester, UK, 2001.
[91] P.-E. Peyneau, J.-N. Roux, Frictionless bead packs have macroscopic friction, but no dilatancy, Phys. Rev. E 78 (1) (2008) 011307.
[92] A. Skinner, A note on the influence of interparticle friction on the shearing strength of a random assembly of spherical particles, Géotechnique 19 (1) (1969) 150–157.
[93] E. Grimaldi, E. Dressaire, Crater formation by sphere impact on a submerged granular bed, J. Vis. 19 (4) (2016) 577–579.
[94] A.M. Worthington, R.S. Cole, V. Impact with a liquid surface, studied by the aid of instantaneous photography, Philos. Trans. R. Soc. Lond. Ser. A (189) (1897) 137–148.
[95] A.M. Worthington, R.S. Cole, IV. Impact with a liquid surface studied by the aid of instantaneous photography. Paper II, Philos. Trans. R. Soc. Lond. Ser. A 194 (252–261) (1900) 175–199.
[96] J.M. Aristoff, J.W. Bush, Water entry of small hydrophobic spheres, J. Fluid Mech. 619 (2009) 45–78.

[97] T.T. Truscott, B.P. Epps, J. Belden, Water entry of projectiles, Annu. Rev. Fluid Mech. 46 (1) (2014) 355–378.
[98] S. Gekle, J.M. Gordillo, D. van der Meer, D. Lohse, High-speed jet formation after solid object impact, Phys. Rev. Lett. 102 (3) (2009) 034502.
[99] C. Ng, C. Choi, D. Song, J. Kwan, R. Koo, H. Shiu, K. Ho, Physical modeling of baffles influence on landslide debris mobility, Landslides 12 (1) (2015) 1–18.
[100] P. Lumb, The residual soils of Hong Kong, Géotechnique 15 (2) (1965) 180–194.
[101] C.W. Ng, Y. Pang, Influence of stress state on soil-water characteristics and slope stability, J. Geotech. Geoenvironmental Eng. 126 (2) (2000) 157–166.
[102] R.G. Dean, R.A. Dalrymple, Water Wave Mechanics for Engineers and Scientists, vol. 2, World Scientific Publishing Company, 1991.
[103] C. Zhang, Y. Wei, F. Dias, X. Hu, An efficient fully Lagrangian solver for modeling wave interaction with oscillating wave surge converter, Ocean Eng. 236 (2021) 109540.